

# Frequent but Predictable Droughts in East Africa Driven by A Walker Circulation Intensification

Chris Funk<sup>1</sup>, Andreas H. Fink<sup>2</sup>, Laura Harrison<sup>1</sup>, Zewdu Segele<sup>3</sup>, Hussen Seid Endris<sup>4</sup>, Gideon Galu<sup>5</sup>, Diriba Korecha<sup>6</sup>, and Sharon E. Nicholson<sup>7</sup>

<sup>1</sup>University of California, Santa Barbara

<sup>2</sup>Karlsruhe Institute of Technology

<sup>3</sup>IGAD Climate Prediction and Applications Centre [ICPAC]

<sup>4</sup>IGAD Climate Prediction and Applications Center

<sup>5</sup>United States Geological Survey

<sup>6</sup>Famine Early Warning Systems Network

<sup>7</sup>Florida State University

February 9, 2023

## Abstract

The decline of the eastern East African (EA) March-April-May (MAM) rains poses a life-threatening “enigma,” an enigma linked to sequential droughts in the most food-insecure region of the world. The MAM 2022 drought was the driest on record, preceded by three poor rainy seasons, and followed by widespread starvation. Connecting these droughts is an interaction between La Niña and climate change, an interaction that provides exciting opportunities for long-lead prediction and proactive disaster risk management. Using observations, reanalyses, and climate change simulations, we show here, for the first time, that post-1997 OND La Niña events are robust precursors of: (1) strong MAM “Western V Gradients” in the Pacific, which help produce (2) large increases in moisture convergence and atmospheric heating near Indonesia, which appear associated with (3) regional shifts in moisture transports and vertical velocities, which (4) help explain more frequent dry EA rainy seasons. Understanding this causal chain will help make long-lead forecasts more actionable. Increased Warm Pool atmospheric heating and moisture convergence sets the stage for dangerous sequential droughts in EA. At 20-year time scales, we show that these Warm Pool heating increases are attributable to observed Western V warming, which is, in turn, largely attributable to climate change. As energy builds up in the oceans and atmosphere, we see stronger convergence patterns, which offer opportunities for prediction. Hence, linking EA drying to a stronger Walker Circulation can help explain the “enigma” while underscoring the predictable risks associated with recent La Niña events.

1 **Frequent but Predictable Droughts in East Africa Driven By A Walker Circulation**  
2 **Intensification**

3  
4 **Chris Funk<sup>1</sup>, Andreas H. Fink<sup>2</sup>, Laura Harrison<sup>1</sup>, Zewdu Segele<sup>3</sup>, Hussen S. Endris<sup>3</sup>,**  
5 **Gideon Galu<sup>1</sup>, Sharon Nicholson<sup>4</sup>, Diriba Korecha<sup>1</sup>**

6  
7 <sup>1</sup>Climate Hazards Center, University of California, Santa Barbara

8  
9 <sup>2</sup> Institute of Meteorology and Climate Research, Karlsruhe Institute of Technology, Karlsruhe,  
10 Germany

11  
12 <sup>3</sup>IGAD Climate Prediction and Applications Center, Kenya

13  
14 <sup>4</sup>Meteorology and Environmental Science, Florida State University

15  
16 Corresponding Author: Chris Funk

17 **Email:** [chrisfunk@ucsb.edu](mailto:chrisfunk@ucsb.edu)

18 **Key Points:**

- 19
- 20 • Human-induced warming in the western V area of the Pacific combined with La Niña, has produced frequent, predictable March-April-May droughts.
  - 21 • Thermodynamic analyses link these droughts to a stronger Walker Ciruclation, driven by  
22 predictable warming in the Western V region.
  - 23 • CMIP6 simulations indicate that western V warming is largely human-induced, this  
24 warming has enhanced and will enhance the Walker Circulation.
- 25  
26

## 27 **Abstract**

28 The decline of the eastern East African (EA) March-April-May (MAM) rains poses a life-  
29 threatening ‘enigma’, an enigma linked to sequential droughts in the most food insecure region  
30 in the world. The MAM 2022 drought was the driest on record, preceded by three poor rainy  
31 seasons, and followed by widespread starvation. Connecting these droughts is an interaction  
32 between La Niña and climate change, an interaction that provides exciting opportunities for long  
33 lead prediction and proactive disaster risk management. Using observations, reanalyses, and  
34 climate change simulations, we show here, for the first time, that post-1997 OND La Niña events  
35 are robust precursors of: (1) strong MAM ‘Western V Gradients’ in the Pacific, which help  
36 produce (2) large increases in moisture convergence and atmospheric heating near Indonesia,  
37 which appear associated with (3) regional shifts in moisture transports and vertical velocities,  
38 which (4) help explain more frequent dry EA rainy seasons. Understanding this causal chain will  
39 help make long-lead forecasts more actionable. Increased Warm Pool atmospheric heating and  
40 moisture convergence sets the stage for dangerous sequential droughts in EA. At 20-yr time  
41 scales, we show that these Warm Pool heating increases are attributable to observed Western V  
42 warming, which is in turn largely attributable to climate change. As energy builds up in the  
43 oceans and atmosphere, we see stronger convergence patterns, which offer opportunities for  
44 prediction. Hence, linking EA drying to a stronger Walker Circulation can help explain the  
45 ‘enigma’ while underscoring the predictable risks associated with recent La Niña events.

46

## 47 **Plain Language Summary**

48 In 2022, an unprecedented sequence of five sequential droughts, exacerbated by high global  
49 food and fuel prices, drove an exceptional food security crisis in Ethiopia, Somalia and Kenya,  
50 pushing more than 20 million people into a food security crisis. Potential famine loomed in some  
51 areas. Beginning in late 2020, this was the longest and most severe drought recorded in the Horn  
52 in at least 70 years, resulting in multiple failed harvests and large-scale livestock deaths that  
53 decimated food and income sources for rural communities, placed increasing pressure on the cost  
54 of food among urban communities, and led to rising levels of destitution and displacement.  
55 These droughts occur against the backdrop of the ‘East Africa Climate Paradox’, which centers  
56 on the discrepancy between climate change model projections of increased East African March-  
57 April-May rains, and many observational studies pointing towards declines. Here, we show how  
58 framing this dilemma as an ‘enigma’ opens the door to explaining and predicting sequential East  
59 African droughts. The enigma we explore is ‘why are so many recent La Niña events associated  
60 with dry March-April-May rains?’ La Niña events tend to reach their maximum intensity in the  
61 boreal fall, often producing East African droughts. Before the western Pacific ocean warmed  
62 dramatically in 1998, the link between La Niña events and dry March-April-May rains was  
63 weak. Since 1998, the link is very strong. This sets the stage for dangerous sequential droughts,  
64 such as in 2010/11, 2016/17, 2020/21, 2021/2022, and perhaps 2022/23. We explain this enigma  
65 using observations, reanalyses, and the latest (Phase 6) climate change simulations.

66 While climate change models do recreate the observed East African drying, they do recreate  
67 very well the observed west Pacific warming. Climate change, not natural decadal variability  
68 associated with the Pacific Decadal Oscillation, has increased west Pacific sea surface  
69 temperatures. This, in turn, is increasing the ‘Western V Gradient’, a measure of the east-west  
70 differences in Pacific ocean temperatures. When this gradient is negative, there are frequent East

71 African droughts, and this happens in a very predictable way during or after recent La Niña  
72 events. This allows us to predict many dry rainy seasons ~eight months in advance. Such  
73 predictive capacity is important, because the frequency of strong Pacific temperature gradients is  
74 increasing, and we shown that climate change simulations recreate this tendency, and expect it to  
75 increase over the coming decades.

76 What connects East African droughts to Pacific temperature gradients? We answer this  
77 question by examining observed atmospheric heating, moisture transports, and moisture  
78 convergence patterns. In general, eastern East Africa is dry because it resides along the western  
79 edge of the Indian Ocean branch of the Indo-Pacific 'Walker Circulation'. Across East Africa  
80 and the western Indian Ocean, and over the central and eastern Pacific, rainfall and moisture  
81 levels are low. In the area around Indonesia (the eastern Indian and western Pacific Oceans),  
82 winds drive moisture convergence and heavy rains. Here, building on many years of research by  
83 scientists working for the Famine Early Warning Systems Network, we show for the first time  
84 that the strength of the Walker Circulation can be quantified using atmospheric heating and  
85 moisture convergence. When heating and moisture convergence is high in the area around  
86 Indonesia, East African rains are almost always dry. Since 1998, when there has been a La Niña  
87 in October-November-December, there has almost always been strong March-April-May heating  
88 and moisture convergence around Indonesia. This resolves the enigma. Climate change-enhanced  
89 La Niñas amplify the Pacific trade winds, producing strong March-April-May sea surface  
90 temperature gradients, which amplify the Walker Circulation, which reduce moisture  
91 convergence and ascending atmospheric motions over the eastern Horn of Africa.

92 We conclude with a look toward the future evolution of the Walker Circulation, by relating  
93 the observed strength of the Walker Circulation to 20-yr averages of western and eastern Pacific  
94 sea surface temperatures. Both play a significant role, and together explain 96% of the observed  
95 variability. The observed Walker Circulation intensification is primarily driven by the west  
96 Pacific, which in turn is strongly related to climate change. CMIP6 projections of Pacific sea  
97 surface temperatures, combined with the observed empirical relationships, imply further strong  
98 increases in Walker Circulation intensities. Hence, further rainfall declines appear likely,  
99 especially before or after La Niña events. But the process-based analyses presented here suggests  
100 that many of the dry seasons may be predictable, based on Pacific sea surface temperature  
101 gradients.

102

103

104

## 105 **1 Introduction – CMIP6 simulations can enhance drought early warning to support food** 106 **security**

107 This study examines the drivers of March-April-May rains in eastern East Africa (EA), a region  
108 of extreme food insecurity and frequent droughts [Shukla *et al.*, 2021]. Located near the equator  
109 and the descending branch of the Indian Ocean branch of east-west Walker Circulation, this  
110 region receives rains in OND and MAM [Brant Liebmann *et al.*, 2012; Nicholson, 2017].  
111 Sequential OND/MAM droughts can have profound food security impacts, as in 2010/2011,  
112 when more 250,000 Somalis perished due to famine [Checchi and Robinson, 2013]. In 2020-2022  
113 an unprecedented sequence of five dry seasons, associated with a three-year La Niña event, led  
114 to a massive humanitarian crisis, potential famine, and widespread loss of livestock and  
115 livelihoods [ICPAC *et al.*, 2022a; ICPAC *et al.*, 2022b]. These crises occur amidst a continuing  
116 and well-documented decline in MAM ‘long’ rains, as first identified by the Famine Early  
117 Warning Systems Network (FEWS NET) [Funk *et al.*, 2005; Verdin *et al.*, 2005], and later  
118 studies [Lyon, 2014; Lyon and DeWitt, 2012; Yang *et al.*, 2014]. Following the 1997/98 El Niño,  
119 dry MAM seasons became more frequent [Lyon, 2014], while the variability of OND rains  
120 increased [Nicholson, 2015]. The MAM season is also becoming ‘shorter not less intense’ due to  
121 regional circulation changes [Wainwright *et al.*, 2019].

122  
123 Our focus here is the potential link between climate change and the dramatic post-1998 increase  
124 in the frequency of dry MAM seasons, following OND La Niñas. This increase sets the stage for  
125 dangerous OND/MAM multi-season droughts [Funk *et al.*, 2018], but also opens opportunities  
126 for predicting the MAM rains, as in 2017 [Voosen, 2020] and 2021 and 2022 [Rubiano, 2022].  
127 As noted in a 2022 multi-agency alert [ICPAC *et al.*, 2022a], between 1950 and 1997, OND La  
128 Niña conditions, as defined by the Climate Prediction Center [NOAA, 2022], did not alter the  
129 odds of a below-normal (bottom tercile) EA MAM rainy season. Following the twelve La Niñas  
130 since OND 1998, nine rainy seasons have been poor. This shift, and OND La Niña conditions in  
131 2020, 2021, and 2022 has contributed to repetitive droughts and potential famine conditions in  
132 2023 [ICPAC *et al.*, 2022b]. Here, in contrast with other valuable studies that focused on larger  
133 domains, regional climate processes, or sub-seasonal drivers [Finney *et al.*, 2020; Nicholson,  
134 2017; Wainwright *et al.*, 2019], we focus here on large-scale teleconnections that may help  
135 identify, explain and predict recent below-normal EA MAM rainy seasons. These results help  
136 explain regional circulation changes consistent with a ‘shorter not less intense’ rainy season  
137 [Wainwright *et al.*, 2019] and the increasing links to the El Niño Southern Oscillation (ENSO)  
138 [Park *et al.*, 2020]. Our goal in this paper is to support early warning and forecasting efforts by  
139 explaining the links between La Niña, predictable Pacific SST gradients and EA dry seasons, on  
140 both interannual and decadal time-scales.

141  
142 Our study proceeds in three stages. We first examine CMIP6 and observed EA MAM  
143 precipitation and Pacific sea surface temperatures (SST). This links EA drying to human-induced  
144 warming in the west Pacific. Then, using reanalyses, we show that strong Pacific SST gradients  
145 and Walker Circulation disruptions follow post-1997 La Niñas. Seasons with more intense with  
146 Walker Circulations are clearly linked to a preponderance of dry EA MAM seasons. We then use  
147 observed Pacific SST gradients and CMIP6 SST projections to suggest that human-induced west

148 Pacific warming has, and will, enhance the Walker Circulation in ways associated with drying  
149 over EA.

150

151

## 152 **1.1 Background – Describing the ‘East Africa Enigma’**

153

154 Following its introduction in 2015 [Rowell *et al.*, 2015], several papers have discussed the ‘East  
155 African Climate Paradox’ [Lyon and Vigaud, 2017; Wainwright *et al.*, 2019] – while  
156 observations clearly indicate more frequent dry seasons along with later starts and early cessation  
157 [Wainwright *et al.*, 2019], climate change simulations have indicated rainfall increases. While  
158 natural Pacific Decadal Variability (PDV) [Lyon, 2014; Lyon and Vigaud, 2017; Yang *et al.*,  
159 2014] might explain this change, it is becoming more and more likely that the ‘paradox’ arises  
160 due to the models’ systematic biases in SSTs and African circulation features [Lyon, 2020; 2021;  
161 Schwarzwald *et al.*, 2022; Shukla *et al.*, 2016; J E Tierney *et al.*, 2015]. The terrain and  
162 teleconnections controlling precipitation in EA are complex and poorly resolved by global  
163 climate models [Endris *et al.*, 2016]. The models tend to misrepresent the mean zonal SST  
164 gradients in the Indian Ocean [Lyon, 2021; Lyon and Vigaud, 2017; Schwarzwald *et al.*, 2022]  
165 and Pacific Ocean [Seager *et al.*, 2022; Seager *et al.*, 2019]. Over EA they tend to have a  
166 seasonal cycle that is far too wet in OND and dry in MAM [J Tierney *et al.*, 2013]. Multi-model  
167 ensembles of regional climate model simulations perform much better [Endris *et al.*, 2013], and  
168 indicate decreased rainfall in MAM [Ogega *et al.*, 2020]. Recent evaluations of regional and  
169 global climate change models [Endris *et al.*, 2019] indicate stronger future ENSO  
170 teleconnections during MAM, consistent with several climate change studies indicating an  
171 increased frequency of strong-gradient La Niñas [Cai *et al.*, 2022; Cai *et al.*, 2015b].

172 In place of the ‘paradox’, we focus here on the ‘East African Climate Enigma’. The ‘enigma’  
173 relates the increased frequency of dry MAM seasons, following OND La Niñas, to predictable  
174 ‘Western V’ SST gradients (described below) in MAM. The Western V region begins in  
175 equatorial West Pacific (near Indonesia), and extends poleward into the extra-tropical northern  
176 and southern Pacific. Warm SSTs in this region have been linked to dry EEA MAM rainy  
177 seasons [Funk *et al.*, 2018; Funk *et al.*, 2019] and the West Pacific Warming Mode [Funk and  
178 Hoell, 2015]. From a food security perspective, the link between OND La Niñas and MAM  
179 rainfall deficits is important, because it sets the stage for dangerous sequential droughts. Long  
180 lead MAM rainfall forecasts have helped guide humanitarian responses in 2017 [Voosen, 2020],  
181 and 2021/2022 [Button, 2022]. But while they are effective, there has not been relatively little  
182 research focused on how strong Pacific SST gradients induce dry EA rainy seasons, why such  
183 conditions tend to be associated with La Niña events, and how human-induced warming might  
184 be influencing outcomes.

## 185 **2 Methods**

186 The focus here will be on explaining the link between recent (post-1997) OND La Niñas,  
187 as defined by OND [Funk *et al.*, 2018; Funk *et al.*, 2019] NOAA Oceanic Niño Index, ONI  
188 values [NOAA, 2022] and frequent MAM dry seasons in the following year. This also relates to  
189 recent work documenting increasing ENSO-East Africa teleconnections [Park *et al.*, 2020].  
190 While forecasting is not the focus here, these explorations provide process-based insights that  
191 can inform operational forecasts, such as those provided by the IGAD Climate Prediction and

192 Applications Center (ICPAC, [www.icpac.net](http://www.icpac.net)) or the Climate Hazards Center (CHC,  
 193 [blog.chc.ucsb.edu](http://blog.chc.ucsb.edu)). Our goals are to better understand links between the WVG and La Niñas, the  
 194 WVG and the Walker Circulation, and the WVG and climate change. This work has implications  
 195 for seasonal climate prediction, humanitarian assistance programming, and climate change  
 196 adaptation. Our study progresses in three stages.

## 197 **2.1 Linking droughts to predictable Pacific SST gradients and human-induced warming in** 198 **the west Pacific**

199 We begin by describing the ‘East African Climate Paradox’ [Rowell *et al.*, 2015] using updated  
 200 (through 2022) rainfall and SST observations and CMIP6 precipitation simulations. Composites  
 201 of SSTs for dry and wet seasons are evaluated. Dry events, but not wet events, are associated  
 202 with coherent SST teleconnections. Dry MAM seasons are characterized by very warm west  
 203 Pacific ‘Western V’ SSTs. The western V originates in the Warm Pool area around Indonesia  
 204 and extends northeast and southeast into the extra-tropics. Warm Western V conditions have  
 205 been linked to recent MAM droughts [Funk *et al.*, 2018; Funk *et al.*, 2019]. Warming in this  
 206 region also loads heavily on the ‘West Pacific Warming Mode’, the first empirical orthogonal  
 207 function of global ENSO-residual SST [Funk and Hoell, 2015]. We define the ‘Western V  
 208 Gradient’ (WVG) as the difference between standardized NINO3.4 and Western V SSTs. Since  
 209 the west Pacific warmed following the 1997/1998 El Niño [Lyon *et al.*, 2013] and the Walker  
 210 Circulation intensified [L’Heureux *et al.*, 2013], OND La Niña events [NOAA, 2022] are always  
 211 followed by strong negative WVG values in MAM. We show that these WVG values are very  
 212 predictable. We also show that these predictions do a good job of identifying many dry MAM  
 213 seasons at long leads. Using observations, we show that since 1999, strong negative MAM WVG  
 214 events always follow La Niña events in the previous OND, when the La Niña signal tends to be  
 215 at its peak. Then, using CMIP6 simulations, we examine the level of correspondence between the  
 216 simulated SST warming trends, and observed outcomes in the NINO3.4 and Western V regions,  
 217 as well as the WVG.

## 218 **2.2 Linking La Niña/WVG events to Walker Circulation Intensification**

219 This section examines interannual WVG influences on MAM Indo-Pacific atmospheric heating,  
 220 moisture transports, and moisture convergence fields. Long term means and WVG anomalies in  
 221 atmospheric heating and moisture transports can be used to explore the Indian and Pacific  
 222 branches of the Walker Circulation [Bjerknes, 1969]. Note that we use the term ‘Walker  
 223 Circulation’ to broadly refer to the complex Indo-Pacific circulation patterns linking the Pacific  
 224 to the Warm Pool region near Indonesia, and the Warm Pool region to MAM EA rains. While we  
 225 present equatorial longitude-by-height results, we also examine spatial maps which emphasize  
 226 that emphasize how extra-tropical SST and atmospheric heating gradients act to modulate  
 227 moisture transports.

228  
 229 Our thermodynamic approach was inspired by studies using vertically integrated transports of  
 230 heat energy (internal energy,  $T$ ) and geopotential height energy (potential energy,  $Z$ ) [Peixoto  
 231 and Oort, 1992; Trenberth and Stepaniak, 2003a; b].  $T$  is a function of the vertical temperature  
 232 distribution and specific heat capacity of air,  $Z$  is a function of geopotential height and  $g$ , the  
 233 acceleration due to gravity. These are the two largest atmospheric energy terms. In atmospheric

234 thermodynamics, it is common to combine these two terms to describe changes in Dry Static  
235 Energy (DSE):

$$236 \quad \quad \quad \text{DSE} = T + Z \quad \quad \quad \text{eq. 1}$$

238  
239 DSE is a conserved quantity. Changes in DSE, however, arise from the introduction of external  
240 heating, commonly referred to as diabatic heating. Latent heating (LH) due to precipitation,  
241 radiation (R), and sensible heating (SH) in the planetary boundary layer are the largest sources of  
242 diabatic heating. The R term here is a measure of the net radiation into a column of air, i.e. a  
243 combination of the downward and upward shortwave radiation from the top of the atmosphere  
244 and surface of the Earth. Increased atmospheric water vapor contributes to increased trapped  
245 longwave radiation and increased precipitation. As the atmosphere warms and saturation vapor  
246 pressures increase, these heating terms are likely to increase as well. DSE is a conserved  
247 quantity, modulated by external (diabatic) heating, which leads to:

$$248 \quad \quad \quad \text{diabatic heating} = \text{Div}(T) + \text{Div}(Z) \quad \quad \quad \text{eq. 2}$$

249  
250 Where  $\text{Div}(T)$  and  $\text{Div}(Z)$  are vertically-integrated divergence terms, based on vertically  
251 integrated temperature and geopotential height fluxes. While accurate, the standard DSE  
252 formulation of these terms obscures the fact that  $\text{Div}(T)$  and  $\text{Div}(Z)$  are strongly anti-correlated,  
253 due to hydrostatic relationships [*Peixoto and Oort, 1992*]. Converging heat in the lower and  
254 middle troposphere causes a column of air to stretch, raising upper-level heights, and increasing  
255  $\text{Div}(Z)$ . In rainy areas of the Walker Circulation, heat converges in the lower troposphere, and  
256 geopotential height energy diverges aloft. Persistent heating in the Indo-Pacific Warm Pool area  
257 produces equatorially-trapped Rossby and Kelvin waves, which (respectively) help establish the  
258 Indian and Pacific branches of the Walker Circulation [*Gill, 1980; 1982*]. To measure the  
259 strength of this forcing, we combine diabatic heating and heat convergence into a single  
260 ‘atmospheric heating’ term, measured in  $\text{Wm}^{-2}$ .

$$261 \quad \quad \quad \text{atmospheric heating} = \text{Con}(T) + \text{diabatic forcing} \quad \quad \quad \text{eq. 3}$$

262  
263 As we will show, this framework provides a useful description of the humid and dry regions of  
264 the Walker Circulation. Areas with low level convergent winds will have both heat convergence  
265  $\text{Con}(T)$  and moisture convergence  $\text{Con}(Q)$ . Direct heating by heat convergence will be  
266 augmented by latent heat released via precipitation, since moisture is also conserved:

$$267 \quad \quad \quad \text{precipitation} = \text{Con}(Q) - \text{evaporation} \quad \quad \quad \text{eq. 4}$$

270  
271 Since evaporation in Warm Pool areas tends to be low,  $\text{precipitation} \approx \text{Con}(Q)$ . More moisture  
272 will also increase the trapping of longwave radiation. Eq. 3, therefore, stacks covarying heating  
273 terms. From first principles, a warming atmosphere might experience increased heat  
274 convergence, simply due to increases in air temperatures, as well as increases in precipitation and  
275 decreases in outgoing longwave radiation, due to increased atmospheric water vapor. This logic  
276 also supports combining these heating terms. We examine these variables to formally evaluate  
277 whether a Walker Circulation enhancement is linked to dry EA rainy seasons. Contrasting these  
278 fields, in MAM seasons following 1998-2021 OND La Niñas and 1950-1997 La Niñas helps  
279

280 explain links between distant WVG SST patterns and local reductions in EA MAM total  
281 precipitable water, vertical ascent, and precipitation. Changes in the Indian Ocean branch of the  
282 Walker Circulation alter moisture transports and intensify subsidence over the eastern Horn of  
283 Africa.

### 284 **2.3 Linking Western V warming to Walker Circulation intensification and more frequent** 285 **dry EA rainy seasons**

286  
287 Our final analysis focuses on decadal changes in the strength of the Walker Circulation and the  
288 frequency of below-normal MAM rainy seasons. We begin by updating the observational West  
289 Pacific Warming Mode (WPWM) analysis from Funk and Hoell (2015). This Empirical  
290 Orthogonal Function analysis underscores the points that 1) NINO3.4 and Western V and  
291 NINO3.4 SSTs closely track the first two modes of global SST, and 2) the climate-change-  
292 related WPWM, along with Western V SSTs, continues to increase rapidly. We then use  
293 regression to link 20-yr average Western V and NINO3.4 SST to 20-yr averages of Warm Pool  
294 atmospheric heating. We show that these SST values explain very well 20-yr changes in Warm  
295 Pool atmospheric heating and that the Western V warming has played an important role in the  
296 recent Walker Circulation intensification and the increased frequency of dry East African rainy  
297 seasons. CMIP6 SST ensembles are used to estimate increases in Warm Pool heating through  
298 2050.

## 299 **3 Data**

300 Dry and wet seasons are defined using satellite-gauge [Funk *et al.*, 2015b] and interpolated  
301 gauge [Funk *et al.*, 2015a] datasets. These widely used data sets were specifically developed to  
302 work well in East Africa, work well [Dinku *et al.*, 2018], and incorporate many additional  
303 raingauge observations provided by collaborators at Florida State University [Nicholson, 2017],  
304 the Ethiopian Meteorological Agency (~120 stations), and the Somali Food Security and  
305 Nutrition Analysis Unit (~90 stations). The EA area of focus is based on the region used in a  
306 mid-2022 multi-agency alert focused on the failure of the MAM 2022 rains [ICPAC *et al.*,  
307 2022a]. Areal averages of the 1981-2022 Climate Hazards InfraRed Precipitation with Stations  
308 (CHIRPS) [Funk *et al.*, 2015a] and the 1900-2014 Centennial Trends [Funk *et al.*, 2015b]  
309 correlate very well over their period of overlap (1981-2014). A bivariate regression is used to  
310 transform Centennial Trends values into CHIRPS-compatible regional averages over the 1950-  
311 1980 period. A Gamma distribution fit is then used to develop a Standardized Precipitation Index  
312 (SPI) times-series [Husak *et al.*, 2007]. This time series, and all other analyses in this study, are  
313 centered on a 1981-2021 baseline. Dry and wet seasons will be based on the EA SPI values  
314 below and above -0.44Z and +0.44Z, which corresponds with a 1-in-3 year low or high value.  
315 Dry seasons may occasionally be described as droughts, to avoid repetition. Version 5 of the  
316 NOAA Extended SST [Huang *et al.*, 2017] is used to represent ocean temperatures. To explore  
317 circulation changes we use ERA5 [Hersbach *et al.*, 2020] and MERRA2 [Gelaro *et al.*, 2017]  
318 reanalyses. Our analysis looks at moisture transports and the combined influence of local  
319 diabatic heating and atmospheric heat convergence. We also include in our study August

320 forecasts of MAM SSTs from the North American Multi-Model Ensemble (NMME)[*Kirtman et*  
321 *al.*, 2014].

322

323 Our study also uses a multi-model ensemble of 152 Shared Socio-Economic Pathway 245 SST  
324 simulations from the latest CMIP version 6 (CMIP6) archive [*Eyring et al.*, 2016] (Table 1). The  
325 moderate SSP245 scenario is based on projections of large increases in sustainable development  
326 and  $4.5 \text{ Wm}^{-2}$  of radiative forcing [*Meinshausen et al.*, 2020]. CMIP6 data were accessed from  
327 Lawrence Livermore National Laboratory (LLNL) node of the Earth System Grid Federation  
328 (ESGF) platform (<https://esgf-node.llnl.gov/search/cmip6/>).

329

330 Finally, it should be noted that most of our observational results focus on the 1981-2022 time  
331 period, during which satellite data informs our precipitation estimates and reanalyses. While we  
332 do present longer time-series of EA rainfall, and changes in 1950-2022 ERA5 WVG events, the  
333 bulk of our analysis focuses on the past 42 years. This allows for cross-checks between the  
334 ERA5 and MERRA2 reanalyses.

## 335 4 Results

### 336 4.1 Links between OND La Niña, predictable strong Western V Gradients and EA 337 Droughts

338

339 In MAM 2022, rains in Ethiopia, Kenya and Somalia were exceptionally poor (Fig. 1A,B). Here,  
340 as in several previous FEWS NET [*Funk and al.*, 2019] studies [*Funk et al.*, 2014; *Funk et al.*,  
341 2018; *Funk et al.*, 2019; *B. Liebmann et al.*, 2014], we focus on a specific spatial subset of the  
342 Greater Horn of Africa, eastern East Africa (purple polygon shown in Fig. 1A), not a broader  
343 region as in [*Finney et al.*, 2020; *Walker et al.*, 2020], because this extremely food insecure  
344 region [*Shukla et al.*, 2021] experiences frequent sequential droughts, especially during or  
345 following recent La Niña events [*Funk et al.*, 2014; *Funk et al.*, 2018; *Funk et al.*, 2019; *Hoell*  
346 *and Funk*, 2013a; b; *B. Liebmann et al.*, 2014; *Williams and Funk*, 2011]. Since 1999, 11 seasons  
347 have been dry. Many of these dry seasons have also followed 12 post-1997 OND La Niñas  
348 (yellow circles, Fig. 1B). We refer to these events as ‘Western V Gradient’ events (described  
349 further below), because even if La Niña conditions fade, strong Pacific gradients, augmented by  
350 west Pacific warming, may be conducive to dry EA MAM outcomes [*Funk et al.*, 2018; *Funk et*  
351 *al.*, 2019].

352

353 The observed drying contrasts with results (Fig. 1C,D) from 152 CMIP6 SSP245 simulations  
354 (Table 1). Time-series of 30-yr average SPI indicate little change. The last observed and  
355 simulated values from this time-series (1993-2022 average SPI) are expanded in Fig. 1D, which  
356 breaks the results out by model. The observed 30-yr SPI value is very unlikely given the  
357 observed range of CMIP6 averages. This could be explained by a large natural internal decadal  
358 variation, potentially related to the Pacific (further discussed below), or it might relate to issues  
359 associated with poor representations of mean Indo-Pacific SSTs and EA seasonality and  
360 teleconnections (discussed above in section 1.1).

361

362 Composites of standardized MAM SSTs during 1981-2022 dry seasons (Fig. 2A) exhibit a  
363 contrast between a warm ‘Western V’ region in the west Pacific and cool central-east Pacific  
364 SSTs. Western V SST are averaged over the equatorial west Pacific ( $120\text{-}160^{\circ}\text{E}$ ,  $15^{\circ}\text{S}\text{-}20^{\circ}\text{N}$ ),

365 Western North Pacific (160°E-150°W, 20°N-35°N) and Western South Pacific (155°E-150°W,  
366 15°S-30°S). Western V [Funk et al., 2019] and Western North Pacific SST [Funk et al., 2018]  
367 have been linked to dry EA rains, and FEWS NET uses a standardized gradient between  
368 NINO3.4 and Western V SSTs (the Western V Gradient, WVG) to inform operational long-lead  
369 predictions. Interestingly, while dry MAM season composites exhibit significant links to the  
370 Pacific (Fig. 2A), and some relation to Indian Ocean SSTs, wet season composites indicate less  
371 strong links (Fig. 2B). Non-linearities have been previously identified for the OND season  
372 [Nicholson, 2015], but have received little attention in MAM. Dry events may be more  
373 predictable than wet events.

374  
375 Enigmatically, strong negative MAM WVG conditions are very common following recent OND  
376 La Niñas, and are also associated with many of the recent dry EA MAM seasons (Fig. 2C). There  
377 have been 12 OND La Niñas since 1998, and the MAM WVG values the following year ranged  
378 from -0.8Z to -2.2Z. Nine of these MAM seasons were dry EA years. Here, we will describe the  
379 12 post-1997 MAM seasons that follow the last 12 La Niñas as ‘WVG events’. It is important to  
380 differentiate these from La Niñas, because warm Western V SSTs can linger after a La Niña  
381 fades (as in 2016/17) producing La Niña-like impacts in MAM, consistent with stronger ENSO  
382 teleconnections [Park et al., 2020]. Strong warming trends in the western Pacific [Funk et al.,  
383 2018; Funk et al., 2019] and frequent La Niñas since the late 1990s have led to a marked  
384 increase in the frequency of strong negative WVG conditions during MAM (Fig. 2C).

385  
386 We can predict WVG conditions at long leads, allowing us to predict many of the events that  
387 produce the decline in EA rains. As an example, Fig. 2D shows forecasts of MAM WVG values,  
388 based on September North American Multi-Model Ensemble climate forecasts<sup>1</sup> [Kirtman et al.,  
389 2014]. Western V, WVG and NINO3.4 SSTs are all predicted very well by the NMME (1982-  
390 2022  $R^2$  0.77, 0.77, 0.67). When WVG values are predicted to be negative ( $< -0.5Z$ ) we see a  
391 preponderance of dry EA MAM rainy seasons, and many of the seasons with low WVG values  
392 follow OND La Niñas. The societal import of Fig. 2D is very important, because this approach  
393 can help anticipate dangerous OND/MAM sequential droughts, which in 2020-2022 brought four  
394 sequential dry seasons and the threat of starvation to millions in Ethiopia, Kenya, and Somalia  
395 [ICPAC et al., 2022a].

396  
397 Figure 3 presents observed and simulated changes in 20-yr MAM Western V, NINO3.4 and  
398 WVG time-series. For the Western V, the observations track very closely with the CMIP6  
399 simulations (Fig. 3A). The correlation between the CMIP6 median Western V values and the  
400 observed Western V time-series is 0.96. The CMIP6 simulations suggest that climate change, not  
401 natural Pacific Decadal variability, has resulted in large SST increases in the western V region.  
402 The pace of observed warming has increased dramatically over the past 20 years. The observed  
403 2003-2022 Western V average falls comfortably within the CMIP6 distribution (Fig. 3B). This  
404 contrasts with NINO3.4 outcomes (Fig. 3C-D). As noted by other studies, in observations, there  
405 is marked lack of warming in the eastern Pacific [Seager et al., 2022; Seager et al., 2019]. The  
406 CMIP6 ensemble, on the other hand, predicts substantial warming. The distribution of  
407 standardized 2003-2022 CMIP6 NINO3.4 values (Fig. 3D) suggests that the observed lack of  
408 cooling is very unlikely, given the simulations. This might arise due to an extreme expression of

---

<sup>1</sup> <https://www.agrilinks.org/post/forecast-update-east-africa-likely-experience-six-droughts-row>

409 natural decadal variability. However, it seems increasingly likely that systematic biases in Pacific  
410 SST may also contribute to this discrepancy [Seager *et al.*, 2022; Seager *et al.*, 2019].

411  
412 As one would expect, WVG observations and CMIP6 simulations (Fig. 3E-F), fall between  
413 panels 3A-B and 3C-D. While the observed 2002-2023 WVG value (-0.5Z) falls at the edge of  
414 the CMIP6 distribution (Fig. 3F), the CMIP6 ensemble does predict reductions in the WVG  
415 (Fig. 3E), due to the influence of human-induced warming in the Western V. Assuming that the  
416 CMIP6 WVG simulations are 'true', and that the lack of warming in the NINO3.4 region is  
417 natural, these results still indicate that about half of the observed increase in the WVG has been  
418 caused by climate change. If the CMIP6 models are over-estimating warming the NINO3.4  
419 region, then climate change would account for a greater portion of the observed decrease in  
420 WVG values.

#### 421 422 **4.2 Linking WVG events to large and energetic changes in the Walker Circulation**

423  
424 A better understanding of the processes that link Pacific SSTs and dry EA outcomes will help  
425 build confidence in dry season outlooks, which will make them more actionable. To that end we  
426 examine MAM WVG circulation anomalies using ERA5 and MERRA2 reanalyses. As discussed  
427 in the methods section, atmospheric heating is inversely correlated with the divergence of  
428 geopotential height energy (Fig. 4A-B), and the long term mean atmospheric heating (Fig. 4C)  
429 and geopotential divergence fields (Fig. 4D) help delineate the low and high pressure cells that  
430 comprise the global Walker Circulation.

431  
432 Climatologically, the atmospheric heating that drives the Walker Circulation can be visualized  
433 by examining maps of vertically integrated diabatic heating (Fig. 5A) and atmospheric heat  
434 convergence (Fig. 5B). These are the two terms on the right hand side of eq. 3. In the tropics,  
435 diabatic heating in the lower and middle troposphere destabilizes the atmosphere and produces  
436 lower surface pressures, which drives atmospheric heat convergence (Fig. 5B). We refer to the  
437 combination of diabatic heating and heat convergence as atmospheric heating. Because  
438 temperatures and water vapor are both larger in the lower troposphere, vertically integrated heat  
439 and moisture transports are very similar. Areas with strong moisture convergence will have  
440 heavy precipitation, and strong heat convergence, and large amounts of water vapor will trap  
441 longwave radiation. In the Indo-Pacific, this region is often referred to as the 'Warm Pool'. Fig.  
442 5A,B also show long term average moisture transports. The Pacific Trade winds feed very large  
443 transports of heat and moisture into the Warm Pool, linking the Walker Circulation to Pacific  
444 SSTs.

445  
446 In MAM, the Indian Ocean branch of the Walker Circulation can be characterized by strong  
447 atmospheric heating ( $>450\text{Wm}^{-2}$ ) in the eastern equatorial Indian Ocean, and heat divergence ( $<-$   
448  $270\text{Wm}^{-2}$ ) over the southern and equatorial western Indian Ocean (Fig. 5AB). This strong  
449 heating gradient produces a strong low-level pressure gradient associated winds that transport  
450 moisture across the southern Indian Ocean and into East Africa (arrows in yellow boxes Fig.  
451 5AB). Over the southern Indian Ocean ( $\sim 60\text{-}110^\circ\text{E}$ , between  $\sim 30^\circ\text{S}$  and  $5^\circ\text{S}$ ), we see mean  
452 atmospheric heating values change from strong cooling to strong heating. This atmospheric  
453 heating gradient is also associated with a strong meridional sea level pressure gradient that drives  
454 easterly moisture transports that drives easterly moisture transports that cross the equator and

455 feed moisture into EA. Longitude-by-height transects of climatological equatorial (5°S-5°N)  
456 ERA5 vertical velocities and zonal velocities reveal, on average, descending air tendencies  
457 between 40 and 55°E that heat and stabilize the atmosphere over the eastern Horn of Africa (Fig.  
458 5C). Thus, we see in terms of the long-term mean climate over the Indian Ocean offsetting  
459 contributions from atmospheric heating over the Indian Ocean Warm Pool. Over the southeastern  
460 Indian Ocean, the meridional gradient between extra-tropical cooling and tropical heating helps  
461 produce a strong pressure gradient associated with low-level moisture transports into EA (Fig.  
462 5B), but over the western and central equatorial Indian Ocean a zonal east-west heating gradient  
463 (Fig. 5B) helps set up an east-west response in vertical velocities (Fig. 5C) that helps suppress  
464 rainfall over the eastern Horn.

465  
466 We next explore ERA5 SSTs and atmospheric heating anomalies following the 12 recent post-  
467 1997 OND La Niña events, which we also refer to as ‘MAM WVG events’ (Fig. 5D-E), because  
468 all of these events have strong negative WVG values in MAM (Figure 2C). Composites based on  
469 actual MAM WVG values and EHoA MAM dry seasons all resemble Fig. 5D-E. We chose to  
470 use OND La Niña events to emphasize opportunities for long-lead prediction of MAM droughts  
471 following La Niña-related OND dry seasons.

472  
473 A composite mean of the post-OND-La Niña MAM SST anomalies has a WVG structure (Fig.  
474 5D), but also reveals interesting SST cooling in the central Indian and warming in the  
475 southwestern Indian Ocean. This Indian Ocean SST gradient is associated with moisture  
476 transport anomalies that flow from over the southern Indian Ocean, and then turn east, towards  
477 the eastern Indian Ocean (Fig. 5E). These transport anomalies exhibit enhanced anticyclonic  
478 flow around that deflects moisture southward along the western flank of the Mascarene High.  
479 This is consistent with findings of Wainwright et al. [Wainwright et al., 2019] indicating that the  
480 late onset in MAM rainfall is linked with warmer SSTs over the south western Indian Ocean by  
481 delaying the northward movement of the tropical rainfall belt.

482  
483 These MAM WVG events are associated with large statistically significant changes in  
484 atmospheric heating in the Indo-Pacific Warm Pool (100-150°E, 15°S-15°N) and Central Pacific  
485 (150°E-170°W, 8°S-6°N) (Fig. 5D, Table 2). These results identify a very large westward  
486 transition in equatorial western-central Pacific heating. Driven both by diabatic heating and heat  
487 convergence, these large shifts indicate a westward shift of peak atmospheric heating, with  
488 increased subsidence near the equatorial dateline, increased equatorial Pacific moisture and heat  
489 transports, and increased Warm Pool heating.

490  
491 Over the Indian Ocean we also see an interesting, and statistically significant, increase in  
492 atmospheric heating over the Northern Indian Ocean (60-100°E, 15°S-6°N), and some small  
493 atmospheric heating decreases over the central Indian Ocean (60-100°E, 15°S-6°N) (Fig. 5E).  
494 Dry season SST composites (Fig. 2A) show fairly large (-1.2 to -0.6Z) and significant cooling  
495 anomalies over the central Indian Ocean as well, contributing to an enhanced equatorial SST  
496 gradient between the central Indian Ocean and the Warm Pool. Increased Warm Pool and North  
497 Indian Ocean atmospheric heating, combined with less heating over the Central Indian Ocean  
498 appears associated with anomalous westerly moisture transports across the equatorial Indian  
499 Ocean, away from EA. This can be seen as an eastward shift of the climatological transport  
500 fields, which typically flow into EA (Fig. 5B). These exchanges of heat and moisture modulate

501 the Walker Circulation, increasing heating and moisture convergence over the Warm Pool and  
502 northern Indian Ocean, and decreasing these quantities over the central Indian and Pacific Ocean.  
503 Table 2 lists the diabatic heating, heat convergence, and moisture convergence anomalies for  
504 recent WVG events and 1981-2022 dry EA MAM seasons. Energy terms are in  $\text{Wm}^{-2}$ , while  
505 moisture convergence is in total mm per MAM season. Increases in convergence in the Warm  
506 Pool and Northern Indian Ocean are highly significant and large.

507  
508 As discussed in the methods section, areas of increased or decreased atmospheric heating also  
509 correspond to areas with decreasing or increasing divergence of geopotential height energy (Fig.  
510 4), because heating and geopotential height energy are tightly coupled in a hydrostatic  
511 atmosphere [Peixoto and Oort, 1992]. In the Central Pacific and Central Indian Ocean, increased  
512 geopotential height energy stabilizes the atmosphere and increases surface pressures. Conversely,  
513 in the Warm Pool and northern Indian Ocean, we find increased height divergence and lower  
514 surface pressures. This supports strong zonal moisture and heat transport anomalies flowing from  
515 over the Central Indian and Pacific into the Warm Pool (Fig. 5E).

516  
517 Correlations of equatorial 1981-2022 WVG/ERA5 vertical and zonal velocities and specific  
518 humidity (Fig. 5F) reveal a Walker Circulation enhancement, consisting of a Warm Pool versus  
519 central Pacific dipole, and a weaker but still significant response over the Indian Ocean. The  
520 latter appears associated with subsidence in the middle and lower troposphere, westerly wind  
521 anomalies, and reduced atmospheric water vapor in the lower half of the troposphere between  
522  $40^{\circ}\text{E}$  and  $100^{\circ}\text{E}$ . As discussed above, climatological conditions relate equatorial Indian Ocean  
523 Warm Pool atmospheric heating to offsetting factors: moisture transports across the southern  
524 Indian Ocean (Fig. 5AB), and subsidence between  $40^{\circ}\text{E}$ - $55^{\circ}\text{E}$ . WVG events increase atmospheric  
525 heating over the northern Indian Ocean and decrease atmospheric heating over the central Indian  
526 Ocean (Fig. 5E, Table 2), while also increasing the zonally overturning Walker Circulation (Fig.  
527 5F). Over East Africa, this reduces atmospheric moisture and vertical motions in the mid-  
528 troposphere (Table 3).

529  
530 Strong links between an enhanced Walker Circulation and dry outcomes during the EA MAM  
531 season are shown in Figure 6A,C. These scatterplots identify the very strong covariation between  
532 Warm Pool heating and moisture convergence (ERA5  $R=0.99$ , MERRA2  $R=0.98$ ,  $p=0.0001$ ).  
533 This strong correlation is not surprising. Heat and moisture transports are very similar, being  
534 driven primarily by low-level winds. Increased moisture convergence increases precipitation and  
535 latent heating (Eq. 4). More moisture increases the trapping of longwave radiation. What is  
536 striking, however, is 1) how variable these terms are, and 2) how well intense heating and  
537 moisture convergence discriminates dry EA seasons, as indicated by the circle colors.

538  
539 The first point matters. If year-to-year variations in the Warm Pool were small, they would not  
540 be likely drivers of EA droughts. But what we see in the ERA5 and MERRA2 are very large  
541 ranges, with heating and moisture convergence ranging from  $\sim 150$  to  $\sim 700 \text{ Wm}^{-2}$  and  $\sim 50$  to  
542  $\sim 350 \text{ mmMAM}^{-1}$ . These data exhibit a  $\sim$ six-fold change between the weakest and strongest  
543 seasons. During the more intense seasons, when ERA5 heating exceeds  $\sim 500 \text{ Wm}^{-2}$ , as indicated  
544 by the vertical black line in Fig. 5A,C, we see frequent dry EA outcomes and few wet or normal  
545 seasons. Furthermore, the circle with black crosses reveal that many of these strong  
546 heating/convergence years are strong MAM WVG events that followed OND La Niñas. OND La

547 Niñas are very robust indicators of strong MAM Warm Pool heating and moisture convergence  
548 ... up to six months in the future. Interestingly, the 2018 WVG was associated with low heating  
549 and convergence values, and very heavy rains, likely due to the influence of sub-seasonal MJO  
550 and cyclone influences [Kilavi *et al.*, 2018]. It should be noted, also, that moderate and low  
551 heating/convergence outcomes have few droughts, but there does not appear to be a strong  
552 connection to wet season frequencies. These results support the idea that dry seasons are  
553 predictable because of links to Pacific SSTs (Fig. 2A), while wet seasons are less predictable  
554 (Fig. 2B), because forcing from Warm Pool is limited.

555  
556 Scatterplots showing Warm Pool heating and Western V SSTs (Fig. 6B,D) also support links  
557 between Western V warming, Walker Circulation enhancements and frequent EA droughts.  
558 Warm Pool heating is strongly linked to warmer Western V SSTs. The 1981-2022 correlations  
559 between Western V SSTs and ERA5 and MERRA2 atmospheric heating are 0.74 and 0.70 (df.  
560 40,  $p=0.0000001$ ). Very warm Western V SSTs are clearly associated with increased Warm Pool  
561 atmospheric heating, and when Western V SSTs exceed +0.8Z, we find frequent dry EA rainy  
562 seasons (8 out of 12 seasons). We have already discussed the strong link between Western V  
563 SSTs and human-induced warming (Fig. 3A,B).

564  
565 Past research [Funk *et al.*, 2018; Funk *et al.*, 2019] has described how warm Western V and  
566 Western North Pacific SSTs are associated with ridging aloft, producing high pressure anomalies  
567 that encircle the twin equatorial upper lows associated with La Nina events, as represented by the  
568 Matsuno-Gill model [Gill, 1980]. The twin upper-level lows are at  $\sim 150^\circ\text{W}$ , at  $\sim 15^\circ\text{S}$  and  $15^\circ\text{N}$ ;  
569 while upper-level ridging is located both in the extra-tropical Pacific ( $\sim 170\text{-}150^\circ\text{W}$ ,  $\sim 45^\circ\text{S}$  and  
570  $\sim 45^\circ\text{N}$ ) and over the equatorial Western Pacific ( $\sim 150^\circ\text{E}$ ,  $20^\circ\text{S}$ - $2^\circ\text{N}$ ; Figures 5 and 6 in  
571 reference[Funk *et al.*, 2018]). These figures show that the resulting geopotential height gradients  
572 disrupt the sub-tropical westerly jets, increasing upper-level geopotential height convergence  
573 near the equatorial Central Pacific, amplifying the easterly flows of heat and moisture into the  
574 Warm Pool, and disrupting the Indian Ocean branch of the Walker Circulation.

575  
576 Figures 5 and 6 highlight opportunities for prediction. As highlighted by the repeated use of  
577 green crosses, OND La Niñas are associated with predictable negative MAM WVG values (Fig.  
578 2C) and strong Warm Pool atmospheric heating, and moisture convergence, and very warm  
579 Western V SSTs (Fig. 6). Over eastern East Africa, ERA5 and MERRA2 indicate highly  
580 significant and large ( $\sim 1$  sigma) decreases in total precipitable water during strong WVG MAM  
581 seasons; in the mid-troposphere subsidence also increases significantly (Table 3). Often arising  
582 in conjunction or after an OND La Niña event, these teleconnections set the stage for sequential  
583 but often predictable dry seasons. Thus La Niña-related MAM droughts are predictable because  
584 of reliable and predictable WVG conditions (Fig. 2D, 5D), and Walker Circulation  
585 enhancements (Fig. 5E, Fig. 6).

586  
587 This section has focused on the 1981-2022 satellite-observation period, for which we have good  
588 rainfall observations, reanalyses and SSTs. Over this period, we can say with great certainty that  
589 most MAM EA dry seasons were associated with more heating and moisture convergence in the  
590 Warm Pool and northern Indian Ocean, following La Niñas, when there have been predictable  
591 very warm Western V and WVG SST conditions. We next shift to a 1950-2022 time period to

592 examine the ‘East African Enigma’, to better understand some of the predominant features that  
593 differentiate “modern era” post-1997 La Niña events from earlier ones.

594

### 595 **4.3 Contrasting MAM circulations following 1998-2022 and 1950-1997 OND La Niñas**

596

597 An important, but analytically challenging, aspect of the EA Paradox is a potential shift in links  
598 to La Niña. There is general agreement on a shift in Pacific SST following the 1997/98 El Niño  
599 [*L’Heureux et al.*, 2013; *Lyon et al.*, 2013; *Yang et al.*, 2014]. Following this event, Western V  
600 SSTs increased [*Funk et al.*, 2019] and the Western V Gradient decreased substantially (Fig. 2C).  
601 Since the early 2010s, it has been hypothesized that the interaction of La Niña events and a low-  
602 frequency warming [*Williams and Funk*, 2011] may enhance the link between La Niña and dry  
603 EA MAM seasons, and recent work on this important topic [*Park et al.*, 2020] shows clearly the  
604 increasing correlation between boreal winter ENSO SSTs and EA rains in the following MAM  
605 season. Park et al. (2020) describe how a westward intensification of the Walker Circulation  
606 enhances links to Pacific SST variations, with 2000-2016 zonal equatorial vertical velocities, 200  
607 hPa velocity potential and winds exhibiting ENSO teleconnections between 50°E and 180°E.

608

609 The recent availability of 1950-2022 ERA5 reanalysis, gives us an exciting opportunity to map  
610 the change in atmospheric heating and moisture convergence during the MAM seasons following  
611 the 12 post-1997 OND La Niñas versus the 12 1950-1997 La Niñas. While not identical, these  
612 results (Fig. 7A) broadly resemble WVG events (Fig. 5E), this implies a change in the behavior  
613 of the ‘modern’ MAM seasons that follow OND La Niñas. Fig. 7A indicates stronger  
614 atmospheric cooling and higher low-level air pressures over the southeastern Indian Ocean and  
615 central Indian Ocean, and an interesting negative IOD-like heating increase in atmospheric  
616 heating over the eastern equatorial Indian Ocean, i.e. an intensification of the Indian Ocean  
617 branch of the Walker Circulation. This increased atmospheric heating appears associated with  
618 higher pressures over the central Indian Ocean, and northward moisture transport anomalies that  
619 cross the equator near 75°E and turn towards Indonesia. In a sense, the eastward edge of the  
620 climatological moisture transports over the Indian Ocean (Fig. 5A) has shifted east, increasing  
621 over the central Indian Ocean (yellow arrow in Fig. 7A). Stronger eastward transports from over  
622 the central Pacific feed more heat and moisture into the Indian Ocean Warm Pool. This pattern is  
623 not associated with the western Indian Ocean, but rather the difference between the tropical  
624 central Indian Ocean and the Indo-Pacific Warm Pool, where WVG SST composites also  
625 indicate a dipole structure (Fig. 5D,E).

626

627 Given the strong relationship between dry EA seasons and Warm Pool atmospheric heating (Fig.  
628 6A,C), we can contrast ERA5 MAM Warm Pool heating Probability Distribution Functions  
629 (PDF) for pre-and-post 1997 La Niña events (Fig. 7B). A  $\sim 110 \text{ Wm}^{-2}$  increase in heating is  
630 identified, and this distribution shift increases the probability of exceeding a  $500 \text{ Wm}^{-2}$  threshold  
631 from 24% to 58%. Recent OND La Niñas anticipate much more energetic MAM Walker  
632 Circulations. These results can help explain why predicted WVG events (Fig. 2D) are good  
633 indicators of elevated EA MAM drought risk, and why there has been a large shift in EA MAM  
634 SPI PDFs following pre-and-post 1998 La Niña events (Fig. 7C). Since 1998, when there has  
635 been an OND La Niña, there have been strong MAM WVG gradients (Fig. 2C), very warm  
636 Western V SSTs (Fig. 5D), and strong Warm Pool heating and convergence (Fig. 6). These

637 results, and the large and significant changes shown in Fig. 7A, help explain why 75% of the  
638 time EA MAM rains are poor, when a La Niña arrives during boreal fall.

639  
640 It is important to note, however, that dry EA MAM seasons are linked to the overall Pacific SST  
641 gradient structure, not just the NINO3.4 region (Fig. 2A). For example, during three of the nine  
642 seasons with boreal fall La Niña and dry MAM outcomes (2001, 2009, 2017), NINO3.4 SST  
643 values did not meet the ONI La Niña criteria during MAM, yet these seasons had strong negative  
644 WVG values and large Warm Pool heating values [ $>460 \text{ Wm}^{-2}$ ]. Looking to the large-scale  
645 WVG more extensively resolves the large-scale SST patterns that arise from the interaction of  
646 natural ENSO variability and anthropogenic warming trends. The next section discusses the  
647 latter more in detail.

#### 648 649 **4.4 Relating Warm Pool heating and more frequent droughts to anthropogenic warming in** 650 **the Western V**

651  
652 We next explore low frequency (20-yr) links between MAM Pacific SSTs, Warm Pool heating,  
653 and EA dry season frequencies. The value of diagnostic analyses focused on atmospheric heating  
654 and moisture transport/convergence patterns (i.e. sections 4.2 and 4.3) is that they enable us to  
655 quantify the changes in climatic forcing associated with SST gradients. The WVG, by itself, is  
656 somewhat arbitrary, given that we weight equally the standardized Western V and NINO3.4  
657 regions. While studies examining the ENSO-residual West Pacific Warming Mode (WPWM)  
658 have suggested that Western V-like SSTs amplify the Walker Circulation [*Funk and Hoell, 2015;*  
659 *2017*], an important question that we address here is ‘*how influential is the Western V, in*  
660 *comparison with ENSO, as represented by NINO3.4 SST?*’.

661  
662 To set the stage for this analysis, we briefly present an updated analysis (Fig. 8) of the 1900-  
663 2022 ENSO and WPWM principal components (PC), as in Funk and Hoell (2015). ENSO in this  
664 study, as in [*Lyon et al., 2013*], is represented by the first EOF/PC of tropical Pacific SSTs. This  
665 PC tracks closely with SST in the NINO3.4 region (Fig. 8A). The ENSO PC and NINO3.4  
666 average SST time-series have a 1950-2022 correlation of 0.94. To estimate the WPWM, each  
667 grid cell’s MAM SST is regressed against the ENSO PC. Then the 1<sup>st</sup> EOF of the global  
668 residuals is used to define the WPWM, which tracks closely with the Western V. The WPWM  
669 PC and Western V average SST time-series have a 1950-2022 correlation of 0.87. An identical  
670 calculation of the WPWM, based on large ensembles of climate change models, are very similar  
671 to the observed patterns [*Funk and Hoell, 2015; 2017*]. Western V warming is not primarily  
672 driven Pacific Decadal Variability. Time-series of the WPWM/ENSO PCs (Fig. 8C) and Western  
673 V/NINO3.4 (Fig. 8D) are very similar. In broad strokes, two transitions appear in these time-  
674 series. First, the ENSO/NINO3.4 time-series have a Pacific Decadal Oscillation-related [*Mantua*  
675 *and Hare, 2002*] increase in the late 1970s, but thereafter show little increase [*Seager et al.,*  
676 *2022*]. Then, the WPWM/Western V trends upward, with post-1998 values being especially  
677 warm. It is worth noting that the MAM 2022 WPWM and Western V values appear to be, by a  
678 substantial margin, the warmest on record.

679  
680 We next use linear regression to relate 20-yr MAM Western V and NINO3.4 SST values to 20-yr  
681 1950-2022 ERA5 Warm Pool atmospheric heating. The blue bars in Fig. 9A show 20-yr average  
682 ERA5 Warm Pool Atmospheric heating. Between the first and last 20-year period we see a

683 substantial increase, from  $\sim 330$  to  $\sim 420$   $\text{Wm}^{-2}$ . Interestingly, a regression based on 20-yr  
 684 standardized Western V and NINO3.4 SST can explain 97% of the atmospheric heating variance.  
 685 The Western V and NINO3.4 coefficients are highly significant and roughly similar in  
 686 magnitude (58 and 67  $\text{Wm}^{-2}$  per standardized anomaly). These results are shown with a green  
 687 line in Fig. 9A. A regression carried out with just 20-yr Western V (red line Fig. 9A) explains  
 688 76% of the observed variance. Most of the 20-yr variance of the Warm Pool heating can be  
 689 explained by Western V warming. To examine the contribution of climate change, we can use  
 690 this equation ( $\text{HEAT}_{\text{WV}} = 386 + 44 * \text{Western V SST}$ ), but replace the observed Western V values  
 691 with the median of our large CMIP6 ensemble (Fig. 3A). These results are labeled as F(WestV-  
 692 CMIP6-50<sup>th</sup> Percentile SST) in Fig. 9A. 20<sup>th</sup> and 80<sup>th</sup> percentile CMIP6 estimates are also shown.

693  
 694 We would interpret these results as follows. First, the WVG formulation, which gives equal  
 695 weight to the Western V and NINO3.4 regions, seems fairly justified at 20-yr time-scales. 20-  
 696 year Warm Pool atmospheric heating covaries with both 20-yr NINO3.4 and Western V SSTs,  
 697 which in turn track closely with the first two models of global SST variability (Fig. 8). Between  
 698 the 1970s and 1990s a largely natural increase in NINO3.4 SSTs occurred [*Mantua and Hare,*  
 699 2002] (Fig. 3C), and we also see this reflected in the Warm Pool heating regression estimate,  
 700 which declined by about 40  $\text{Wm}^{-2}$  during this period. However, since the 1980s, the Western V  
 701 warmed substantially, and we find this associated with a large  $\sim 80$   $\text{Wm}^{-2}$  increase Warm Pool  
 702 heating.

703  
 704 Is the recent Western V warming largely due to climate change, or natural decadal variability?  
 705 While some studies, using detrended SSTs, have argued that western Pacific warming is largely  
 706 natural [*Lyon, 2014; Yang et al., 2014*], it is possible that the detrending process used in these  
 707 studies introduces biases into the results, since the rates of external forcing and associated  
 708 warming increase non-linearly. Assuming climate change is linear, and that residuals are  
 709 'natural' can miss the rapid human-induced warming present in the 1990s-2020s (Fig.3A). A  
 710 simpler approach is to compare directly observed 20-yr Western V SSTs with estimates from the  
 711 CMIP5 [*Funk et al., 2019*] or CMIP6 (Fig. 3A, Fig. 8A). CMIP6 20-yr Western V SST tracks  
 712 extremely well with the observations (median time series,  $R=0.98$ , 1950-2022). The heavy black  
 713 line in Fig. 9A translates the median CMIP6 Western V SST values into Warm Pool atmospheric  
 714 heating, in  $\text{Wm}^{-2}$ , using the empirical Western V regression coefficients. Differences between the  
 715 observed (red line) and externally-forced CMIP6 (heavy black line) 20-year Western V time-  
 716 series indicate the influence of natural Pacific Decadal Variability. These fluctuations are limited  
 717 to a small cooling in the 1980s and warming in the late-2000s. The dominant change in observed  
 718 20-yr running average Western V (red line) - the increasing trend - aligns with human-induced  
 719 warming (black lines). Between 1950 and 2022, CMIP6 Western V SST estimates suggest an  
 720 overall increase in Warm Pool atmospheric heating from  $\sim 340$  to  $\sim 410$   $\text{Wm}^{-2}$ . This shift in mean  
 721 Warm Pool heating is augmented further following recent La Niña events (Fig. 7A), helping to  
 722 explain the enigmatic increase in dry EA MAM seasons (33%  $\rightarrow$  75%, Fig. 7C).

723  
 724 Over the past 75 years, Western V SST have warmed by  $\sim +2Z$  standardized anomalies, and this  
 725 warming shifts the heating distribution by more than  $+80\text{Wm}^{-2}$ . Projections through 2050 suggest  
 726 another similar increase over the next 30 years (Fig. 9A). Such heating influence will likely be  
 727 particularly dangerous during or following La Niñas, setting the stage for more frequent  
 728 sequential OND/MAM droughts.

729  
730 In contrast to Western V SSTs, there is a large and growing discrepancy between observed east  
731 Pacific SSTs and CMIP6 projections, with “*observations-based SST trends ... at the far edge or*  
732 *beyond the range of modeled internal variability*” [Seager et al., 2022], there has been a notable  
733 lack of warming in the NINO3.4 region, and this is in marked contrast to 20-yr anomalies from a  
734 25-model 152-member ensemble of CMIP6 simulations (Fig. 3D). The observed 2003-2022  
735 value (-0.09Z) is extremely unlikely given the distribution from the CMIP6 simulations  
736 (Supplemental Fig. 4B). More detailed analyses [Wills et al., 2022] identify “*a triangular region*  
737 *in the eastern tropical and subtropical Pacific*” as the ocean region where CMIP6 model  
738 simulations differ most from observations, with the differences very unlikely (<5% probability)  
739 due to internal variability. While a detailed exploration is beyond the scope of this study,  
740 systematic Pacific SST biases are one likely cause of this discrepancy, and when bias-corrected  
741 ocean and atmosphere models are used to explore this issue, they recreate the observed increase  
742 in equatorial Pacific zonal SST gradients [Seager et al., 2019]. Hence assuming that the climate  
743 change models are ‘correct’ and that the observed lack of warming is driven by naturally-  
744 occurring Pacific Decadal Variability appears problematic.

745  
746 Finally, we present regressions relating 20-yr NINO3.4 and Western V SSTs to 20-yr dry season  
747 frequencies, i.e. the number of times in each 20-yr period in which EA MAM SPI was less than -  
748 0.44Z (Fig. 9B). The F(Observed WestV SST) time-series denotes a set of probability estimates  
749 derived via a linear regression using observed Western V SSTs as a predictor and 20-yr running  
750 observed frequencies of dry East African seasons as a predictand: ( $\text{PROB}_{\text{dry}} = 0.3 + 0.13\text{WV}$ ,  
751  $R^2 = 0.74$ ). Western V SST increases can explain most of the 20-yr variance in 20-yr changes in  
752 the frequency of dry seasons. These results suggest that the Western V warming has been a  
753 primary driver of increased dry season frequencies in the eastern Horn of Africa. Since Western  
754 V warming has been dominated by human-induced external forcing, climate change has been a  
755 strong driver of increased dry season frequencies in East Africa.

756

## 757 **5 Conclusions**

758

### 759 **5.1 A Walker Circulation intensification can explain the enigma predictability of the EA** 760 **MAM rains.**

761

762 Here, we have addressed a quite specific question – do intensifications of the Walker  
763 Circulations help explain the “East Africa Climate Enigma”, i.e. the fact that so many recent  
764 OND La Niñas are followed by below-normal MAM EA rainy seasons. Furthermore, how does  
765 this link relate to climate change and the large observed decline in EA MAM rains (Fig. 1B)? We  
766 have addressed these questions in a two-step attribution process. The first step links observed EA  
767 droughts to decreasing but predictable WVG values (Fig. 2). These strong Pacific gradients, we  
768 argue, are being produced through an interaction of naturally occurring La Niña events and  
769 human-induced warming in the Western V region (Fig. 2C, Fig. 3A,B). The second step then  
770 links WVG events to changes in the Walker Circulation and conditions over EA (Fig. 5-6, Tables  
771 2,3).

772

773 These 1981-2022 results paint a clear story that helps us understand the predictability of MAM  
774 dry seasons. First, we see a large, climate-change-related warming of the Western V region,  
775 well-reproduced in the CMIP6 (Fig. 3A,B). This warming, combined with the influence of La  
776 Niña, results in very reliable low WVG values during MAM seasons following OND La Niñas  
777 (Fig. 2C). These gradients, furthermore, are predicted well by seasonal climate prediction  
778 systems (Fig. 2D). MAM EA rains, furthermore, have very often been poor following post-1997  
779 OND La Niñas (Fig. 7C), consistent with increasing ENSO teleconnections [*Park et al.*, 2020].  
780

781 To make such insights more actionable, however, we have tried to provide a clear causal  
782 description linking WVG conditions to dry EA rains. To this end we have used gradients in  
783 atmospheric heating to help describe the Indo-Pacific Walker Circulation. In terms of the long  
784 term mean climate, these fields identify the regions of high and low pressure that help guide  
785 moisture transports into the Warm Pool and eastern Horn (Fig. 5B), which in turn help setup  
786 zonally-overturning wind patterns along the equator (Fig. 5C).  
787

788 Composites of SSTs, atmospheric heating and moisture transports, following post-1997 La  
789 Niñas, show significant and substantial changes in SSTs (Fig. 5D) and atmospheric  
790 heating and moisture transports (Table 2, Fig. 5E). These large and significant changes (Table 2)  
791 can be anticipated many months ahead of the MAM rains, since these composites are based on  
792 lagged OND La Niña definitions. Warm Pool intensification arises through both increased  
793 diabatic heating and increased heat and moisture convergence (Table 2). Over EA, we find  
794 corresponding decreases in total precipitable water and increases in mid-tropospheric subsidence  
795 (Table 3).  
796

797 Scatterplots of Warm Pool atmospheric heating and moisture convergence (Fig. 6A,C) very  
798 strongly support the link between Walker Circulation enhancements and dry EA outcomes.  
799 When ERA5 heating exceeded  $450 \text{ Wm}^{-2}$  there were 9 dry seasons, 2 normal seasons and 2 wet  
800 seasons. Strong Warm Pool heating in MERRA2 reanalyses similarly discriminate dry outcomes.  
801 As previously hypothesized, Walker Circulation enhancements are a robust indicator of dry EA  
802 outcomes. Twelve post-1997 La Niñas were precursors to MAM SST anomalies (Fig. 5D) that  
803 strongly resemble dry season SST composites (Fig. 2A). And the associated circulation  
804 disruptions (Fig. 5E, Fig. 7AB, Table 2) appear linked to frequent droughts (Fig. 1B), but offer  
805 opportunities for prediction (Fig. 2D). The energetic framework provided here helps us explain  
806 these opportunities. While we only have  $\sim 12$  events, we see that Warm Pool heating and  
807 moisture convergence increases dramatically during most of these seasons (Fig. 6A,C) and when  
808 compared to the MAM seasons following 1950-1997 La Niñas (Fig. 7A-B).  
809

810 Thus, without ruling out other influences such as westerly Congo Basin moisture transports and  
811 the MJO [*Finney et al.*, 2020], or sub-seasonal changes in the length of the long rains  
812 [*Wainwright et al.*, 2019], the results presented here support the idea that one primary cause of  
813 recent EA droughts has involved a large westward shift in atmospheric heating between the  
814 equatorial central Pacific and Warm Pool regions during WVG seasons. These regions exhibit  
815 the largest atmospheric heating anomalies. But, as shown by Gill [*Gill*, 1980], increased heating  
816 in the Warm Pool may increase subsidence and low-level pressures to the west, changing  
817 circulation patterns over the Indian Ocean, providing proximate impacts that reduce moisture and  
818 vertical ascent over East Africa. Early studies linking EA drying with an increased Indian Ocean

819 branch of the Walker Circulation posited atmospheric heating over the central Indian Ocean  
820 [Funk *et al.*, 2008; Verdin *et al.*, 2005]; the work presented here suggests heating increases over  
821 Indian and Pacific Warm Pool regions, and underscores the amplifying role played by moisture  
822 and heat transports and convergence. This helps explain the link with Pacific SSTs [Lyon and  
823 DeWitt, 2012; Yang *et al.*, 2014] as well as the tendency for the long rains to start later and end  
824 earlier [Wainwright *et al.*, 2019]. Such insights could assist in the prediction of onset and  
825 cessation dates, which are linked to zonal wind variations over the Indian Ocean [MacLeod,  
826 2018].

827  
828 Our WVG composites (Fig. 5D) also identify Indian Ocean SST warming over the southwest and  
829 northern Indian Ocean, and cooling near 75°E, 15°S. Recent analysis has suggested a later start  
830 and earlier cessation of the long rains [Wainwright *et al.*, 2019], and this may be consistent with  
831 the observed WVG SST responses, and expectations that La Niña-like conditions will tend to  
832 slow the onset and hasten then end of the rainy season. In the southern Indian Ocean, during  
833 WVG events (Fig. 5D), warmer southwestern SSTs could delay the typical northward  
834 progression of the rains between February and March. In the central and northern Indian Ocean,  
835 during WVG events (Fig. 5D,E, Table 2), warmer SSTs in the northern Indian Ocean (Fig. 5D)  
836 and increased atmospheric heating over the northern Indian Ocean, combined with cooler SSTs  
837 and less heating over the central Indian Ocean, might also help trigger an early transition to the  
838 boreal summer Indian Monsoon circulation, which could reduce rainfall in May. The contrasting  
839 heating responses over the northern and central Indian Ocean (Fig. 5E) help drive moisture and  
840 heat into the Warm Pool, and away from EA. This may suggest a ‘Walker Circulation  
841 Intensification’ over the northern Indian Ocean, perhaps leading to an earlier transition to a  
842 boreal summer monsoon pattern, similar to the June-August circulation. Hence, the increased  
843 frequency of strong WVG events, especially following recent La Niñas, appears related to the  
844 shorter EEA rainy season as described by Wainwright *et al.* [Wainwright *et al.*, 2019]. Climate  
845 change assessments, based on regional climate model results [Gudoshava *et al.*, 2020], have  
846 suggested that the long rains will start and end earlier. This earlier start projection, which appears  
847 at odds with the observations, may be related to a tendency for the global climate change models  
848 to predict an El Niño-like tendency in Pacific SSTs (Fig. 3C,D), and the well-established north-  
849 south rainfall dipole associated with ENSO, with southern (eastern) Africa being drier (wetter)  
850 during El Niños.

851  
852 In our La Niña atmospheric heating analysis (Fig. 7A), on the other hand, we find enhanced  
853 atmospheric heating primarily in the south-eastern Indian Ocean, where recent La Niñas appear  
854 associated with  $>160 \text{ Wm}^{-2}$  more heating than pre-1998 events. In the absence of strong Walker  
855 Circulation forcing, sub-seasonal influences such as the MJO, and more local weather influences  
856 such as westerly Congo basin moisture transports likely play an important role [Finney *et al.*,  
857 2020]. The MJO, of course, modulates the Walker Circulation and East African rains as well,  
858 and certainly influences heating and moisture transports. Recent research has linked a two-fold  
859 expansion of Warm Pool to a modulation of the MJO life cycle [Roxy *et al.*, 2019], with  
860 Maritime Continent residence times increasing by 5-6 days and Indian Ocean residence times  
861 decreasing by 3-4 days. Analyses of global satellite-gauge precipitation trends [Adler *et al.*,  
862 2017], have noted marked increases WVG-like SSTs, Warm Pool total precipitable water and  
863 precipitation (c.f. their Fig. 8), consistent with a strong equatorial Pacific SST gradient [Seager  
864 *et al.*, 2022; Seager *et al.*, 2019].

865 In closing, when one considers the ‘cause’ of the EA rainfall decline, we would suggest that it is  
866 useful to consider two aspects: the increased impacts following recent La Niña events, and the  
867 high frequency of recent La Niña events themselves. In place of the ‘East African Climate  
868 Paradox’ we have suggested the ‘East Africa Enigma’: why have La Niña-related SST conditions  
869 become such a consistent driver of droughts during MAM? Our analysis of atmospheric heating  
870 and changes in moisture transports help explain how the combination of anthropogenic Western  
871 V warming and La Niña events leads to increases in Warm Pool heating, which in turn  
872 modulates important circulation features over the Indian Ocean, increasing subsidence and  
873 decreasing EA moisture levels (Table 3). Hence, the interaction of climate change and frequent  
874 La Niña events have led to frequent MAM droughts, and many of those dry seasons have  
875 followed poor OND outcomes [*Funk et al.*, 2018]. This is consistent with recent multi-agency  
876 alerts attributing the recent droughts to the combined influence of La Niña and climate change.  
877 Without climate change, there would not be a strong link to La Niñas (Figure 7A,B). It is worth  
878 noting that strong ‘gradient La Niñas’ have been identified in observations [*Johnson*, 2013], and  
879 are expected by climate change models [*Cai et al.*, 2022; *Cai et al.*, 2015a; *Cai et al.*, 2015b].

880 For EA, our study has emphasized the strong relationship between MAM atmospheric heating,  
881 WVG SST and EA SPI, given the set of all post-1997 OND La Niña events. Such conditions  
882 pose risks, even if a La Niña event fades. When these events commence, enhanced trade winds  
883 transport more oceanic heat energy from the east Pacific and into the Western V region, via the  
884 sub-tropical gyre, and there is a great deal of certainty that these transports will persist for many  
885 months. As oceanic heat content increases due to climate change, it is not surprising to see that  
886 these natural La Niña transport patterns result in large increases in Western V SSTs, and more  
887 negative WVG values (Fig. 2C), which are very predictable (Figure 2D). Western V SSTs, even  
888 in the absence of very cool NINO3.4 SSTs, still increase flows of heat and moisture into the  
889 Warm Pool atmosphere, which increase the risk of dry EA rainy seasons. Even if the frequency  
890 of La Niñas were to decrease in the future, La Niñas will develop in an environment that is very  
891 warm- and likely even warmer than present-day- and the conditions in the Warm Pool and  
892 Western V will likely amplify the impacts of these La Niñas, setting the stage for sequential dry  
893 East Africa outcomes in OND and MAM. It is also possible, however, that observed streak of La  
894 Niñas will continue, due to a stronger zonal Pacific gradient. CMIP6-based projections of Warm  
895 Pool atmospheric heating, based on Western V warming, suggest a further  $\sim 80 \text{ Wm}^{-2}$  increase by  
896 2050 (Fig. 9A). Understanding the emergent links between La Niñas, WVG and the Walker  
897 Circulation will help anticipate and manage risks.

## 898 **Acknowledgments**

899 This research was supported by the United States Agency for International Development  
900 (USAID) (Cooperative Agreement #72DFFP19CA00001), National Aeronautics and Space  
901 Administration (NASA) GPM mission Grant 80NSSC19K0686, and the Bill and Melinda Gates  
902 Foundation contract INV-017546.  
903

## 904 **Availability Statement**

905 Please also note that we have produced a Dryad Data Repository with the time-series analyzed in  
906 this study. We have chosen a spreadsheet format to maximize accessibility. Even non-  
907 programmers can verify the basic results from our study. It is available at the link below.

908 <https://datadryad.org/stash/share/I2kn11CShPW0YDIUAA-La9IjaMHDmKLHoJzZYWCMmc8>

909

910 **Tables**

911

912 **Table 1.** The CMIP6 SSP245 models and simulations used in this study.

Model Names	Number of Simulations
ACCESS-CM2	3
ACCESS-ESM1-5	11
CanESM5-CanOE	3
CanESM5	25
CMCC-ESM2	1
CNRM-CM6-1-HR	1
CNRM-CM6-1	6
CNRM-ESM2-1	9
EC-Earth3-CC	1
EC-Earth3-Veg-LR	3
EC-Earth3-Veg	5
FGOALS-g3	4
FIO-ESM-2-0	3
GFDL-ESM4	3
GISS-E2-1-G	10
HadGEM3-GC31-LL	1
INM-CM4-8	1
INM-CM5-0	1
IPSL-CM6A-LR	11
MIROC6	3
MIROC-ES2L	30
MPI-ESM1-2-HR	2
MPI-ESM1-2-LR	9
MRI-ESM2-0	1
UKESM1-0-LL	5
<b>Total Number of Sims</b>	<b>152</b>

913

914

915

916

917 **Table 2.** Dry-Versus-West EA seasons and strong WVG season anomalies for selected forcing  
 918 regions. \*,\*\*,\*\*\* denote significance at  $p=0.1$ ,  $0.05$ , and  $0.01$ , based on two-tailed T-tests.  
 919 Moisture convergence is shown as the seasonal total moisture convergence.

	Warm Pool	Eq Central Pacific	Northern Indian	Central Indian
<b>Dry Seasons</b>				
Heat Convergence [ $\text{Wm}^{-2}$ ]				
ERA5	+78***	-85*	+51**	-32**
MERRA2	+95***	-130**	+42**	-14
Diabatic Heating [ $\text{Wm}^{-2}$ ]				
ERA5	+44***	-32	+29**	-13**
MERRA2	+77***	-55**	+45**	+3
Geopotential Divergence [ $\text{Wm}^{-2}$ ]				
ERA5	+108***	-112**	+67**	-51**
MERRA2	+128***	-178**	+63**	-16
Moisture Convergence [mm]				
MERRA2	+85***	-80	-45**	-49***
ERA5	+102***	-128**	-51**	-27*
<b>Strong WVG Seasons</b>				
Heat Convergence [ $\text{Wm}^{-2}$ ]				
ERA5	+123***	-178***	+81***	-49***
MERRA2	+133***	-206***	+74**	-36**
Diabatic Heating [ $\text{Wm}^{-2}$ ]				
ERA5	+66***	-81***	+48***	-19**
MERRA2	+95***	-114***	+86***	-40
Geopotential Divergence [ $\text{Wm}^{-2}$ ]				
ERA5	+169***	-250***	+110***	-76***
MERRA2	+172***	-287***	+160***	-91**
Moisture Convergence [mm]				
ERA5	+121***	-206***	+77***	-75***
MERRA2	+126***	-243***	+81***	-59

920

921

922

923

924 **Table 3.** Strong WVG season anomalies for Eastern East African MERRA2 and ERA5 Total  
 925 Precipitable Water and 600 hPa vertical velocities. \*, \*\*, \*\*\* denote significance at  $p=0.1$ , 0.05, and  
 926 0.01, based on two-tailed T-tests. Moisture convergence is shown as the seasonal total moisture  
 927 convergence. Anomalies also expressed as standardized anomalies. Eastern East Africa region  
 928 corresponds to 38-52°E, 5°S-8°N.

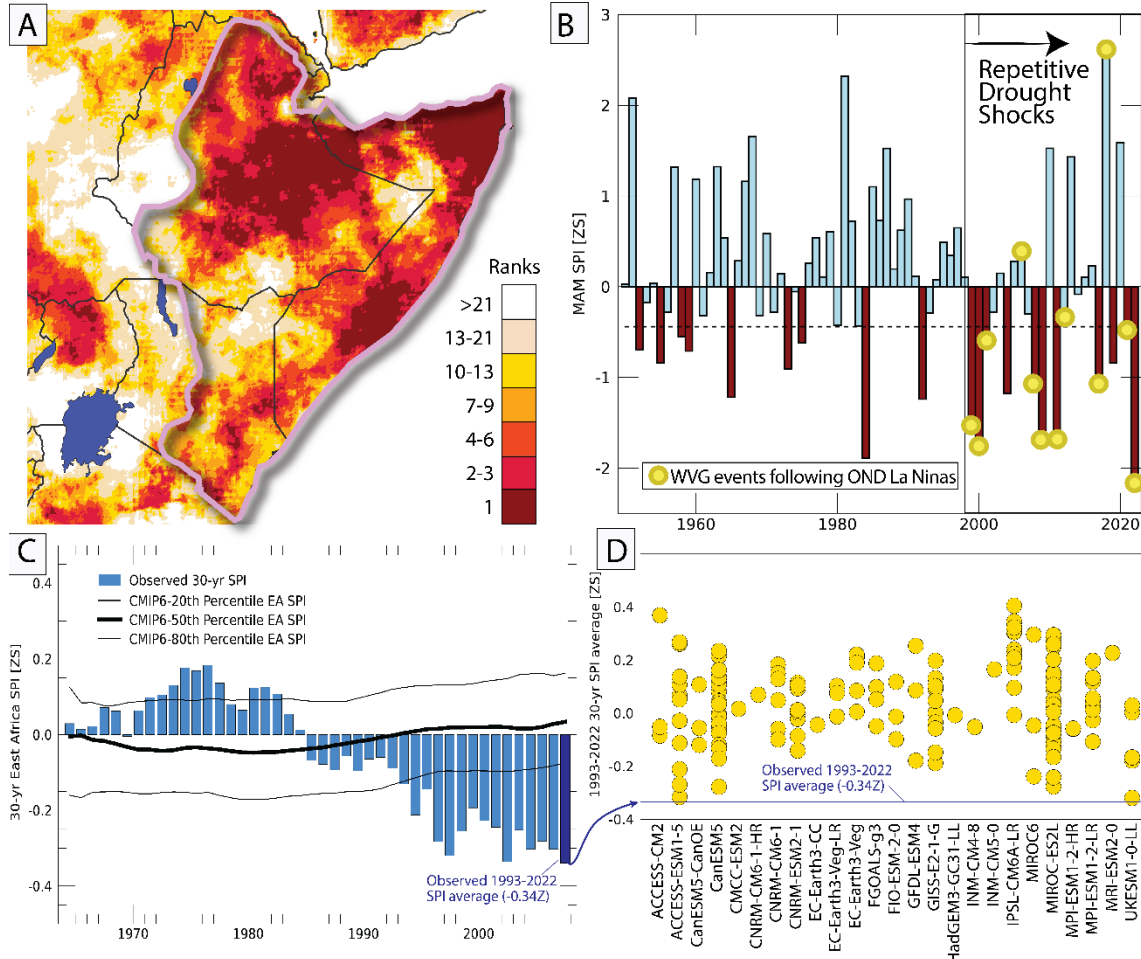
	Total Precipitable Water [ $\text{kgm}^2\text{s}^{-1}$ ]	Total Precipitable Water [Z-score]	600 hPa vertical velocity [ $\text{Pas}^{-1}$ ]	600 hPa vertical velocity [Z Score]
ERA5	-2.4***	-1.1Z***	+0.004**	+0.7Z
MERRA2	-2.2***	-1.0Z***	+0.003*	+0.5Z

929

930

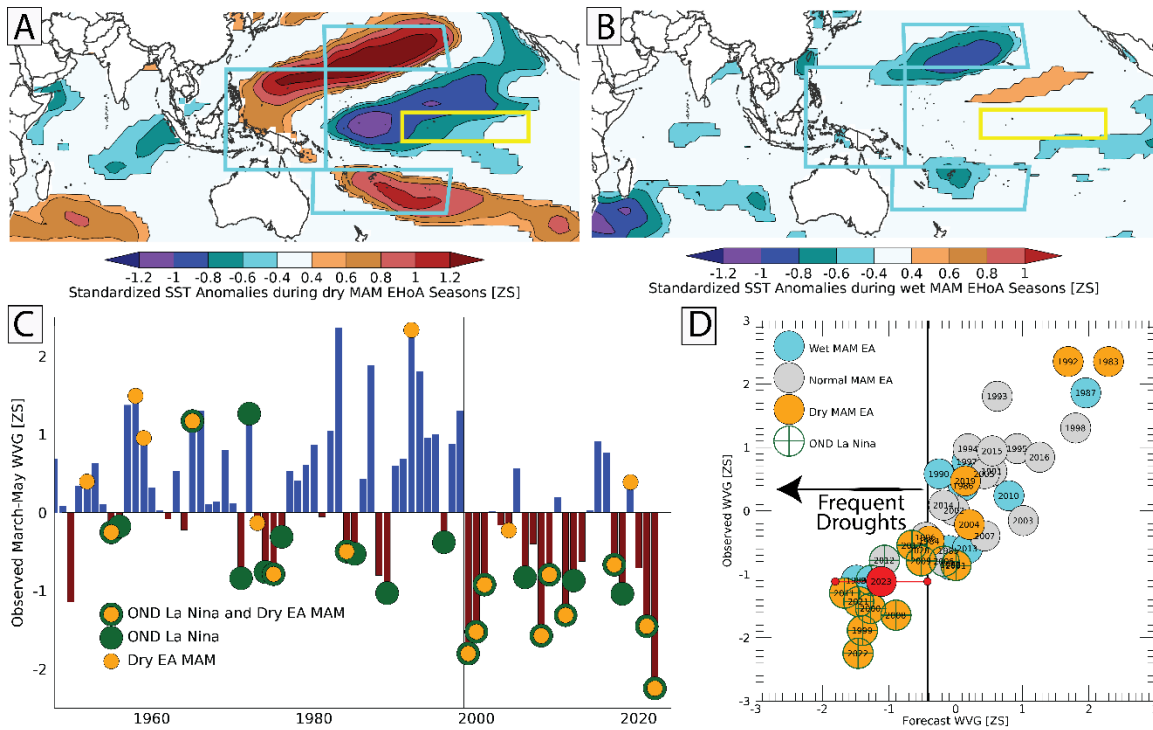
931

932 **Figures**  
 933

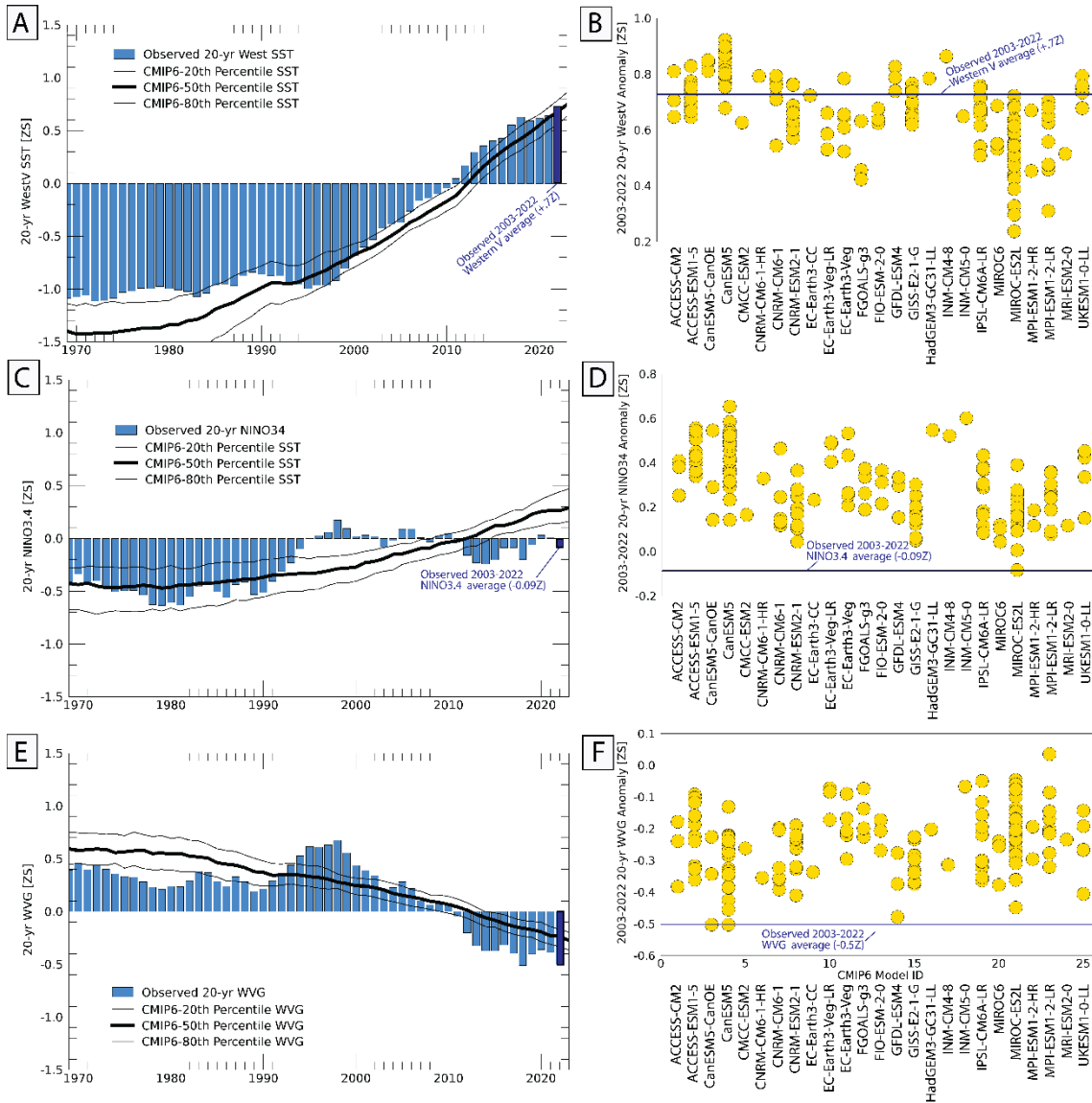


934 **Figure 1.** Describing the East African Climate Paradox. **A.** MAM 2022 rainfall ranks indicate  
 935 most of the Horn of Africa received extremely low rainfall amounts, based on 42 years of  
 936 CHIRPS rainfall. The purple polygon in Panel A denotes the area of exceptional dryness in  
 937 MAM 2022. **B.** Time-series of dry region MAM CHIRPS/Centennial Trends rainfall, expressed  
 938 as Standardized Precipitation Index (SPI) values). Also noted with yellow circles are strong  
 939 negative WVG seasons. **C.** Observed (blue bars) and projected CMIP6 SSP245 30-yr average  
 940 East Africa SPI. Centered on a 1981-2021 baseline. Based on 152 CMIP6 simulations. The thick  
 941 and thin black lines show the median and 20<sup>th</sup>/80<sup>th</sup> quantiles of the CMIP6 simulation  
 942 distribution. **D.** The 152 simulated CMIP6 2003-2022 20-yr average East Africa SPI, centered on  
 943 a 1981-2021 baseline. The horizontal line in Fig. 1D denotes the observed 1993-2022 average  
 944 East Africa SPI value (-0.34Z).  
 945

946  
 947  
 948

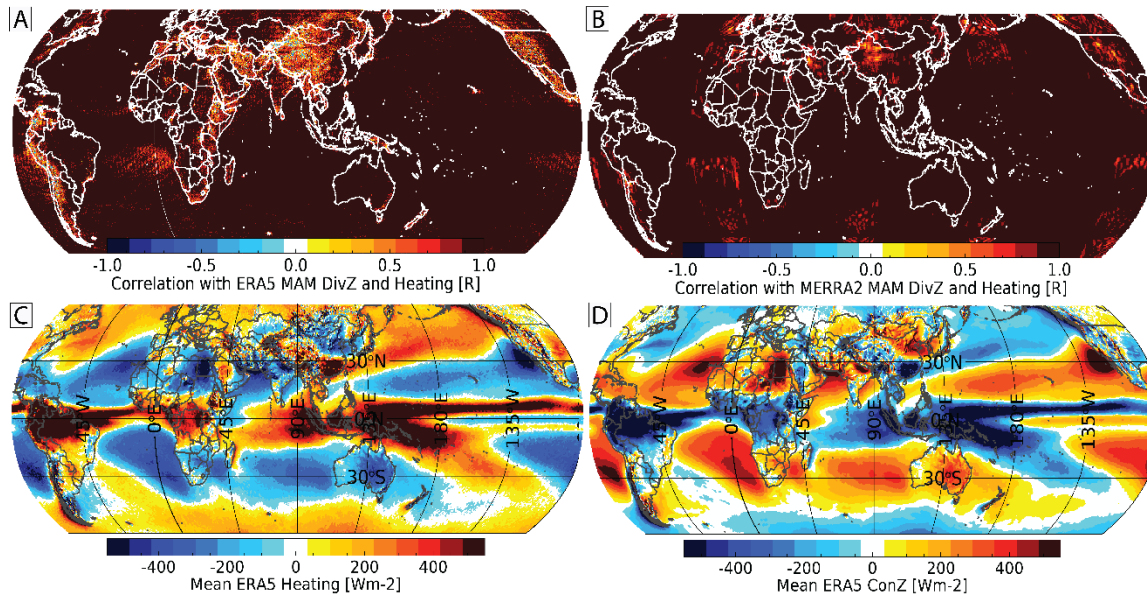


949 **Figure 2.** Relating dry seasons to the Western V gradient. **A-B.** Composites of standardized  
 950 SSTs during 1981-2022 dry seasons (**A**) and wet seasons (**B**) reveal a substantial non-linearity.  
 951 Dry seasons exhibit a coherent dipole pattern in the Pacific, while wet seasons SST anomalies  
 952 exhibit few areas with significant relationships. Wet and dry seasons based on 1981-2022 EA  
 953 SPI values of greater or less than +0.44 and -0.44. These breaks correspond with the top and  
 954 bottom tercile boundaries. Screened for significance at  $p=0.1$  using a two-tailed T-test. The cyan  
 955 boxes in A and B denote the equatorial [120-160°E, 15°S-20°N], northern [160°E -150°W, 20-  
 956 35°N], and southern [155°E -150°W, 30-15°S] regions of the ‘Western V’ area. The yellow box  
 957 denotes the NINO3.4 region in the eastern equatorial Pacific [170-120°W, 5°S-5°N]. The WVG  
 958 is the standardized difference between the NINO3.4 and Western V areas. **C.** A bar plot of  
 959 observed standardized MAM WVG values, centered on a 1981-2021 baseline. Orange circles  
 960 denote dry EA MAM seasons. Green circles denote preceding OND La Niña years. Orange  
 961 within green circles identify OND La Niña seasons followed by dry EA MAM events. The thin  
 962 vertical line at between 1998 and 1999 identifies the shift towards stronger WVG values and  
 963 more frequent dry EA MAM rainy seasons. **D.** Scatterplot showing forecasts of MAM WVG  
 964 index values, based on August NMME SST predictions. Observed MAM EA rainy season  
 965 outcomes shown with blue/gray/orange shading. All time-series and SST centered on a 1981-  
 966 2021 baseline. Also shown are preceding OND La Niña seasons, and the 2023 WVG forecasts.  
 967 The y-axis value has been set to the forecast value. 80% confidence intervals for the forecast are  
 968 also shown with small red circles and a horizontal red line.



970  
 971 **Figure 3.** Observed and CMIP6 SST time-series. **A.** Observed (blue bars) and CMIP6 SSP245  
 972 projections of 20-yr averages of standardized Western V SST anomalies. Centered on a 1981-  
 973 2021 baseline. CMIP6 results based on 152 CMIP6 simulations. The thick and thin red lines  
 974 show the median and 20<sup>th</sup>/80<sup>th</sup> quantiles of the CMIP6 simulation distribution. **B.** Individual  
 975 CMIP6 simulated 2003-2022 20-yr average Western V SST anomalies, centered on a 1981-2021  
 976 baseline. The horizontal line in Fig. 4B denotes the observed average 2003-2022 standardized  
 977 Western V SST anomaly (+0.7Z). **C-D.** Same but for standardized NINO3.4 SST anomalies. **E-**  
 978 **F.** Same but for standardized WVG index values.

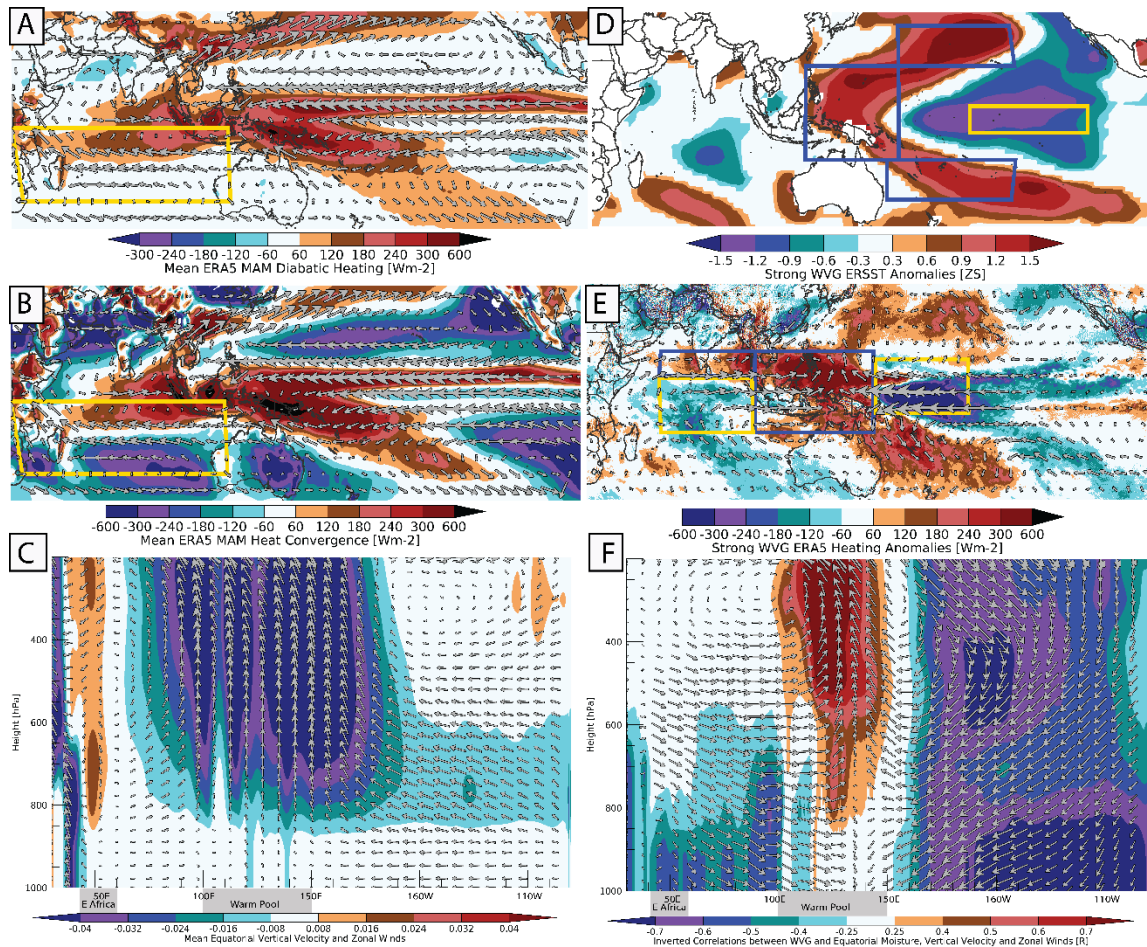
979



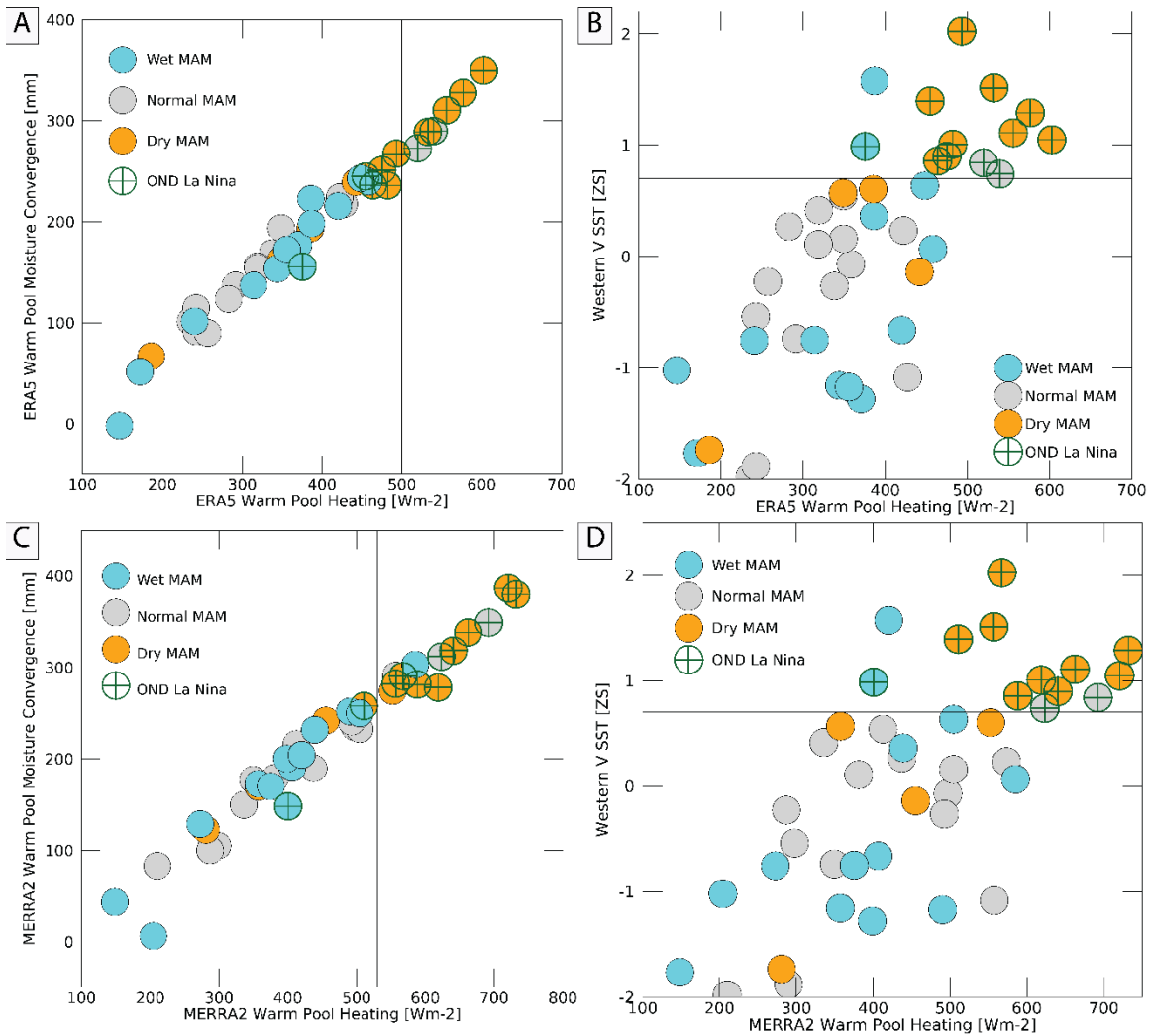
980  
981  
982  
983  
984  
985  
986  
987  
988

**Figure 4.** Geopotential height energy divergence offsets heating energy changes. **A-B.** 1981-2021 correlations between ERA5 (**A**) and MERRA2 (**B**) MAM atmospheric heating (diabatic heating + heat convergence) and geopotential height energy divergence. **C.** Long term (1981-2021) mean ERA5 atmospheric heating **B.** Same for geopotential height convergence.

989

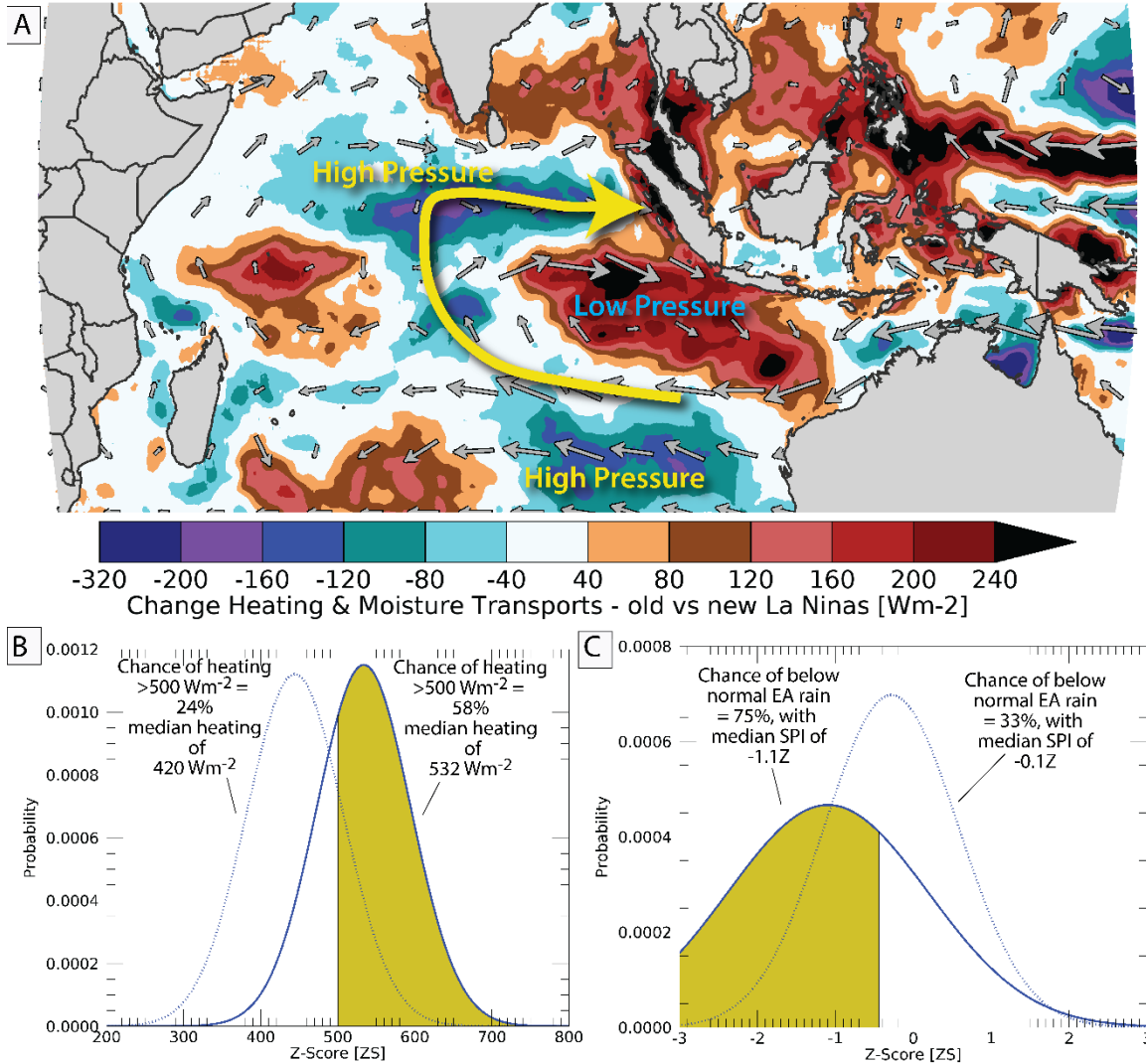


990  
 991 **Figure 5.** Relating WVG events to Walker Circulation intensification. **A.** Mean 1981-2021  
 992 ERA5 diabatic heating in  $\text{Wm}^{-2}$ . Vectors show ERA5 mean vertically-integrated moisture  
 993 transports, with a maximum westerly flux rate of  $-357 \text{ kgm}^{-1}\text{s}^{-1}$ . **B.** Same but for mean vertically  
 994 integrated atmospheric heat convergence. **C.** Long term mean ERA5 equatorial [ $5^{\circ}\text{S}$ - $5^{\circ}\text{N}$ ]  
 995 longitude-by-height vertical and zonal velocities ( $\text{Pas}^{-1}$  and  $\text{ms}^{-1}$ ). Vertical velocities scaled by  
 996 200. **D.** Composites of standardized MAM SSTs during 1981-2022 strong WVG events (circles  
 997 in Fig. 1B). Screened for significance at  $p=0.1$  using a two-tailed T-test. **E.** Similar composites  
 998 but for ERA5 atmospheric heating (diabatic heating + atmospheric heat convergence) in  $\text{Wm}^{-2}$ .  
 999 Screened for significance at  $p=0.1$ . Also shown are ERA moisture transport anomalies, with a  
 1000 maximum westerly flux rate of  $-174 \text{ kgm}^{-1}\text{s}^{-1}$ . Also shown are areas of interest: Indo-Pacific  
 1001 [ $100$ - $150^{\circ}\text{E}$ ,  $15^{\circ}\text{S}$ - $15^{\circ}\text{N}$ ], Central Pacific [ $150$ - $170^{\circ}\text{E}$ ,  $8^{\circ}\text{S}$ - $12^{\circ}\text{N}$ ], northern Indian Ocean [ $60$ -  
 1002  $100^{\circ}\text{E}$ ,  $5^{\circ}\text{N}$ - $15^{\circ}\text{N}$ ], and central Indian Ocean [ $60$ - $100^{\circ}\text{E}$ ,  $15^{\circ}\text{S}$ - $5^{\circ}\text{N}$ ]. **F.** 1981-2022 correlations  
 1003 between equatorial ERA5 vertical and zonal velocity and moisture (specific humidity) and  
 1004 inverted observed WVG values (the time-series shown in Supplemental Fig. 1A). Since negative  
 1005 vertical velocities (in  $\text{Pas}^{-1}$ ) indicate upward motions (panel C), the vertical velocity correlations  
 1006 have been inverted, to indicate that stronger WVG values are associated with increased ascent  
 1007 over the Warm Pool.



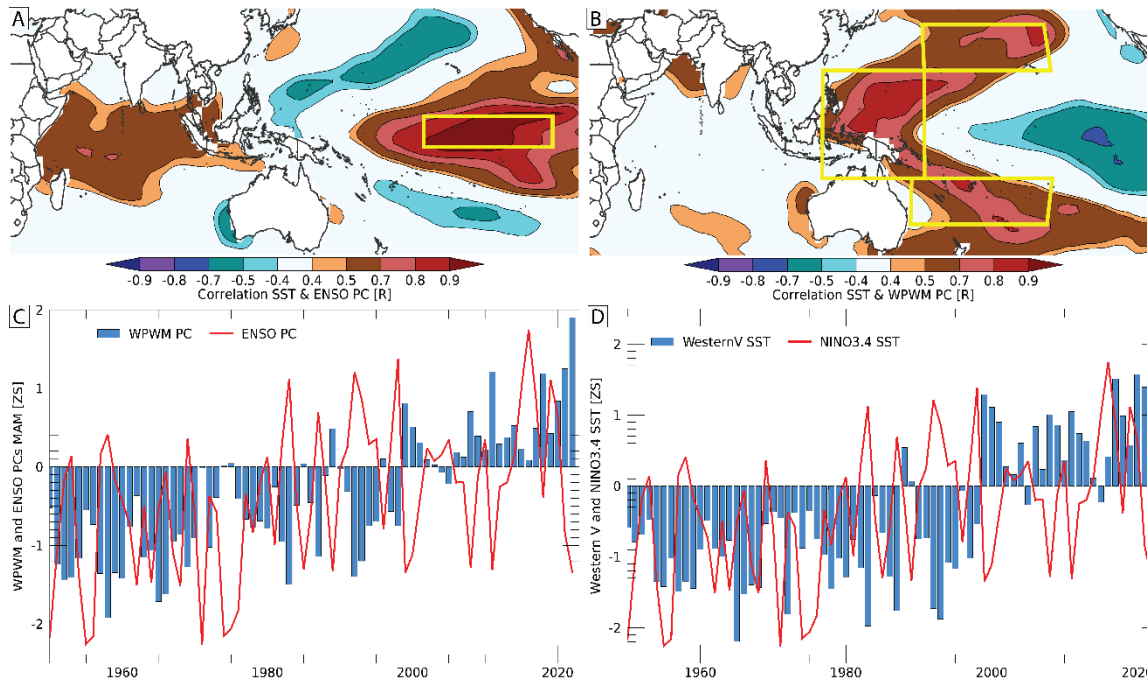
1008  
 1009  
 1010  
 1011  
 1012  
 1013  
 1014  
 1015  
 1016  
 1017

**Figure 6.** Increased Warm Pool atmospheric heating can help explain the East Africa Climate Enigma. Circle color denotes East African MAM rainfall terciles. Green crosses identify preceding OND La Niña seasons. **A.** A scatterplot of ERA5 MAM Warm Pool heating (x-axis) and Warm Pool moisture convergence (y-axis) **B.** A scatterplot of ERA5 Warm Pool heating (x-axis) and standardized MAM Western V SSTs (y-axis). Circle colors in **A** and **B** identify EA wet and dry MAM rainy seasons. **C-D.** Same but for MERRA2 reanalysis.

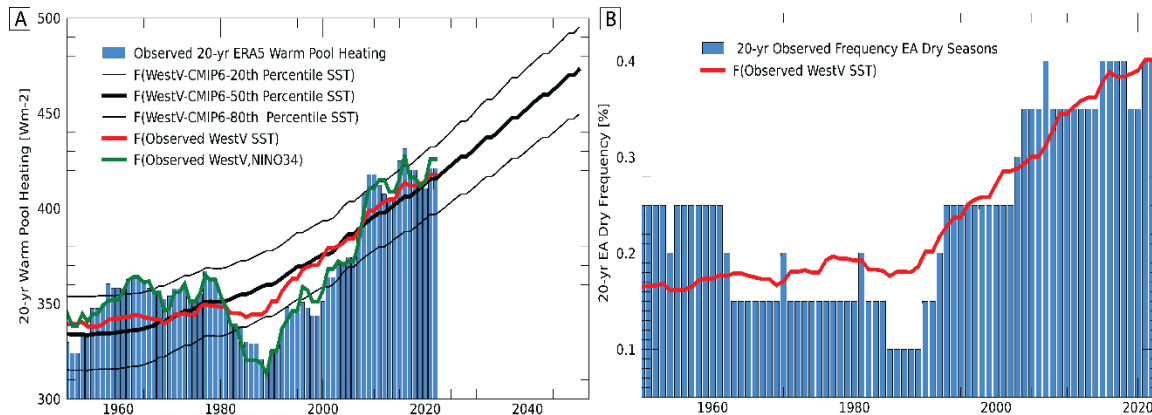


1018  
1019  
1020  
1021  
1022  
1023  
1024  
1025  
1026

**Figure 7.** Change in atmospheric heating following recent La Niñas can help explain the East Africa Climate Enigma. Circle color denotes East African MAM rainfall terciles. Green crosses identify preceding OND La Niña seasons. **A.** The difference between 1999-2022 and 1950-1997 ERA5 atmospheric heating and moisture transports in MAM seasons following OND La Niña events. **B.** PDFs of MAM West Pacific heating following pre- and post-1998 OND La Niña events. **C.** Same for observed EA MAM SPI (i.e. the data plotted in Figure 1B).



1027  
 1028 **Figure 8.** Relating MAM NINO3.4 and Western V SST to ENSO and West Pacific Warming  
 1029 Mode Empirical Orthogonal Functions (EOF). **A.** 1981-2022 correlation between the 1<sup>st</sup>  
 1030 Principal Component (PC) of tropical Pacific MAM SSTS and observed MAM SSTS. Yellow  
 1031 box denotes the NINO3.4 region. **B.** Same but for the WPWM and Western V region. **C.** Time-  
 1032 series of MAM WPWM and ENSO MAM PCs, expressed as standardized anomalies centered on  
 1033 a 1981-2021 baseline. **D.** Same for regional SST averaged over the Western V and NINO3.4.  
 1034



1035 **Figure 9.** Relating Warm Pool heating and more frequent droughts to anthropogenic warming in  
 1036 the Western V. **A.** Observed and estimated 20-yr ERA5 West Pacific Heating V SST anomalies.  
 1037 The green line show regression estimates based on observed standardized 20-yr Western V and  
 1038 NINO3.4 SST. The red line shows estimates based only observed Western V. The thick black  
 1039 line shows 20-yr Warm Pool heating based on the median CMIP6 Western V SST estimates. The  
 1040 thin black lines show the spread of CMIP6 Warm Pool Heating estimates. **B.** The 20-yr observed  
 1041 frequency of EA dry seasons (i.e. circles in Figure 2C), along with Western V and NINO3.4-  
 1042 based regression estimates.  
 1043  
 1044

1045

## 1046 References

- 1047  
 1048 Adler, R. F., G. Gu, M. Sapiano, J.-J. Wang, and G. J. Huffman (2017), Global precipitation:  
 1049 Means, variations and trends during the satellite era (1979–2014), *Surveys in Geophysics*,  
 1050 38(4), 679-699.  
 1051 Bjerknes, J. (1969), Atmospheric teleconnections from the equatorial Pacific, *Monthly Weather*  
 1052 *Review*, 97(3), 163-172, doi: 10.1175/1520-0493(1969)097<0163:atftpe>2.3.co;2.  
 1053 Button, H. (2022), Famine Early Warning Systems Network forecasts alert USAID to impending  
 1054 food emergencies, edited, US Agency for International Development, Washington, DC.  
 1055 Cai, W., B. Ng, G. Wang, A. Santoso, L. Wu, and K. Yang (2022), Increased ENSO sea surface  
 1056 temperature variability under four IPCC emission scenarios, *Nature Climate Change*, 12(3),  
 1057 228-231, doi: 10.1038/s41558-022-01282-z.  
 1058 Cai, W., A. Santoso, G. Wang, S.-W. Yeh, S.-I. An, K. M. Cobb, M. Collins, E. Guilyardi, F.-F.  
 1059 Jin, and J.-S. Kug (2015a), ENSO and greenhouse warming, *Nature Climate Change*.  
 1060 Cai, W., G. Wang, A. Santoso, M. J. McPhaden, L. Wu, F.-F. Jin, A. Timmermann, M. Collins,  
 1061 G. Vecchi, and M. Lengaigne (2015b), Increased frequency of extreme La Niña events under  
 1062 greenhouse warming, *Nature Climate Change*, 5(2), 132-137.  
 1063 Checchi, F., and W. C. Robinson (2013), Mortality among populations of southern and central  
 1064 Somalia affected by severe food insecurity and famine during 2010-2012*Rep.*, 87 pp,  
 1065 [http://www.fsnao.org/downloads/Somalia\\_Mortality\\_Estimates\\_Final\\_Report\\_8May2013\\_up](http://www.fsnao.org/downloads/Somalia_Mortality_Estimates_Final_Report_8May2013_upload.pdf)  
 1066 [load.pdf](http://www.fsnao.org/downloads/Somalia_Mortality_Estimates_Final_Report_8May2013_upload.pdf), Rome, Washington.

- 1067 Dinku, T., C. Funk, P. Peterson, R. Maidment, T. Tadesse, H. Gadain, and P. Ceccato (2018),  
1068 Validation of the CHIRPS satellite rainfall estimates over eastern of Africa, *Quarterly*  
1069 *Journal of the Royal Meteorological Society*.
- 1070 Endris, H. S., C. Lennard, B. Hewitson, A. Dosio, G. Nikulin, and H.-J. Panitz (2016),  
1071 Teleconnection responses in multi-GCM driven CORDEX RCMs over Eastern Africa,  
1072 *Climate Dynamics*, 46(9), 2821-2846.
- 1073 Endris, H. S., C. Lennard, B. Hewitson, A. Dosio, G. Nikulin, and G. A. Artan (2019), Future  
1074 changes in rainfall associated with ENSO, IOD and changes in the mean state over Eastern  
1075 Africa, *Climate dynamics*, 52(3), 2029-2053.
- 1076 Endris, H. S., P. Omondi, S. Jain, C. Lennard, B. Hewitson, L. Chang'a, J. Awange, A. Dosio, P.  
1077 Ketiemi, and G. Nikulin (2013), Assessment of the performance of CORDEX regional  
1078 climate models in simulating East African rainfall, *Journal of Climate*, 26(21), 8453-8475.
- 1079 Eyring, V., S. Bony, G. A. Meehl, C. A. Senior, B. Stevens, R. J. Stouffer, and K. E. Taylor  
1080 (2016), Overview of the Coupled Model Intercomparison Project Phase 6 (CMIP6)  
1081 experimental design and organization, *Geoscientific Model Development*, 9(5), 1937-1958.
- 1082 Finney, D. L., J. H. Marsham, D. P. Walker, C. E. Birch, B. J. Woodhams, L. S. Jackson, and S.  
1083 Hardy (2020), The effect of westerlies on East African rainfall and the associated role of  
1084 tropical cyclones and the Madden–Julian Oscillation, *Quarterly Journal of the Royal*  
1085 *Meteorological Society*, 146(727), 647-664, doi: <https://doi.org/10.1002/qj.3698>.
- 1086 Funk, C., and A. Hoell (2015), The leading mode of observed and CMIP5 ENSO-residual sea  
1087 surface temperatures and associated changes in Indo-Pacific climate, *Journal of Climate*,  
1088 28(11), 4309-4329.
- 1089 Funk, C., and A. Hoell (2017), Recent Climate Extremes Associated with the West Pacific  
1090 Warming Mode, in *Climate Extremes: Patterns and Mechanisms*, edited by S. Y. Wang, Jin-  
1091 Ho; Funk, Chris; Gillies, Robert, Wiley Press, American Geophysical Union.
- 1092 Funk, C., and e. al. (2019), Recognizing the Famine Early Warning Systems Network (FEWS  
1093 NET): Over 30 Years of Drought Early Warning Science Advances and Partnerships  
1094 Promoting Global Food Security, *Bull. Amer. Meteor. Soc.* 100(6), 1010-1027.
- 1095 Funk, C., S. E. Nicholson, M. Landsfeld, D. Klotter, P. Peterson, and L. Harrison (2015a), The  
1096 Centennial Trends Greater Horn of Africa precipitation dataset, *Scientific Data*, 2(150050),  
1097 doi: 10.1038/sdata.2015.50.
- 1098 Funk, C., M. D. Dettinger, J. C. Michaelsen, J. P. Verdin, M. E. Brown, M. Barlow, and A. Hoell  
1099 (2008), Warming of the Indian Ocean threatens eastern and southern African food security  
1100 but could be mitigated by agricultural development, *Proc Nat Acad Sci USA*, 105(31),  
1101 11081-11086.
- 1102 Funk, C., A. Hoell, S. Shukla, I. Bladé, B. Liebmann, J. B. Roberts, and G. Husak (2014),  
1103 Predicting East African spring droughts using Pacific and Indian Ocean sea surface  
1104 temperature indices, *Hydrology and Earth System Sciences Discussions*, 11(3), 3111-3136.
- 1105 Funk, C., G. Senay, A. Asfaw, J. Verdin, J. Rowland, J. Michaelson, G. Eilerts, D. Korecha, and  
1106 R. Choularton (2005), Recent drought tendencies in Ethiopia and equatorial-subtropical  
1107 eastern Africa, *Vulnerability to Food Insecurity: Factor Identification and Characterization*  
1108 *Report, 1*, 12.
- 1109 Funk, C., P. Peterson, M. Landsfeld, D. Pedreros, J. Verdin, S. Shukla, G. Husak, J. Rowland, L.  
1110 Harrison, and A. Hoell (2015b), The climate hazards infrared precipitation with stations—a  
1111 new environmental record for monitoring extremes, *Scientific data*, 2.

- 1112 Funk, C., et al. (2018), Examining the role of unusually warm Indo-Pacific sea surface  
1113 temperatures in recent African droughts *Quart J Roy Meteor Soc*, 144, 360-383, doi:  
1114 10.1002/qj.3266.
- 1115 Funk, C., et al. (2019), Examining the potential contributions of extreme 'Western V' sea surface  
1116 temperatures to the 2017 March-June East African Drought, *Bull. Amer. Meteor. Soc.*,  
1117 100(1), S55-S60.
- 1118 Gelaro, R., et al. (2017), The Modern-Era Retrospective Analysis for Research and Applications,  
1119 Version 2 (MERRA-2), *Journal of Climate*, 30(14), 5419-5454, doi: 10.1175/JCLI-D-16-  
1120 0758.1.
- 1121 Gill, A. E. (1980), Some simple solutions for heat-induced tropical circulation, *Q J Roy Meteor*  
1122 *Soc*, 106, 447-462.
- 1123 Gill, A. E. (1982), *Atmosphere-ocean dynamics*, 662 pp., Academic Press, San Diego.
- 1124 Gudoshava, M., H. O. Misiani, Z. T. Segele, S. Jain, J. O. Ouma, G. Otieno, R. Anyah, V. S.  
1125 Indasi, H. S. Endris, and S. Osima (2020), Projected effects of 1.5 C and 2 C global warming  
1126 levels on the intra-seasonal rainfall characteristics over the Greater Horn of Africa, *Environ*  
1127 *Res Lett*, 15(3), 034037.
- 1128 Hersbach, H., B. Bell, P. Berrisford, S. Hirahara, A. Horányi, J. Muñoz-Sabater, J. Nicolas, C.  
1129 Peubey, R. Radu, and D. Schepers (2020), The ERA5 global reanalysis, *Quarterly Journal of*  
1130 *the Royal Meteorological Society*, 146(730), 1999-2049.
- 1131 Hoell, A., and C. Funk (2013a), Indo-Pacific sea surface temperature influences on failed  
1132 consecutive rainy seasons over eastern Africa, *Climate Dynamics*, 43(5-6), 1645-1660.
- 1133 Hoell, A., and C. Funk (2013b), The ENSO-Related West Pacific Sea Surface Temperature  
1134 Gradient, *Journal of Climate*, 26(23), 9545-9562.
- 1135 Huang, B., P. W. Thorne, V. F. Banzon, T. Boyer, G. Chepurin, J. H. Lawrimore, M. J. Menne,  
1136 T. M. Smith, R. S. Vose, and H.-M. Zhang (2017), Extended Reconstructed Sea Surface  
1137 Temperature, Version 5 (ERSSTv5): Upgrades, Validations, and Intercomparisons, *Journal*  
1138 *of Climate*, 30(20), 8179-8205, doi: 10.1175/JCLI-D-16-0836.1.
- 1139 Husak, G. J., J. Michaelsen, and C. Funk (2007), Use of the gamma distribution to represent  
1140 monthly rainfall in Africa for drought monitoring applications, *International Journal of*  
1141 *Climatology*, 27(7), 935-944.
- 1142 ICPAC, FEWS-NET, WMO, FAO, WFP, and JRC (2022a), Unprecedented drought brings threat  
1143 of starvation to millions in Ethiopia, Kenya, and Somalia, *Multi-Agency Drought Alert*.
- 1144 ICPAC, et al. (2022b), Immediate global action required to prevent Famine in the Horn of  
1145 Africa, *Multi-agency Drought Alert*.
- 1146 Johnson, N. C. (2013), How many ENSO flavors can we distinguish?, *Journal of Climate*,  
1147 26(13), 4816-4827.
- 1148 Kilavi, M., D. MacLeod, M. Ambani, J. Robbins, R. Dankers, R. Graham, H. Titley, A. A. Salih,  
1149 and M. C. Todd (2018), Extreme rainfall and flooding over central Kenya including Nairobi  
1150 city during the long-rains season 2018: causes, predictability, and potential for early warning  
1151 and actions, *Atmosphere*, 9(12), 472.
- 1152 Kirtman, B. P., D. Min, J. M. Infanti, J. L. Kinter III, D. A. Paolino, Q. Zhang, H. van den Dool,  
1153 S. Saha, M. P. Mendez, and E. Becker (2014), The North American Multimodel Ensemble:  
1154 Phase-1 seasonal-to-interannual prediction; phase-2 toward developing intraseasonal  
1155 prediction, *B Am Meteorol Soc*, 95(4), 585-601.

- 1156 L'Heureux, M. L., S. Lee, and B. Lyon (2013), Recent multidecadal strengthening of the Walker  
1157 circulation across the tropical Pacific, *Nature Climate Change*, 3(6), 571-576, doi:  
1158 doi:10.1038/nclimate1840.
- 1159 Liebmann, B., I. Bladé, G. N. Kiladis, L. M. Carvalho, G. B. Senay, D. Allured, S. Leroux, and  
1160 C. Funk (2012), Seasonality of African precipitation from 1996 to 2009, *Journal of Climate*,  
1161 25(12), 4304-4322.
- 1162 Liebmann, B., M. P. Hoerling, C. Funk, I. Bladé, R. M. Dole, D. Allured, X. Quan, P. Pegion,  
1163 and J. K. Eischeid (2014), Understanding Recent Eastern Horn of Africa Rainfall Variability  
1164 and Change, *J. Climate*, 27(23), 8630-8645.
- 1165 Lyon, B. (2014), Seasonal Drought in the Greater Horn of Africa and its Recent Increase During  
1166 the March-May Long Rains, *Journal of Climate*, 27(2014), 7953-7975.
- 1167 Lyon, B. (2020), Biases in CMIP5 Sea Surface Temperature and the Annual Cycle of East  
1168 African Rainfall, *Journal of Climate*, 33(19), 8209-8223.
- 1169 Lyon, B. (2021), Biases in sea surface temperature and the annual cycle of Greater Horn of  
1170 Africa rainfall in CMIP6, *International Journal of Climatology*.
- 1171 Lyon, B., and D. G. DeWitt (2012), A recent and abrupt decline in the East African long rains,  
1172 *GEOPHYSICAL RESEARCH LETTERS*, 39(L02702).
- 1173 Lyon, B., and N. Vigaud (2017), Unraveling East Africa's climate paradox, *Climate extremes:*  
1174 *Patterns and mechanisms*, 265, 281.
- 1175 Lyon, B., A. G. Barnston, and D. G. DeWitt (2013), Tropical pacific forcing of a 1998–1999  
1176 climate shift: observational analysis and climate model results for the boreal spring season,  
1177 *Climate Dynamics*, 43 (3-4), 893-909.
- 1178 MacLeod, D. (2018), Seasonal predictability of onset and cessation of the east African rains,  
1179 *Weather and climate extremes*, 21, 27-35.
- 1180 Mantua, N., and S. Hare (2002), The Pacific Decadal Oscillation, *Journal of Oceanography*,  
1181 58(1), 35-44, doi: 10.1023/a:1015820616384.
- 1182 Meinshausen, M., Z. R. Nicholls, J. Lewis, M. J. Gidden, E. Vogel, M. Freund, U. Beyerle, C.  
1183 Gessner, A. Nauels, and N. Bauer (2020), The shared socio-economic pathway (SSP)  
1184 greenhouse gas concentrations and their extensions to 2500, *Geoscientific Model*  
1185 *Development*, 13(8), 3571-3605.
- 1186 Nicholson, S. E. (2015), Long-term variability of the East African 'short rains' and its links to  
1187 large-scale factors, *International Journal of Climatology*, n/a-n/a, doi: 10.1002/joc.4259.
- 1188 Nicholson, S. E. (2017), Climate and Climatic Variability of Rainfall over Eastern Africa,  
1189 *Reviews of Geophysics*, n/a-n/a, doi: 10.1002/2016RG000544.
- 1190 NOAA (2022), *Cold & Warm Episodes by Season*, edited by C. P. Center.
- 1191 Ogega, O. M., J. Koske, J. B. Kung'u, E. Scoccimarro, H. S. Endris, and M. N. Mistry (2020),  
1192 Heavy precipitation events over East Africa in a changing climate: results from CORDEX  
1193 RCMs, *Climate Dynamics*, 55(3), 993-1009.
- 1194 Park, S., D. Kang, C. Yoo, J. Im, and M.-I. Lee (2020), Recent ENSO influence on East African  
1195 drought during rainy seasons through the synergistic use of satellite and reanalysis data,  
1196 *ISPRS Journal of Photogrammetry and Remote Sensing*, 162, 17-26.
- 1197 Peixoto, J. P., and A. H. Oort (1992), *Physics of Climate*, Am. Inst. Physics, New York.
- 1198 Rowell, D. P., B. B. Booth, S. E. Nicholson, and P. Good (2015), Reconciling Past and Future  
1199 Rainfall Trends over East Africa, *Journal of Climate*, 28(24), 9768-9788, doi: 10.1175/JCLI-  
1200 D-15-0140.1.

- 1201 Roxy, M. K., P. Dasgupta, M. J. McPhaden, T. Suematsu, C. Zhang, and D. Kim (2019),  
1202 Twofold expansion of the Indo-Pacific warm pool warps the MJO life cycle, *Nature*,  
1203 575(7784), 647-651, doi: 10.1038/s41586-019-1764-4.
- 1204 Rubiano, M. P. (2022), How Scientists Predict Famine Before It Hits, *BBC Future Planet*.
- 1205 Schwarzwald, K., L. Goddard, R. Seager, M. Ting, and K. Marvel (2022), Understanding CMIP6  
1206 Biases in the Representation of the Greater Horn of Africa Long and Short Rains.
- 1207 Seager, R., N. Henderson, and M. Cane (2022), Persistent discrepancies between observed and  
1208 modeled trends in the tropical Pacific Ocean, *Journal of Climate*, 1-41, doi: 10.1175/jcli-d-  
1209 21-0648.1.
- 1210 Seager, R., M. Cane, N. Henderson, D.-E. Lee, R. Abernathey, and H. Zhang (2019),  
1211 Strengthening tropical Pacific zonal sea surface temperature gradient consistent with rising  
1212 greenhouse gases, *Nature Climate Change*, 9(7), 517-522, doi: 10.1038/s41558-019-0505-x.
- 1213 Shukla, S., J. Roberts, A. Hoell, C. C. Funk, F. Robertson, and B. Kirtman (2016), Assessing  
1214 North American multimodel ensemble (NMME) seasonal forecast skill to assist in the early  
1215 warning of anomalous hydrometeorological events over East Africa, *Climate Dynamics*, 1-  
1216 17, doi: 10.1007/s00382-016-3296-z.
- 1217 Shukla, S., G. Husak, W. Turner, F. Davenport, C. Funk, L. Harrison, and N. Krell (2021), A  
1218 slow rainy season onset is a reliable harbinger of drought in most food insecure regions in  
1219 Sub-Saharan Africa, *Plos one*, 16(1), e0242883.
- 1220 Tierney, J., J. Smerdon, K. Anchukaitis, and R. Seager (2013), Multidecadal variability in East  
1221 African hydroclimate controlled by the Indian Ocean, *Nature*, 493(7342), 389-392.
- 1222 Tierney, J. E., C. C. Ummenhofer, and P. B. deMenocal (2015), Past and future rainfall in the  
1223 Horn of Africa, *Science Advances*, 1(9), 1-8, doi: 10.1126/sciadv.1500682.
- 1224 Trenberth, K. E., and D. P. Stepaniak (2003a), Covariability of components of poleward  
1225 atmospheric energy transports on seasonal and interannual timescales, *Journal of Climate*,  
1226 16(22), 3691-3705.
- 1227 Trenberth, K. E., and D. P. Stepaniak (2003b), Seamless poleward atmospheric energy transports  
1228 and implications for the Hadley circulation, *Journal of Climate*, 16(22), 3706-3722.
- 1229 Verdin, J., C. Funk, G. Senay, and R. Choullarton (2005), Climate science and famine early  
1230 warning, *Philos T Roy Soc B*, 360(1463), 2155-2168.
- 1231 Voosen, P. (2020), The hunger forecast, *Science*, 368(6488), 226-229, doi: DOI:  
1232 10.1126/science.368.6488.226.
- 1233 Wainwright, C. M., J. H. Marsham, R. J. Keane, D. P. Rowell, D. L. Finney, E. Black, and R. P.  
1234 Allan (2019), 'Eastern African Paradox' rainfall decline due to shorter not less intense Long  
1235 Rains, *npj Climate and Atmospheric Science*, 2(1), 1-9.
- 1236 Walker, D. P., J. H. Marsham, C. E. Birch, A. A. Scaife, and D. L. Finney (2020), Common  
1237 Mechanism for Interannual and Decadal Variability in the East African Long Rains,  
1238 *Geophysical Research Letters*, 47(22), e2020GL089182, doi:  
1239 <https://doi.org/10.1029/2020GL089182>.
- 1240 Williams, P., and C. Funk (2011), A westward extension of the warm pool leads to a westward  
1241 extension of the Walker circulation, drying eastern Africa, *Climate Dynamics*, 37(11-12),  
1242 2417-2435.
- 1243 Wills, R. C. J., Y. Dong, C. Proistosescu, K. C. Armour, and D. S. Battisti (2022), Systematic  
1244 Climate Model Biases in the Large-Scale Patterns of Recent Sea-Surface Temperature and  
1245 Sea-Level Pressure Change, *Geophysical Research Letters*, 49(17), e2022GL100011, doi:  
1246 <https://doi.org/10.1029/2022GL100011>.

1247 Yang, W., R. Seager, M. A. Cane, and B. Lyon (2014), The East African Long Rains in  
1248 Observations and Models, *Journal of Climate*, 27(19), 7185-7202, doi: 10.1175/JCLI-D-13-  
1249 00447.1.  
1250

1 **Frequent but Predictable Droughts in East Africa Driven By A Walker Circulation**  
2 **Intensification**

3  
4 **Chris Funk<sup>1</sup>, Andreas H. Fink<sup>2</sup>, Laura Harrison<sup>1</sup>, Zewdu Segele<sup>3</sup>, Hussen S. Endris<sup>3</sup>,**  
5 **Gideon Galu<sup>1</sup>, Sharon Nicholson<sup>4</sup>, Diriba Korecha<sup>1</sup>**

6  
7 <sup>1</sup>Climate Hazards Center, University of California, Santa Barbara

8  
9 <sup>2</sup> Institute of Meteorology and Climate Research, Karlsruhe Institute of Technology, Karlsruhe,  
10 Germany

11  
12 <sup>3</sup>IGAD Climate Prediction and Applications Center, Kenya

13  
14 <sup>4</sup>Meteorology and Environmental Science, Florida State University

15  
16 Corresponding Author: Chris Funk

17 **Email:** [chrisfunk@ucsb.edu](mailto:chrisfunk@ucsb.edu)

18 **Key Points:**

- 19 • Human-induced warming in the western V area of the Pacific combined with La Niña,  
20 has produced frequent, predictable March-April-May droughts.
- 21 • Thermodynamic analyses link these droughts to a stronger Walker Ciruclation, driven by  
22 predictable warming in the Western V region.
- 23 • CMIP6 simulations indicate that western V warming is largely human-induced, this  
24 warming has enhanced and will enhance the Walker Circulation.  
25  
26

## 27 **Abstract**

28 The decline of the eastern East African (EA) March-April-May (MAM) rains poses a life-  
29 threatening ‘enigma’, an enigma linked to sequential droughts in the most food insecure region  
30 in the world. The MAM 2022 drought was the driest on record, preceded by three poor rainy  
31 seasons, and followed by widespread starvation. Connecting these droughts is an interaction  
32 between La Niña and climate change, an interaction that provides exciting opportunities for long  
33 lead prediction and proactive disaster risk management. Using observations, reanalyses, and  
34 climate change simulations, we show here, for the first time, that post-1997 OND La Niña events  
35 are robust precursors of: (1) strong MAM ‘Western V Gradients’ in the Pacific, which help  
36 produce (2) large increases in moisture convergence and atmospheric heating near Indonesia,  
37 which appear associated with (3) regional shifts in moisture transports and vertical velocities,  
38 which (4) help explain more frequent dry EA rainy seasons. Understanding this causal chain will  
39 help make long-lead forecasts more actionable. Increased Warm Pool atmospheric heating and  
40 moisture convergence sets the stage for dangerous sequential droughts in EA. At 20-yr time  
41 scales, we show that these Warm Pool heating increases are attributable to observed Western V  
42 warming, which is in turn largely attributable to climate change. As energy builds up in the  
43 oceans and atmosphere, we see stronger convergence patterns, which offer opportunities for  
44 prediction. Hence, linking EA drying to a stronger Walker Circulation can help explain the  
45 ‘enigma’ while underscoring the predictable risks associated with recent La Niña events.

46

## 47 **Plain Language Summary**

48 In 2022, an unprecedented sequence of five sequential droughts, exacerbated by high global  
49 food and fuel prices, drove an exceptional food security crisis in Ethiopia, Somalia and Kenya,  
50 pushing more than 20 million people into a food security crisis. Potential famine loomed in some  
51 areas. Beginning in late 2020, this was the longest and most severe drought recorded in the Horn  
52 in at least 70 years, resulting in multiple failed harvests and large-scale livestock deaths that  
53 decimated food and income sources for rural communities, placed increasing pressure on the cost  
54 of food among urban communities, and led to rising levels of destitution and displacement.  
55 These droughts occur against the backdrop of the ‘East Africa Climate Paradox’, which centers  
56 on the discrepancy between climate change model projections of increased East African March-  
57 April-May rains, and many observational studies pointing towards declines. Here, we show how  
58 framing this dilemma as an ‘enigma’ opens the door to explaining and predicting sequential East  
59 African droughts. The enigma we explore is ‘why are so many recent La Niña events associated  
60 with dry March-April-May rains?’ La Niña events tend to reach their maximum intensity in the  
61 boreal fall, often producing East African droughts. Before the western Pacific ocean warmed  
62 dramatically in 1998, the link between La Niña events and dry March-April-May rains was  
63 weak. Since 1998, the link is very strong. This sets the stage for dangerous sequential droughts,  
64 such as in 2010/11, 2016/17, 2020/21, 2021/2022, and perhaps 2022/23. We explain this enigma  
65 using observations, reanalyses, and the latest (Phase 6) climate change simulations.

66 While climate change models do recreate the observed East African drying, they do recreate  
67 very well the observed west Pacific warming. Climate change, not natural decadal variability  
68 associated with the Pacific Decadal Oscillation, has increased west Pacific sea surface  
69 temperatures. This, in turn, is increasing the ‘Western V Gradient’, a measure of the east-west  
70 differences in Pacific ocean temperatures. When this gradient is negative, there are frequent East

71 African droughts, and this happens in a very predictable way during or after recent La Niña  
72 events. This allows us to predict many dry rainy seasons ~eight months in advance. Such  
73 predictive capacity is important, because the frequency of strong Pacific temperature gradients is  
74 increasing, and we shown that climate change simulations recreate this tendency, and expect it to  
75 increase over the coming decades.

76 What connects East African droughts to Pacific temperature gradients? We answer this  
77 question by examining observed atmospheric heating, moisture transports, and moisture  
78 convergence patterns. In general, eastern East Africa is dry because it resides along the western  
79 edge of the Indian Ocean branch of the Indo-Pacific 'Walker Circulation'. Across East Africa  
80 and the western Indian Ocean, and over the central and eastern Pacific, rainfall and moisture  
81 levels are low. In the area around Indonesia (the eastern Indian and western Pacific Oceans),  
82 winds drive moisture convergence and heavy rains. Here, building on many years of research by  
83 scientists working for the Famine Early Warning Systems Network, we show for the first time  
84 that the strength of the Walker Circulation can be quantified using atmospheric heating and  
85 moisture convergence. When heating and moisture convergence is high in the area around  
86 Indonesia, East African rains are almost always dry. Since 1998, when there has been a La Niña  
87 in October-November-December, there has almost always been strong March-April-May heating  
88 and moisture convergence around Indonesia. This resolves the enigma. Climate change-enhanced  
89 La Niñas amplify the Pacific trade winds, producing strong March-April-May sea surface  
90 temperature gradients, which amplify the Walker Circulation, which reduce moisture  
91 convergence and ascending atmospheric motions over the eastern Horn of Africa.

92 We conclude with a look toward the future evolution of the Walker Circulation, by relating  
93 the observed strength of the Walker Circulation to 20-yr averages of western and eastern Pacific  
94 sea surface temperatures. Both play a significant role, and together explain 96% of the observed  
95 variability. The observed Walker Circulation intensification is primarily driven by the west  
96 Pacific, which in turn is strongly related to climate change. CMIP6 projections of Pacific sea  
97 surface temperatures, combined with the observed empirical relationships, imply further strong  
98 increases in Walker Circulation intensities. Hence, further rainfall declines appear likely,  
99 especially before or after La Niña events. But the process-based analyses presented here suggests  
100 that many of the dry seasons may be predictable, based on Pacific sea surface temperature  
101 gradients.

102

103

104

## 105 **1 Introduction – CMIP6 simulations can enhance drought early warning to support food** 106 **security**

107 This study examines the drivers of March-April-May rains in eastern East Africa (EA), a region  
108 of extreme food insecurity and frequent droughts [Shukla *et al.*, 2021]. Located near the equator  
109 and the descending branch of the Indian Ocean branch of east-west Walker Circulation, this  
110 region receives rains in OND and MAM [Brant Liebmann *et al.*, 2012; Nicholson, 2017].  
111 Sequential OND/MAM droughts can have profound food security impacts, as in 2010/2011,  
112 when more 250,000 Somalis perished due to famine [Checchi and Robinson, 2013]. In 2020-2022  
113 an unprecedented sequence of five dry seasons, associated with a three-year La Niña event, led  
114 to a massive humanitarian crisis, potential famine, and widespread loss of livestock and  
115 livelihoods [ICPAC *et al.*, 2022a; ICPAC *et al.*, 2022b]. These crises occur amidst a continuing  
116 and well-documented decline in MAM ‘long’ rains, as first identified by the Famine Early  
117 Warning Systems Network (FEWS NET) [Funk *et al.*, 2005; Verdin *et al.*, 2005], and later  
118 studies [Lyon, 2014; Lyon and DeWitt, 2012; Yang *et al.*, 2014]. Following the 1997/98 El Niño,  
119 dry MAM seasons became more frequent [Lyon, 2014], while the variability of OND rains  
120 increased [Nicholson, 2015]. The MAM season is also becoming ‘shorter not less intense’ due to  
121 regional circulation changes [Wainwright *et al.*, 2019].  
122

123 Our focus here is the potential link between climate change and the dramatic post-1998 increase  
124 in the frequency of dry MAM seasons, following OND La Niñas. This increase sets the stage for  
125 dangerous OND/MAM multi-season droughts [Funk *et al.*, 2018], but also opens opportunities  
126 for predicting the MAM rains, as in 2017 [Voosen, 2020] and 2021 and 2022 [Rubiano, 2022].  
127 As noted in a 2022 multi-agency alert [ICPAC *et al.*, 2022a], between 1950 and 1997, OND La  
128 Niña conditions, as defined by the Climate Prediction Center [NOAA, 2022], did not alter the  
129 odds of a below-normal (bottom tercile) EA MAM rainy season. Following the twelve La Niñas  
130 since OND 1998, nine rainy seasons have been poor. This shift, and OND La Niña conditions in  
131 2020, 2021, and 2022 has contributed to repetitive droughts and potential famine conditions in  
132 2023 [ICPAC *et al.*, 2022b]. Here, in contrast with other valuable studies that focused on larger  
133 domains, regional climate processes, or sub-seasonal drivers [Finney *et al.*, 2020; Nicholson,  
134 2017; Wainwright *et al.*, 2019], we focus here on large-scale teleconnections that may help  
135 identify, explain and predict recent below-normal EA MAM rainy seasons. These results help  
136 explain regional circulation changes consistent with a ‘shorter not less intense’ rainy season  
137 [Wainwright *et al.*, 2019] and the increasing links to the El Niño Southern Oscillation (ENSO)  
138 [Park *et al.*, 2020]. Our goal in this paper is to support early warning and forecasting efforts by  
139 explaining the links between La Niña, predictable Pacific SST gradients and EA dry seasons, on  
140 both interannual and decadal time-scales.  
141

142 Our study proceeds in three stages. We first examine CMIP6 and observed EA MAM  
143 precipitation and Pacific sea surface temperatures (SST). This links EA drying to human-induced  
144 warming in the west Pacific. Then, using reanalyses, we show that strong Pacific SST gradients  
145 and Walker Circulation disruptions follow post-1997 La Niñas. Seasons with more intense with  
146 Walker Circulations are clearly linked to a preponderance of dry EA MAM seasons. We then use  
147 observed Pacific SST gradients and CMIP6 SST projections to suggest that human-induced west

148 Pacific warming has, and will, enhance the Walker Circulation in ways associated with drying  
149 over EA.

150

151

## 152 **1.1 Background – Describing the ‘East Africa Enigma’**

153

154 Following its introduction in 2015 [Rowell *et al.*, 2015], several papers have discussed the ‘East  
155 African Climate Paradox’ [Lyon and Vigaud, 2017; Wainwright *et al.*, 2019] – while  
156 observations clearly indicate more frequent dry seasons along with later starts and early cessation  
157 [Wainwright *et al.*, 2019], climate change simulations have indicated rainfall increases. While  
158 natural Pacific Decadal Variability (PDV) [Lyon, 2014; Lyon and Vigaud, 2017; Yang *et al.*,  
159 2014] might explain this change, it is becoming more and more likely that the ‘paradox’ arises  
160 due to the models’ systematic biases in SSTs and African circulation features [Lyon, 2020; 2021;  
161 Schwarzwald *et al.*, 2022; Shukla *et al.*, 2016; J E Tierney *et al.*, 2015]. The terrain and  
162 teleconnections controlling precipitation in EA are complex and poorly resolved by global  
163 climate models [Endris *et al.*, 2016]. The models tend to misrepresent the mean zonal SST  
164 gradients in the Indian Ocean [Lyon, 2021; Lyon and Vigaud, 2017; Schwarzwald *et al.*, 2022]  
165 and Pacific Ocean [Seager *et al.*, 2022; Seager *et al.*, 2019]. Over EA they tend to have a  
166 seasonal cycle that is far too wet in OND and dry in MAM [J Tierney *et al.*, 2013]. Multi-model  
167 ensembles of regional climate model simulations perform much better [Endris *et al.*, 2013], and  
168 indicate decreased rainfall in MAM [Ogega *et al.*, 2020]. Recent evaluations of regional and  
169 global climate change models [Endris *et al.*, 2019] indicate stronger future ENSO  
170 teleconnections during MAM, consistent with several climate change studies indicating an  
171 increased frequency of strong-gradient La Niñas [Cai *et al.*, 2022; Cai *et al.*, 2015b].

172 In place of the ‘paradox’, we focus here on the ‘East African Climate Enigma’. The ‘enigma’  
173 relates the increased frequency of dry MAM seasons, following OND La Niñas, to predictable  
174 ‘Western V’ SST gradients (described below) in MAM. The Western V region begins in  
175 equatorial West Pacific (near Indonesia), and extends poleward into the extra-tropical northern  
176 and southern Pacific. Warm SSTs in this region have been linked to dry EEA MAM rainy  
177 seasons [Funk *et al.*, 2018; Funk *et al.*, 2019] and the West Pacific Warming Mode [Funk and  
178 Hoell, 2015]. From a food security perspective, the link between OND La Niñas and MAM  
179 rainfall deficits is important, because it sets the stage for dangerous sequential droughts. Long  
180 lead MAM rainfall forecasts have helped guide humanitarian responses in 2017 [Voosen, 2020],  
181 and 2021/2022 [Button, 2022]. But while they are effective, there has not been relatively little  
182 research focused on how strong Pacific SST gradients induce dry EA rainy seasons, why such  
183 conditions tend to be associated with La Niña events, and how human-induced warming might  
184 be influencing outcomes.

## 185 **2 Methods**

186 The focus here will be on explaining the link between recent (post-1997) OND La Niñas,  
187 as defined by OND [Funk *et al.*, 2018; Funk *et al.*, 2019] NOAA Oceanic Niño Index, ONI  
188 values [NOAA, 2022] and frequent MAM dry seasons in the following year. This also relates to  
189 recent work documenting increasing ENSO-East Africa teleconnections [Park *et al.*, 2020].  
190 While forecasting is not the focus here, these explorations provide process-based insights that  
191 can inform operational forecasts, such as those provided by the IGAD Climate Prediction and

192 Applications Center (ICPAC, [www.icpac.net](http://www.icpac.net)) or the Climate Hazards Center (CHC,  
 193 [blog.chc.ucsb.edu](http://blog.chc.ucsb.edu)). Our goals are to better understand links between the WVG and La Niñas, the  
 194 WVG and the Walker Circulation, and the WVG and climate change. This work has implications  
 195 for seasonal climate prediction, humanitarian assistance programming, and climate change  
 196 adaptation. Our study progresses in three stages.

## 197 **2.1 Linking droughts to predictable Pacific SST gradients and human-induced warming in** 198 **the west Pacific**

199 We begin by describing the ‘East African Climate Paradox’ [Rowell *et al.*, 2015] using updated  
 200 (through 2022) rainfall and SST observations and CMIP6 precipitation simulations. Composites  
 201 of SSTs for dry and wet seasons are evaluated. Dry events, but not wet events, are associated  
 202 with coherent SST teleconnections. Dry MAM seasons are characterized by very warm west  
 203 Pacific ‘Western V’ SSTs. The western V originates in the Warm Pool area around Indonesia  
 204 and extends northeast and southeast into the extra-tropics. Warm Western V conditions have  
 205 been linked to recent MAM droughts [Funk *et al.*, 2018; Funk *et al.*, 2019]. Warming in this  
 206 region also loads heavily on the ‘West Pacific Warming Mode’, the first empirical orthogonal  
 207 function of global ENSO-residual SST [Funk and Hoell, 2015]. We define the ‘Western V  
 208 Gradient’ (WVG) as the difference between standardized NINO3.4 and Western V SSTs. Since  
 209 the west Pacific warmed following the 1997/1998 El Niño [Lyon *et al.*, 2013] and the Walker  
 210 Circulation intensified [L’Heureux *et al.*, 2013], OND La Niña events [NOAA, 2022] are always  
 211 followed by strong negative WVG values in MAM. We show that these WVG values are very  
 212 predictable. We also show that these predictions do a good job of identifying many dry MAM  
 213 seasons at long leads. Using observations, we show that since 1999, strong negative MAM WVG  
 214 events always follow La Niña events in the previous OND, when the La Niña signal tends to be  
 215 at its peak. Then, using CMIP6 simulations, we examine the level of correspondence between the  
 216 simulated SST warming trends, and observed outcomes in the NINO3.4 and Western V regions,  
 217 as well as the WVG.

## 218 **2.2 Linking La Niña/WVG events to Walker Circulation Intensification**

219 This section examines interannual WVG influences on MAM Indo-Pacific atmospheric heating,  
 220 moisture transports, and moisture convergence fields. Long term means and WVG anomalies in  
 221 atmospheric heating and moisture transports can be used to explore the Indian and Pacific  
 222 branches of the Walker Circulation [Bjerknes, 1969]. Note that we use the term ‘Walker  
 223 Circulation’ to broadly refer to the complex Indo-Pacific circulation patterns linking the Pacific  
 224 to the Warm Pool region near Indonesia, and the Warm Pool region to MAM EA rains. While we  
 225 present equatorial longitude-by-height results, we also examine spatial maps which emphasize  
 226 that emphasize how extra-tropical SST and atmospheric heating gradients act to modulate  
 227 moisture transports.

228  
 229 Our thermodynamic approach was inspired by studies using vertically integrated transports of  
 230 heat energy (internal energy,  $T$ ) and geopotential height energy (potential energy,  $Z$ ) [Peixoto  
 231 and Oort, 1992; Trenberth and Stepaniak, 2003a; b].  $T$  is a function of the vertical temperature  
 232 distribution and specific heat capacity of air,  $Z$  is a function of geopotential height and  $g$ , the  
 233 acceleration due to gravity. These are the two largest atmospheric energy terms. In atmospheric

234 thermodynamics, it is common to combine these two terms to describe changes in Dry Static  
235 Energy (DSE):

$$236 \quad \quad \quad \text{DSE} = T + Z \quad \quad \quad \text{eq. 1}$$

238  
239 DSE is a conserved quantity. Changes in DSE, however, arise from the introduction of external  
240 heating, commonly referred to as diabatic heating. Latent heating (LH) due to precipitation,  
241 radiation (R), and sensible heating (SH) in the planetary boundary layer are the largest sources of  
242 diabatic heating. The R term here is a measure of the net radiation into a column of air, i.e. a  
243 combination of the downward and upward shortwave radiation from the top of the atmosphere  
244 and surface of the Earth. Increased atmospheric water vapor contributes to increased trapped  
245 longwave radiation and increased precipitation. As the atmosphere warms and saturation vapor  
246 pressures increase, these heating terms are likely to increase as well. DSE is a conserved  
247 quantity, modulated by external (diabatic) heating, which leads to:

$$248 \quad \quad \quad \text{diabatic heating} = \text{Div}(T) + \text{Div}(Z) \quad \quad \quad \text{eq. 2}$$

249  
250  
251 Where  $\text{Div}(T)$  and  $\text{Div}(Z)$  are vertically-integrated divergence terms, based on vertically  
252 integrated temperature and geopotential height fluxes. While accurate, the standard DSE  
253 formulation of these terms obscures the fact that  $\text{Div}(T)$  and  $\text{Div}(Z)$  are strongly anti-correlated,  
254 due to hydrostatic relationships [*Peixoto and Oort, 1992*]. Converging heat in the lower and  
255 middle troposphere causes a column of air to stretch, raising upper-level heights, and increasing  
256  $\text{Div}(Z)$ . In rainy areas of the Walker Circulation, heat converges in the lower troposphere, and  
257 geopotential height energy diverges aloft. Persistent heating in the Indo-Pacific Warm Pool area  
258 produces equatorially-trapped Rossby and Kelvin waves, which (respectively) help establish the  
259 Indian and Pacific branches of the Walker Circulation [*Gill, 1980; 1982*]. To measure the  
260 strength of this forcing, we combine diabatic heating and heat convergence into a single  
261 ‘atmospheric heating’ term, measured in  $\text{Wm}^{-2}$ .

$$262 \quad \quad \quad \text{atmospheric heating} = \text{Con}(T) + \text{diabatic forcing} \quad \quad \quad \text{eq. 3}$$

263  
264  
265 As we will show, this framework provides a useful description of the humid and dry regions of  
266 the Walker Circulation. Areas with low level convergent winds will have both heat convergence  
267  $\text{Con}(T)$  and moisture convergence  $\text{Con}(Q)$ . Direct heating by heat convergence will be  
268 augmented by latent heat released via precipitation, since moisture is also conserved:

$$269 \quad \quad \quad \text{precipitation} = \text{Con}(Q) - \text{evaporation} \quad \quad \quad \text{eq. 4}$$

270  
271  
272 Since evaporation in Warm Pool areas tends to be low,  $\text{precipitation} \approx \text{Con}(Q)$ . More moisture  
273 will also increase the trapping of longwave radiation. Eq. 3, therefore, stacks covarying heating  
274 terms. From first principles, a warming atmosphere might experience increased heat  
275 convergence, simply due to increases in air temperatures, as well as increases in precipitation and  
276 decreases in outgoing longwave radiation, due to increased atmospheric water vapor. This logic  
277 also supports combining these heating terms. We examine these variables to formally evaluate  
278 whether a Walker Circulation enhancement is linked to dry EA rainy seasons. Contrasting these  
279 fields, in MAM seasons following 1998-2021 OND La Niñas and 1950-1997 La Niñas helps

280 explain links between distant WVG SST patterns and local reductions in EA MAM total  
281 precipitable water, vertical ascent, and precipitation. Changes in the Indian Ocean branch of the  
282 Walker Circulation alter moisture transports and intensify subsidence over the eastern Horn of  
283 Africa.

### 284 **2.3 Linking Western V warming to Walker Circulation intensification and more frequent** 285 **dry EA rainy seasons**

286  
287 Our final analysis focuses on decadal changes in the strength of the Walker Circulation and the  
288 frequency of below-normal MAM rainy seasons. We begin by updating the observational West  
289 Pacific Warming Mode (WPWM) analysis from Funk and Hoell (2015). This Empirical  
290 Orthogonal Function analysis underscores the points that 1) NINO3.4 and Western V and  
291 NINO3.4 SSTs closely track the first two modes of global SST, and 2) the climate-change-  
292 related WPWM, along with Western V SSTs, continues to increase rapidly. We then use  
293 regression to link 20-yr average Western V and NINO3.4 SST to 20-yr averages of Warm Pool  
294 atmospheric heating. We show that these SST values explain very well 20-yr changes in Warm  
295 Pool atmospheric heating and that the Western V warming has played an important role in the  
296 recent Walker Circulation intensification and the increased frequency of dry East African rainy  
297 seasons. CMIP6 SST ensembles are used to estimate increases in Warm Pool heating through  
298 2050.

## 299 **3 Data**

300 Dry and wet seasons are defined using satellite-gauge [Funk *et al.*, 2015b] and interpolated  
301 gauge [Funk *et al.*, 2015a] datasets. These widely used data sets were specifically developed to  
302 work well in East Africa, work well [Dinku *et al.*, 2018], and incorporate many additional  
303 raingauge observations provided by collaborators at Florida State University [Nicholson, 2017],  
304 the Ethiopian Meteorological Agency (~120 stations), and the Somali Food Security and  
305 Nutrition Analysis Unit (~90 stations). The EA area of focus is based on the region used in a  
306 mid-2022 multi-agency alert focused on the failure of the MAM 2022 rains [ICPAC *et al.*,  
307 2022a]. Areal averages of the 1981-2022 Climate Hazards InfraRed Precipitation with Stations  
308 (CHIRPS) [Funk *et al.*, 2015a] and the 1900-2014 Centennial Trends [Funk *et al.*, 2015b]  
309 correlate very well over their period of overlap (1981-2014). A bivariate regression is used to  
310 transform Centennial Trends values into CHIRPS-compatible regional averages over the 1950-  
311 1980 period. A Gamma distribution fit is then used to develop a Standardized Precipitation Index  
312 (SPI) times-series [Husak *et al.*, 2007]. This time series, and all other analyses in this study, are  
313 centered on a 1981-2021 baseline. Dry and wet seasons will be based on the EA SPI values  
314 below and above -0.44Z and +0.44Z, which corresponds with a 1-in-3 year low or high value.  
315 Dry seasons may occasionally be described as droughts, to avoid repetition. Version 5 of the  
316 NOAA Extended SST [Huang *et al.*, 2017] is used to represent ocean temperatures. To explore  
317 circulation changes we use ERA5 [Hersbach *et al.*, 2020] and MERRA2 [Gelaro *et al.*, 2017]  
318 reanalyses. Our analysis looks at moisture transports and the combined influence of local  
319 diabatic heating and atmospheric heat convergence. We also include in our study August

320 forecasts of MAM SSTs from the North American Multi-Model Ensemble (NMME)[*Kirtman et*  
321 *al.*, 2014].

322

323 Our study also uses a multi-model ensemble of 152 Shared Socio-Economic Pathway 245 SST  
324 simulations from the latest CMIP version 6 (CMIP6) archive [*Eyring et al.*, 2016] (Table 1). The  
325 moderate SSP245 scenario is based on projections of large increases in sustainable development  
326 and  $4.5 \text{ Wm}^{-2}$  of radiative forcing [*Meinshausen et al.*, 2020]. CMIP6 data were accessed from  
327 Lawrence Livermore National Laboratory (LLNL) node of the Earth System Grid Federation  
328 (ESGF) platform (<https://esgf-node.llnl.gov/search/cmip6/>).

329

330 Finally, it should be noted that most of our observational results focus on the 1981-2022 time  
331 period, during which satellite data informs our precipitation estimates and reanalyses. While we  
332 do present longer time-series of EA rainfall, and changes in 1950-2022 ERA5 WVG events, the  
333 bulk of our analysis focuses on the past 42 years. This allows for cross-checks between the  
334 ERA5 and MERRA2 reanalyses.

## 335 4 Results

### 336 4.1 Links between OND La Niña, predictable strong Western V Gradients and EA 337 Droughts

338

339 In MAM 2022, rains in Ethiopia, Kenya and Somalia were exceptionally poor (Fig. 1A,B). Here,  
340 as in several previous FEWS NET [*Funk and al.*, 2019] studies [*Funk et al.*, 2014; *Funk et al.*,  
341 2018; *Funk et al.*, 2019; *B. Liebmann et al.*, 2014], we focus on a specific spatial subset of the  
342 Greater Horn of Africa, eastern East Africa (purple polygon shown in Fig. 1A), not a broader  
343 region as in [*Finney et al.*, 2020; *Walker et al.*, 2020], because this extremely food insecure  
344 region [*Shukla et al.*, 2021] experiences frequent sequential droughts, especially during or  
345 following recent La Niña events [*Funk et al.*, 2014; *Funk et al.*, 2018; *Funk et al.*, 2019; *Hoell*  
346 *and Funk*, 2013a; b; *B. Liebmann et al.*, 2014; *Williams and Funk*, 2011]. Since 1999, 11 seasons  
347 have been dry. Many of these dry seasons have also followed 12 post-1997 OND La Niñas  
348 (yellow circles, Fig. 1B). We refer to these events as ‘Western V Gradient’ events (described  
349 further below), because even if La Niña conditions fade, strong Pacific gradients, augmented by  
350 west Pacific warming, may be conducive to dry EA MAM outcomes [*Funk et al.*, 2018; *Funk et*  
351 *al.*, 2019].

352

353 The observed drying contrasts with results (Fig. 1C,D) from 152 CMIP6 SSP245 simulations  
354 (Table 1). Time-series of 30-yr average SPI indicate little change. The last observed and  
355 simulated values from this time-series (1993-2022 average SPI) are expanded in Fig. 1D, which  
356 breaks the results out by model. The observed 30-yr SPI value is very unlikely given the  
357 observed range of CMIP6 averages. This could be explained by a large natural internal decadal  
358 variation, potentially related to the Pacific (further discussed below), or it might relate to issues  
359 associated with poor representations of mean Indo-Pacific SSTs and EA seasonality and  
360 teleconnections (discussed above in section 1.1).

361

362 Composites of standardized MAM SSTs during 1981-2022 dry seasons (Fig. 2A) exhibit a  
363 contrast between a warm ‘Western V’ region in the west Pacific and cool central-east Pacific  
364 SSTs. Western V SST are averaged over the equatorial west Pacific (120-160°E, 15°S-20°N),

365 Western North Pacific (160°E-150°W, 20°N-35°N) and Western South Pacific (155°E-150°W,  
366 15°S-30°S). Western V [Funk et al., 2019] and Western North Pacific SST [Funk et al., 2018]  
367 have been linked to dry EA rains, and FEWS NET uses a standardized gradient between  
368 NINO3.4 and Western V SSTs (the Western V Gradient, WVG) to inform operational long-lead  
369 predictions. Interestingly, while dry MAM season composites exhibit significant links to the  
370 Pacific (Fig. 2A), and some relation to Indian Ocean SSTs, wet season composites indicate less  
371 strong links (Fig. 2B). Non-linearities have been previously identified for the OND season  
372 [Nicholson, 2015], but have received little attention in MAM. Dry events may be more  
373 predictable than wet events.

374  
375 Enigmatically, strong negative MAM WVG conditions are very common following recent OND  
376 La Niñas, and are also associated with many of the recent dry EA MAM seasons (Fig. 2C). There  
377 have been 12 OND La Niñas since 1998, and the MAM WVG values the following year ranged  
378 from -0.8Z to -2.2Z. Nine of these MAM seasons were dry EA years. Here, we will describe the  
379 12 post-1997 MAM seasons that follow the last 12 La Niñas as ‘WVG events’. It is important to  
380 differentiate these from La Niñas, because warm Western V SSTs can linger after a La Niña  
381 fades (as in 2016/17) producing La Niña-like impacts in MAM, consistent with stronger ENSO  
382 teleconnections [Park et al., 2020]. Strong warming trends in the western Pacific [Funk et al.,  
383 2018; Funk et al., 2019] and frequent La Niñas since the late 1990s have led to a marked  
384 increase in the frequency of strong negative WVG conditions during MAM (Fig. 2C).

385  
386 We can predict WVG conditions at long leads, allowing us to predict many of the events that  
387 produce the decline in EA rains. As an example, Fig. 2D shows forecasts of MAM WVG values,  
388 based on September North American Multi-Model Ensemble climate forecasts<sup>1</sup> [Kirtman et al.,  
389 2014]. Western V, WVG and NINO3.4 SSTs are all predicted very well by the NMME (1982-  
390 2022 R<sup>2</sup> 0.77, 0.77, 0.67). When WVG values are predicted to be negative (< -0.5Z) we see a  
391 preponderance of dry EA MAM rainy seasons, and many of the seasons with low WVG values  
392 follow OND La Niñas. The societal import of Fig. 2D is very important, because this approach  
393 can help anticipate dangerous OND/MAM sequential droughts, which in 2020-2022 brought four  
394 sequential dry seasons and the threat of starvation to millions in Ethiopia, Kenya, and Somalia  
395 [JCPAC et al., 2022a].

396  
397 Figure 3 presents observed and simulated changes in 20-yr MAM Western V, NINO3.4 and  
398 WVG time-series. For the Western V, the observations track very closely with the CMIP6  
399 simulations (Fig. 3A). The correlation between the CMIP6 median Western V values and the  
400 observed Western V time-series is 0.96. The CMIP6 simulations suggest that climate change, not  
401 natural Pacific Decadal variability, has resulted in large SST increases in the western V region.  
402 The pace of observed warming has increased dramatically over the past 20 years. The observed  
403 2003-2022 Western V average falls comfortably within the CMIP6 distribution (Fig. 3B). This  
404 contrasts with NINO3.4 outcomes (Fig. 3C-D). As noted by other studies, in observations, there  
405 is marked lack of warming in the eastern Pacific [Seager et al., 2022; Seager et al., 2019]. The  
406 CMIP6 ensemble, on the other hand, predicts substantial warming. The distribution of  
407 standardized 2003-2022 CMIP6 NINO3.4 values (Fig. 3D) suggests that the observed lack of  
408 cooling is very unlikely, given the simulations. This might arise due to an extreme expression of

---

<sup>1</sup> <https://www.agrilinks.org/post/forecast-update-east-africa-likely-experience-six-droughts-row>

409 natural decadal variability. However, it seems increasingly likely that systematic biases in Pacific  
410 SST may also contribute to this discrepancy [Seager *et al.*, 2022; Seager *et al.*, 2019].

411  
412 As one would expect, WVG observations and CMIP6 simulations (Fig. 3E-F), fall between  
413 panels 3A-B and 3C-D. While the observed 2002-2023 WVG value (-0.5Z) falls at the edge of  
414 the CMIP6 distribution (Fig. 3F), the CMIP6 ensemble does predict reductions in the WVG  
415 (Fig. 3E), due to the influence of human-induced warming in the Western V. Assuming that the  
416 CMIP6 WVG simulations are 'true', and that the lack of warming in the NINO3.4 region is  
417 natural, these results still indicate that about half of the observed increase in the WVG has been  
418 caused by climate change. If the CMIP6 models are over-estimating warming the NINO3.4  
419 region, then climate change would account for a greater portion of the observed decrease in  
420 WVG values.

#### 421 422 **4.2 Linking WVG events to large and energetic changes in the Walker Circulation**

423  
424 A better understanding of the processes that link Pacific SSTs and dry EA outcomes will help  
425 build confidence in dry season outlooks, which will make them more actionable. To that end we  
426 examine MAM WVG circulation anomalies using ERA5 and MERRA2 reanalyses. As discussed  
427 in the methods section, atmospheric heating is inversely correlated with the divergence of  
428 geopotential height energy (Fig. 4A-B), and the long term mean atmospheric heating (Fig. 4C)  
429 and geopotential divergence fields (Fig. 4D) help delineate the low and high pressure cells that  
430 comprise the global Walker Circulation.

431  
432 Climatologically, the atmospheric heating that drives the Walker Circulation can be visualized  
433 by examining maps of vertically integrated diabatic heating (Fig. 5A) and atmospheric heat  
434 convergence (Fig. 5B). These are the two terms on the right hand side of eq. 3. In the tropics,  
435 diabatic heating in the lower and middle troposphere destabilizes the atmosphere and produces  
436 lower surface pressures, which drives atmospheric heat convergence (Fig. 5B). We refer to the  
437 combination of diabatic heating and heat convergence as atmospheric heating. Because  
438 temperatures and water vapor are both larger in the lower troposphere, vertically integrated heat  
439 and moisture transports are very similar. Areas with strong moisture convergence will have  
440 heavy precipitation, and strong heat convergence, and large amounts of water vapor will trap  
441 longwave radiation. In the Indo-Pacific, this region is often referred to as the 'Warm Pool'. Fig.  
442 5A,B also show long term average moisture transports. The Pacific Trade winds feed very large  
443 transports of heat and moisture into the Warm Pool, linking the Walker Circulation to Pacific  
444 SSTs.

445  
446 In MAM, the Indian Ocean branch of the Walker Circulation can be characterized by strong  
447 atmospheric heating ( $>450\text{Wm}^{-2}$ ) in the eastern equatorial Indian Ocean, and heat divergence ( $<-$   
448  $270\text{Wm}^{-2}$ ) over the southern and equatorial western Indian Ocean (Fig. 5AB). This strong  
449 heating gradient produces a strong low-level pressure gradient associated winds that transport  
450 moisture across the southern Indian Ocean and into East Africa (arrows in yellow boxes Fig.  
451 5AB). Over the southern Indian Ocean ( $\sim 60\text{-}110^\circ\text{E}$ , between  $\sim 30^\circ\text{S}$  and  $5^\circ\text{S}$ ), we see mean  
452 atmospheric heating values change from strong cooling to strong heating. This atmospheric  
453 heating gradient is also associated with a strong meridional sea level pressure gradient that drives  
454 easterly moisture transports that drives easterly moisture transports that cross the equator and

455 feed moisture into EA. Longitude-by-height transects of climatological equatorial (5°S-5°N)  
456 ERA5 vertical velocities and zonal velocities reveal, on average, descending air tendencies  
457 between 40 and 55°E that heat and stabilize the atmosphere over the eastern Horn of Africa (Fig.  
458 5C). Thus, we see in terms of the long-term mean climate over the Indian Ocean offsetting  
459 contributions from atmospheric heating over the Indian Ocean Warm Pool. Over the southeastern  
460 Indian Ocean, the meridional gradient between extra-tropical cooling and tropical heating helps  
461 produce a strong pressure gradient associated with low-level moisture transports into EA (Fig.  
462 5B), but over the western and central equatorial Indian Ocean a zonal east-west heating gradient  
463 (Fig. 5B) helps set up an east-west response in vertical velocities (Fig. 5C) that helps suppress  
464 rainfall over the eastern Horn.

465  
466 We next explore ERA5 SSTs and atmospheric heating anomalies following the 12 recent post-  
467 1997 OND La Niña events, which we also refer to as ‘MAM WVG events’ (Fig. 5D-E), because  
468 all of these events have strong negative WVG values in MAM (Figure 2C). Composites based on  
469 actual MAM WVG values and EHoA MAM dry seasons all resemble Fig. 5D-E. We chose to  
470 use OND La Niña events to emphasize opportunities for long-lead prediction of MAM droughts  
471 following La Niña-related OND dry seasons.

472  
473 A composite mean of the post-OND-La Niña MAM SST anomalies has a WVG structure (Fig.  
474 5D), but also reveals interesting SST cooling in the central Indian and warming in the  
475 southwestern Indian Ocean. This Indian Ocean SST gradient is associated with moisture  
476 transport anomalies that flow from over the southern Indian Ocean, and then turn east, towards  
477 the eastern Indian Ocean (Fig. 5E). These transport anomalies exhibit enhanced anticyclonic  
478 flow around that deflects moisture southward along the western flank of the Mascarene High.  
479 This is consistent with findings of Wainwright et al. [Wainwright et al., 2019] indicating that the  
480 late onset in MAM rainfall is linked with warmer SSTs over the south western Indian Ocean by  
481 delaying the northward movement of the tropical rainfall belt.

482  
483 These MAM WVG events are associated with large statistically significant changes in  
484 atmospheric heating in the Indo-Pacific Warm Pool (100-150°E, 15°S-15°N) and Central Pacific  
485 (150°E-170°W, 8°S-6°N) (Fig. 5D, Table 2). These results identify a very large westward  
486 transition in equatorial western-central Pacific heating. Driven both by diabatic heating and heat  
487 convergence, these large shifts indicate a westward shift of peak atmospheric heating, with  
488 increased subsidence near the equatorial dateline, increased equatorial Pacific moisture and heat  
489 transports, and increased Warm Pool heating.

490  
491 Over the Indian Ocean we also see an interesting, and statistically significant, increase in  
492 atmospheric heating over the Northern Indian Ocean (60-100°E, 15°S-6°N), and some small  
493 atmospheric heating decreases over the central Indian Ocean (60-100°E, 15°S-6°N) (Fig. 5E).  
494 Dry season SST composites (Fig. 2A) show fairly large (-1.2 to -0.6Z) and significant cooling  
495 anomalies over the central Indian Ocean as well, contributing to an enhanced equatorial SST  
496 gradient between the central Indian Ocean and the Warm Pool. Increased Warm Pool and North  
497 Indian Ocean atmospheric heating, combined with less heating over the Central Indian Ocean  
498 appears associated with anomalous westerly moisture transports across the equatorial Indian  
499 Ocean, away from EA. This can be seen as an eastward shift of the climatological transport  
500 fields, which typically flow into EA (Fig. 5B). These exchanges of heat and moisture modulate

501 the Walker Circulation, increasing heating and moisture convergence over the Warm Pool and  
 502 northern Indian Ocean, and decreasing these quantities over the central Indian and Pacific Ocean.  
 503 Table 2 lists the diabatic heating, heat convergence, and moisture convergence anomalies for  
 504 recent WVG events and 1981-2022 dry EA MAM seasons. Energy terms are in  $\text{Wm}^{-2}$ , while  
 505 moisture convergence is in total mm per MAM season. Increases in convergence in the Warm  
 506 Pool and Northern Indian Ocean are highly significant and large.

507  
 508 As discussed in the methods section, areas of increased or decreased atmospheric heating also  
 509 correspond to areas with decreasing or increasing divergence of geopotential height energy (Fig.  
 510 4), because heating and geopotential height energy are tightly coupled in a hydrostatic  
 511 atmosphere [Peixoto and Oort, 1992]. In the Central Pacific and Central Indian Ocean, increased  
 512 geopotential height energy stabilizes the atmosphere and increases surface pressures. Conversely,  
 513 in the Warm Pool and northern Indian Ocean, we find increased height divergence and lower  
 514 surface pressures. This supports strong zonal moisture and heat transport anomalies flowing from  
 515 over the Central Indian and Pacific into the Warm Pool (Fig. 5E).

516  
 517 Correlations of equatorial 1981-2022 WVG/ERA5 vertical and zonal velocities and specific  
 518 humidity (Fig. 5F) reveal a Walker Circulation enhancement, consisting of a Warm Pool versus  
 519 central Pacific dipole, and a weaker but still significant response over the Indian Ocean. The  
 520 latter appears associated with subsidence in the middle and lower troposphere, westerly wind  
 521 anomalies, and reduced atmospheric water vapor in the lower half of the troposphere between  
 522  $40^{\circ}\text{E}$  and  $100^{\circ}\text{E}$ . As discussed above, climatological conditions relate equatorial Indian Ocean  
 523 Warm Pool atmospheric heating to offsetting factors: moisture transports across the southern  
 524 Indian Ocean (Fig. 5AB), and subsidence between  $40^{\circ}\text{E}$ - $55^{\circ}\text{E}$ . WVG events increase atmospheric  
 525 heating over the northern Indian Ocean and decrease atmospheric heating over the central Indian  
 526 Ocean (Fig. 5E, Table 2), while also increasing the zonally overturning Walker Circulation (Fig.  
 527 5F). Over East Africa, this reduces atmospheric moisture and vertical motions in the mid-  
 528 troposphere (Table 3).

529  
 530 Strong links between an enhanced Walker Circulation and dry outcomes during the EA MAM  
 531 season are shown in Figure 6A,C. These scatterplots identify the very strong covariation between  
 532 Warm Pool heating and moisture convergence (ERA5  $R=0.99$ , MERRA2  $R=0.98$ ,  $p=0.0001$ ).  
 533 This strong correlation is not surprising. Heat and moisture transports are very similar, being  
 534 driven primarily by low-level winds. Increased moisture convergence increases precipitation and  
 535 latent heating (Eq. 4). More moisture increases the trapping of longwave radiation. What is  
 536 striking, however, is 1) how variable these terms are, and 2) how well intense heating and  
 537 moisture convergence discriminates dry EA seasons, as indicated by the circle colors.

538  
 539 The first point matters. If year-to-year variations in the Warm Pool were small, they would not  
 540 be likely drivers of EA droughts. But what we see in the ERA5 and MERRA2 are very large  
 541 ranges, with heating and moisture convergence ranging from  $\sim 150$  to  $\sim 700 \text{ Wm}^{-2}$  and  $\sim 50$  to  
 542  $\sim 350 \text{ mmMAM}^{-1}$ . These data exhibit a  $\sim$ six-fold change between the weakest and strongest  
 543 seasons. During the more intense seasons, when ERA5 heating exceeds  $\sim 500 \text{ Wm}^{-2}$ , as indicated  
 544 by the vertical black line in Fig. 5A,C, we see frequent dry EA outcomes and few wet or normal  
 545 seasons. Furthermore, the circle with black crosses reveal that many of these strong  
 546 heating/convergence years are strong MAM WVG events that followed OND La Niñas. OND La

547 Niñas are very robust indicators of strong MAM Warm Pool heating and moisture convergence  
548 ... up to six months in the future. Interestingly, the 2018 WVG was associated with low heating  
549 and convergence values, and very heavy rains, likely due to the influence of sub-seasonal MJO  
550 and cyclone influences [Kilavi *et al.*, 2018]. It should be noted, also, that moderate and low  
551 heating/convergence outcomes have few droughts, but there does not appear to be a strong  
552 connection to wet season frequencies. These results support the idea that dry seasons are  
553 predictable because of links to Pacific SSTs (Fig. 2A), while wet seasons are less predictable  
554 (Fig. 2B), because forcing from Warm Pool is limited.

555  
556 Scatterplots showing Warm Pool heating and Western V SSTs (Fig. 6B,D) also support links  
557 between Western V warming, Walker Circulation enhancements and frequent EA droughts.  
558 Warm Pool heating is strongly linked to warmer Western V SSTs. The 1981-2022 correlations  
559 between Western V SSTs and ERA5 and MERRA2 atmospheric heating are 0.74 and 0.70 (df.  
560 40,  $p=0.0000001$ ). Very warm Western V SSTs are clearly associated with increased Warm Pool  
561 atmospheric heating, and when Western V SSTs exceed +0.8Z, we find frequent dry EA rainy  
562 seasons (8 out of 12 seasons). We have already discussed the strong link between Western V  
563 SSTs and human-induced warming (Fig. 3A,B).

564  
565 Past research [Funk *et al.*, 2018; Funk *et al.*, 2019] has described how warm Western V and  
566 Western North Pacific SSTs are associated with ridging aloft, producing high pressure anomalies  
567 that encircle the twin equatorial upper lows associated with La Nina events, as represented by the  
568 Matsuno-Gill model [Gill, 1980]. The twin upper-level lows are at  $\sim 150^\circ\text{W}$ , at  $\sim 15^\circ\text{S}$  and  $15^\circ\text{N}$ ;  
569 while upper-level ridging is located both in the extra-tropical Pacific ( $\sim 170\text{-}150^\circ\text{W}$ ,  $\sim 45^\circ\text{S}$  and  
570  $\sim 45^\circ\text{N}$ ) and over the equatorial Western Pacific ( $\sim 150^\circ\text{E}$ ,  $20^\circ\text{S}$ - $2^\circ\text{N}$ ; Figures 5 and 6 in  
571 reference[Funk *et al.*, 2018]). These figures show that the resulting geopotential height gradients  
572 disrupt the sub-tropical westerly jets, increasing upper-level geopotential height convergence  
573 near the equatorial Central Pacific, amplifying the easterly flows of heat and moisture into the  
574 Warm Pool, and disrupting the Indian Ocean branch of the Walker Circulation.

575  
576 Figures 5 and 6 highlight opportunities for prediction. As highlighted by the repeated use of  
577 green crosses, OND La Niñas are associated with predictable negative MAM WVG values (Fig.  
578 2C) and strong Warm Pool atmospheric heating, and moisture convergence, and very warm  
579 Western V SSTs (Fig. 6). Over eastern East Africa, ERA5 and MERRA2 indicate highly  
580 significant and large ( $\sim 1$  sigma) decreases in total precipitable water during strong WVG MAM  
581 seasons; in the mid-troposphere subsidence also increases significantly (Table 3). Often arising  
582 in conjunction or after an OND La Niña event, these teleconnections set the stage for sequential  
583 but often predictable dry seasons. Thus La Niña-related MAM droughts are predictable because  
584 of reliable and predictable WVG conditions (Fig. 2D, 5D), and Walker Circulation  
585 enhancements (Fig. 5E, Fig. 6).

586  
587 This section has focused on the 1981-2022 satellite-observation period, for which we have good  
588 rainfall observations, reanalyses and SSTs. Over this period, we can say with great certainty that  
589 most MAM EA dry seasons were associated with more heating and moisture convergence in the  
590 Warm Pool and northern Indian Ocean, following La Niñas, when there have been predictable  
591 very warm Western V and WVG SST conditions. We next shift to a 1950-2022 time period to

592 examine the ‘East African Enigma’, to better understand some of the predominant features that  
593 differentiate “modern era” post-1997 La Niña events from earlier ones.

594

#### 595 **4.3 Contrasting MAM circulations following 1998-2022 and 1950-1997 OND La Niñas**

596

597 An important, but analytically challenging, aspect of the EA Paradox is a potential shift in links  
598 to La Niña. There is general agreement on a shift in Pacific SST following the 1997/98 El Niño  
599 [*L’Heureux et al.*, 2013; *Lyon et al.*, 2013; *Yang et al.*, 2014]. Following this event, Western V  
600 SSTs increased [*Funk et al.*, 2019] and the Western V Gradient decreased substantially (Fig. 2C).  
601 Since the early 2010s, it has been hypothesized that the interaction of La Niña events and a low-  
602 frequency warming [*Williams and Funk*, 2011] may enhance the link between La Niña and dry  
603 EA MAM seasons, and recent work on this important topic [*Park et al.*, 2020] shows clearly the  
604 increasing correlation between boreal winter ENSO SSTs and EA rains in the following MAM  
605 season. Park et al. (2020) describe how a westward intensification of the Walker Circulation  
606 enhances links to Pacific SST variations, with 2000-2016 zonal equatorial vertical velocities, 200  
607 hPa velocity potential and winds exhibiting ENSO teleconnections between 50°E and 180°E.

608

609 The recent availability of 1950-2022 ERA5 reanalysis, gives us an exciting opportunity to map  
610 the change in atmospheric heating and moisture convergence during the MAM seasons following  
611 the 12 post-1997 OND La Niñas versus the 12 1950-1997 La Niñas. While not identical, these  
612 results (Fig. 7A) broadly resemble WVG events (Fig. 5E), this implies a change in the behavior  
613 of the ‘modern’ MAM seasons that follow OND La Niñas. Fig. 7A indicates stronger  
614 atmospheric cooling and higher low-level air pressures over the southeastern Indian Ocean and  
615 central Indian Ocean, and an interesting negative IOD-like heating increase in atmospheric  
616 heating over the eastern equatorial Indian Ocean, i.e. an intensification of the Indian Ocean  
617 branch of the Walker Circulation. This increased atmospheric heating appears associated with  
618 higher pressures over the central Indian Ocean, and northward moisture transport anomalies that  
619 cross the equator near 75°E and turn towards Indonesia. In a sense, the eastward edge of the  
620 climatological moisture transports over the Indian Ocean (Fig. 5A) has shifted east, increasing  
621 over the central Indian Ocean (yellow arrow in Fig. 7A). Stronger eastward transports from over  
622 the central Pacific feed more heat and moisture into the Indian Ocean Warm Pool. This pattern is  
623 not associated with the western Indian Ocean, but rather the difference between the tropical  
624 central Indian Ocean and the Indo-Pacific Warm Pool, where WVG SST composites also  
625 indicate a dipole structure (Fig. 5D,E).

626

627 Given the strong relationship between dry EA seasons and Warm Pool atmospheric heating (Fig.  
628 6A,C), we can contrast ERA5 MAM Warm Pool heating Probability Distribution Functions  
629 (PDF) for pre-and-post 1997 La Niña events (Fig. 7B). A  $\sim 110 \text{ Wm}^{-2}$  increase in heating is  
630 identified, and this distribution shift increases the probability of exceeding a  $500 \text{ Wm}^{-2}$  threshold  
631 from 24% to 58%. Recent OND La Niñas anticipate much more energetic MAM Walker  
632 Circulations. These results can help explain why predicted WVG events (Fig. 2D) are good  
633 indicators of elevated EA MAM drought risk, and why there has been a large shift in EA MAM  
634 SPI PDFs following pre-and-post 1998 La Niña events (Fig. 7C). Since 1998, when there has  
635 been an OND La Niña, there have been strong MAM WVG gradients (Fig. 2C), very warm  
636 Western V SSTs (Fig. 5D), and strong Warm Pool heating and convergence (Fig. 6). These

637 results, and the large and significant changes shown in Fig. 7A, help explain why 75% of the  
638 time EA MAM rains are poor, when a La Niña arrives during boreal fall.

639  
640 It is important to note, however, that dry EA MAM seasons are linked to the overall Pacific SST  
641 gradient structure, not just the NINO3.4 region (Fig. 2A). For example, during three of the nine  
642 seasons with boreal fall La Niña and dry MAM outcomes (2001, 2009, 2017), NINO3.4 SST  
643 values did not meet the ONI La Niña criteria during MAM, yet these seasons had strong negative  
644 WVG values and large Warm Pool heating values [ $>460 \text{ Wm}^{-2}$ ]. Looking to the large-scale  
645 WVG more extensively resolves the large-scale SST patterns that arise from the interaction of  
646 natural ENSO variability and anthropogenic warming trends. The next section discusses the  
647 latter more in detail.

#### 648 649 **4.4 Relating Warm Pool heating and more frequent droughts to anthropogenic warming in** 650 **the Western V**

651  
652 We next explore low frequency (20-yr) links between MAM Pacific SSTs, Warm Pool heating,  
653 and EA dry season frequencies. The value of diagnostic analyses focused on atmospheric heating  
654 and moisture transport/convergence patterns (i.e. sections 4.2 and 4.3) is that they enable us to  
655 quantify the changes in climatic forcing associated with SST gradients. The WVG, by itself, is  
656 somewhat arbitrary, given that we weight equally the standardized Western V and NINO3.4  
657 regions. While studies examining the ENSO-residual West Pacific Warming Mode (WPWM)  
658 have suggested that Western V-like SSTs amplify the Walker Circulation [*Funk and Hoell, 2015;*  
659 *2017*], an important question that we address here is ‘*how influential is the Western V, in*  
660 *comparison with ENSO, as represented by NINO3.4 SST?*’.

661  
662 To set the stage for this analysis, we briefly present an updated analysis (Fig. 8) of the 1900-  
663 2022 ENSO and WPWM principal components (PC), as in Funk and Hoell (2015). ENSO in this  
664 study, as in [*Lyon et al., 2013*], is represented by the first EOF/PC of tropical Pacific SSTs. This  
665 PC tracks closely with SST in the NINO3.4 region (Fig. 8A). The ENSO PC and NINO3.4  
666 average SST time-series have a 1950-2022 correlation of 0.94. To estimate the WPWM, each  
667 grid cell’s MAM SST is regressed against the ENSO PC. Then the 1<sup>st</sup> EOF of the global  
668 residuals is used to define the WPWM, which tracks closely with the Western V. The WPWM  
669 PC and Western V average SST time-series have a 1950-2022 correlation of 0.87. An identical  
670 calculation of the WPWM, based on large ensembles of climate change models, are very similar  
671 to the observed patterns [*Funk and Hoell, 2015; 2017*]. Western V warming is not primarily  
672 driven Pacific Decadal Variability. Time-series of the WPWM/ENSO PCs (Fig. 8C) and Western  
673 V/NINO3.4 (Fig. 8D) are very similar. In broad strokes, two transitions appear in these time-  
674 series. First, the ENSO/NINO3.4 time-series have a Pacific Decadal Oscillation-related [*Mantua*  
675 *and Hare, 2002*] increase in the late 1970s, but thereafter show little increase [*Seager et al.,*  
676 *2022*]. Then, the WPWM/Western V trends upward, with post-1998 values being especially  
677 warm. It is worth noting that the MAM 2022 WPWM and Western V values appear to be, by a  
678 substantial margin, the warmest on record.

679  
680 We next use linear regression to relate 20-yr MAM Western V and NINO3.4 SST values to 20-yr  
681 1950-2022 ERA5 Warm Pool atmospheric heating. The blue bars in Fig. 9A show 20-yr average  
682 ERA5 Warm Pool Atmospheric heating. Between the first and last 20-year period we see a

683 substantial increase, from  $\sim 330$  to  $\sim 420$   $\text{Wm}^{-2}$ . Interestingly, a regression based on 20-yr  
 684 standardized Western V and NINO3.4 SST can explain 97% of the atmospheric heating variance.  
 685 The Western V and NINO3.4 coefficients are highly significant and roughly similar in  
 686 magnitude (58 and 67  $\text{Wm}^{-2}$  per standardized anomaly). These results are shown with a green  
 687 line in Fig. 9A. A regression carried out with just 20-yr Western V (red line Fig. 9A) explains  
 688 76% of the observed variance. Most of the 20-yr variance of the Warm Pool heating can be  
 689 explained by Western V warming. To examine the contribution of climate change, we can use  
 690 this equation ( $\text{HEAT}_{\text{WV}} = 386 + 44 * \text{Western V SST}$ ), but replace the observed Western V values  
 691 with the median of our large CMIP6 ensemble (Fig. 3A). These results are labeled as F(WestV-  
 692 CMIP6-50<sup>th</sup> Percentile SST) in Fig. 9A. 20<sup>th</sup> and 80<sup>th</sup> percentile CMIP6 estimates are also shown.

693  
 694 We would interpret these results as follows. First, the WVG formulation, which gives equal  
 695 weight to the Western V and NINO3.4 regions, seems fairly justified at 20-yr time-scales. 20-  
 696 year Warm Pool atmospheric heating covaries with both 20-yr NINO3.4 and Western V SSTs,  
 697 which in turn track closely with the first two models of global SST variability (Fig. 8). Between  
 698 the 1970s and 1990s a largely natural increase in NINO3.4 SSTs occurred [*Mantua and Hare,*  
 699 2002] (Fig. 3C), and we also see this reflected in the Warm Pool heating regression estimate,  
 700 which declined by about 40  $\text{Wm}^{-2}$  during this period. However, since the 1980s, the Western V  
 701 warmed substantially, and we find this associated with a large  $\sim 80$   $\text{Wm}^{-2}$  increase Warm Pool  
 702 heating.

703  
 704 Is the recent Western V warming largely due to climate change, or natural decadal variability?  
 705 While some studies, using detrended SSTs, have argued that western Pacific warming is largely  
 706 natural [*Lyon, 2014; Yang et al., 2014*], it is possible that the detrending process used in these  
 707 studies introduces biases into the results, since the rates of external forcing and associated  
 708 warming increase non-linearly. Assuming climate change is linear, and that residuals are  
 709 'natural' can miss the rapid human-induced warming present in the 1990s-2020s (Fig.3A). A  
 710 simpler approach is to compare directly observed 20-yr Western V SSTs with estimates from the  
 711 CMIP5 [*Funk et al., 2019*] or CMIP6 (Fig. 3A, Fig. 8A). CMIP6 20-yr Western V SST tracks  
 712 extremely well with the observations (median time series,  $R=0.98$ , 1950-2022). The heavy black  
 713 line in Fig. 9A translates the median CMIP6 Western V SST values into Warm Pool atmospheric  
 714 heating, in  $\text{Wm}^{-2}$ , using the empirical Western V regression coefficients. Differences between the  
 715 observed (red line) and externally-forced CMIP6 (heavy black line) 20-year Western V time-  
 716 series indicate the influence of natural Pacific Decadal Variability. These fluctuations are limited  
 717 to a small cooling in the 1980s and warming in the late-2000s. The dominant change in observed  
 718 20-yr running average Western V (red line) - the increasing trend - aligns with human-induced  
 719 warming (black lines). Between 1950 and 2022, CMIP6 Western V SST estimates suggest an  
 720 overall increase in Warm Pool atmospheric heating from  $\sim 340$  to  $\sim 410$   $\text{Wm}^{-2}$ . This shift in mean  
 721 Warm Pool heating is augmented further following recent La Niña events (Fig. 7A), helping to  
 722 explain the enigmatic increase in dry EA MAM seasons (33%  $\rightarrow$  75%, Fig. 7C).

723  
 724 Over the past 75 years, Western V SST have warmed by  $\sim +2Z$  standardized anomalies, and this  
 725 warming shifts the heating distribution by more than  $+80\text{Wm}^{-2}$ . Projections through 2050 suggest  
 726 another similar increase over the next 30 years (Fig. 9A). Such heating influence will likely be  
 727 particularly dangerous during or following La Niñas, setting the stage for more frequent  
 728 sequential OND/MAM droughts.

729  
730 In contrast to Western V SSTs, there is a large and growing discrepancy between observed east  
731 Pacific SSTs and CMIP6 projections, with “*observations-based SST trends ... at the far edge or*  
732 *beyond the range of modeled internal variability*” [Seager et al., 2022], there has been a notable  
733 lack of warming in the NINO3.4 region, and this is in marked contrast to 20-yr anomalies from a  
734 25-model 152-member ensemble of CMIP6 simulations (Fig. 3D). The observed 2003-2022  
735 value (-0.09Z) is extremely unlikely given the distribution from the CMIP6 simulations  
736 (Supplemental Fig. 4B). More detailed analyses [Wills et al., 2022] identify “*a triangular region*  
737 *in the eastern tropical and subtropical Pacific*” as the ocean region where CMIP6 model  
738 simulations differ most from observations, with the differences very unlikely (<5% probability)  
739 due to internal variability. While a detailed exploration is beyond the scope of this study,  
740 systematic Pacific SST biases are one likely cause of this discrepancy, and when bias-corrected  
741 ocean and atmosphere models are used to explore this issue, they recreate the observed increase  
742 in equatorial Pacific zonal SST gradients [Seager et al., 2019]. Hence assuming that the climate  
743 change models are ‘correct’ and that the observed lack of warming is driven by naturally-  
744 occurring Pacific Decadal Variability appears problematic.

745  
746 Finally, we present regressions relating 20-yr NINO3.4 and Western V SSTs to 20-yr dry season  
747 frequencies, i.e. the number of times in each 20-yr period in which EA MAM SPI was less than -  
748 0.44Z (Fig. 9B). The F(Observed WestV SST) time-series denotes a set of probability estimates  
749 derived via a linear regression using observed Western V SSTs as a predictor and 20-yr running  
750 observed frequencies of dry East African seasons as a predictand: ( $\text{PROB}_{\text{dry}} = 0.3 + 0.13\text{WV}$ ,  
751  $R^2 = 0.74$ ). Western V SST increases can explain most of the 20-yr variance in 20-yr changes in  
752 the frequency of dry seasons. These results suggest that the Western V warming has been a  
753 primary driver of increased dry season frequencies in the eastern Horn of Africa. Since Western  
754 V warming has been dominated by human-induced external forcing, climate change has been a  
755 strong driver of increased dry season frequencies in East Africa.

756

## 757 **5 Conclusions**

758

### 759 **5.1 A Walker Circulation intensification can explain the enigma predictability of the EA** 760 **MAM rains.**

761

762 Here, we have addressed a quite specific question – do intensifications of the Walker  
763 Circulations help explain the “East Africa Climate Enigma”, i.e. the fact that so many recent  
764 OND La Niñas are followed by below-normal MAM EA rainy seasons. Furthermore, how does  
765 this link relate to climate change and the large observed decline in EA MAM rains (Fig. 1B)? We  
766 have addressed these questions in a two-step attribution process. The first step links observed EA  
767 droughts to decreasing but predictable WVG values (Fig. 2). These strong Pacific gradients, we  
768 argue, are being produced through an interaction of naturally occurring La Niña events and  
769 human-induced warming in the Western V region (Fig. 2C, Fig. 3A,B). The second step then  
770 links WVG events to changes in the Walker Circulation and conditions over EA (Fig. 5-6, Tables  
771 2,3).

772

773 These 1981-2022 results paint a clear story that helps us understand the predictability of MAM  
774 dry seasons. First, we see a large, climate-change-related warming of the Western V region,  
775 well-reproduced in the CMIP6 (Fig. 3A,B). This warming, combined with the influence of La  
776 Niña, results in very reliable low WVG values during MAM seasons following OND La Niñas  
777 (Fig. 2C). These gradients, furthermore, are predicted well by seasonal climate prediction  
778 systems (Fig. 2D). MAM EA rains, furthermore, have very often been poor following post-1997  
779 OND La Niñas (Fig. 7C), consistent with increasing ENSO teleconnections [Park *et al.*, 2020].  
780

781 To make such insights more actionable, however, we have tried to provide a clear causal  
782 description linking WVG conditions to dry EA rains. To this end we have used gradients in  
783 atmospheric heating to help describe the Indo-Pacific Walker Circulation. In terms of the long  
784 term mean climate, these fields identify the regions of high and low pressure that help guide  
785 moisture transports into the Warm Pool and eastern Horn (Fig. 5B), which in turn help setup  
786 zonally-overturning wind patterns along the equator (Fig. 5C).  
787

788 Composites of SSTs, atmospheric heating and moisture transports, following post-1997 La  
789 Niñas, show significant and substantial changes in SSTs (Fig. 5D) and atmospheric  
790 heating and moisture transports (Table 2, Fig. 5E). These large and significant changes (Table 2)  
791 can be anticipated many months ahead of the MAM rains, since these composites are based on  
792 lagged OND La Niña definitions. Warm Pool intensification arises through both increased  
793 diabatic heating and increased heat and moisture convergence (Table 2). Over EA, we find  
794 corresponding decreases in total precipitable water and increases in mid-tropospheric subsidence  
795 (Table 3).  
796

797 Scatterplots of Warm Pool atmospheric heating and moisture convergence (Fig. 6A,C) very  
798 strongly support the link between Walker Circulation enhancements and dry EA outcomes.  
799 When ERA5 heating exceeded  $450 \text{ Wm}^{-2}$  there were 9 dry seasons, 2 normal seasons and 2 wet  
800 seasons. Strong Warm Pool heating in MERRA2 reanalyses similarly discriminate dry outcomes.  
801 As previously hypothesized, Walker Circulation enhancements are a robust indicator of dry EA  
802 outcomes. Twelve post-1997 La Niñas were precursors to MAM SST anomalies (Fig. 5D) that  
803 strongly resemble dry season SST composites (Fig. 2A). And the associated circulation  
804 disruptions (Fig. 5E, Fig. 7AB, Table 2) appear linked to frequent droughts (Fig. 1B), but offer  
805 opportunities for prediction (Fig. 2D). The energetic framework provided here helps us explain  
806 these opportunities. While we only have  $\sim 12$  events, we see that Warm Pool heating and  
807 moisture convergence increases dramatically during most of these seasons (Fig. 6A,C) and when  
808 compared to the MAM seasons following 1950-1997 La Niñas (Fig. 7A-B).  
809

810 Thus, without ruling out other influences such as westerly Congo Basin moisture transports and  
811 the MJO [Finney *et al.*, 2020], or sub-seasonal changes in the length of the long rains  
812 [Wainwright *et al.*, 2019], the results presented here support the idea that one primary cause of  
813 recent EA droughts has involved a large westward shift in atmospheric heating between the  
814 equatorial central Pacific and Warm Pool regions during WVG seasons. These regions exhibit  
815 the largest atmospheric heating anomalies. But, as shown by Gill [Gill, 1980], increased heating  
816 in the Warm Pool may increase subsidence and low-level pressures to the west, changing  
817 circulation patterns over the Indian Ocean, providing proximate impacts that reduce moisture and  
818 vertical ascent over East Africa. Early studies linking EA drying with an increased Indian Ocean

819 branch of the Walker Circulation posited atmospheric heating over the central Indian Ocean  
820 [Funk *et al.*, 2008; Verdin *et al.*, 2005]; the work presented here suggests heating increases over  
821 Indian and Pacific Warm Pool regions, and underscores the amplifying role played by moisture  
822 and heat transports and convergence. This helps explain the link with Pacific SSTs [Lyon and  
823 DeWitt, 2012; Yang *et al.*, 2014] as well as the tendency for the long rains to start later and end  
824 earlier [Wainwright *et al.*, 2019]. Such insights could assist in the prediction of onset and  
825 cessation dates, which are linked to zonal wind variations over the Indian Ocean [MacLeod,  
826 2018].

827  
828 Our WVG composites (Fig. 5D) also identify Indian Ocean SST warming over the southwest and  
829 northern Indian Ocean, and cooling near 75°E, 15°S. Recent analysis has suggested a later start  
830 and earlier cessation of the long rains [Wainwright *et al.*, 2019], and this may be consistent with  
831 the observed WVG SST responses, and expectations that La Niña-like conditions will tend to  
832 slow the onset and hasten then end of the rainy season. In the southern Indian Ocean, during  
833 WVG events (Fig. 5D), warmer southwestern SSTs could delay the typical northward  
834 progression of the rains between February and March. In the central and northern Indian Ocean,  
835 during WVG events (Fig. 5D,E, Table 2), warmer SSTs in the northern Indian Ocean (Fig. 5D)  
836 and increased atmospheric heating over the northern Indian Ocean, combined with cooler SSTs  
837 and less heating over the central Indian Ocean, might also help trigger an early transition to the  
838 boreal summer Indian Monsoon circulation, which could reduce rainfall in May. The contrasting  
839 heating responses over the northern and central Indian Ocean (Fig. 5E) help drive moisture and  
840 heat into the Warm Pool, and away from EA. This may suggest a ‘Walker Circulation  
841 Intensification’ over the northern Indian Ocean, perhaps leading to an earlier transition to a  
842 boreal summer monsoon pattern, similar to the June-August circulation. Hence, the increased  
843 frequency of strong WVG events, especially following recent La Niñas, appears related to the  
844 shorter EEA rainy season as described by Wainwright *et al.* [Wainwright *et al.*, 2019]. Climate  
845 change assessments, based on regional climate model results [Gudoshava *et al.*, 2020], have  
846 suggested that the long rains will start and end earlier. This earlier start projection, which appears  
847 at odds with the observations, may be related to a tendency for the global climate change models  
848 to predict an El Niño-like tendency in Pacific SSTs (Fig. 3C,D), and the well-established north-  
849 south rainfall dipole associated with ENSO, with southern (eastern) Africa being drier (wetter)  
850 during El Niños.

851  
852 In our La Niña atmospheric heating analysis (Fig. 7A), on the other hand, we find enhanced  
853 atmospheric heating primarily in the south-eastern Indian Ocean, where recent La Niñas appear  
854 associated with  $>160 \text{ Wm}^{-2}$  more heating than pre-1998 events. In the absence of strong Walker  
855 Circulation forcing, sub-seasonal influences such as the MJO, and more local weather influences  
856 such as westerly Congo basin moisture transports likely play an important role [Finney *et al.*,  
857 2020]. The MJO, of course, modulates the Walker Circulation and East African rains as well,  
858 and certainly influences heating and moisture transports. Recent research has linked a two-fold  
859 expansion of Warm Pool to a modulation of the MJO life cycle [Roxy *et al.*, 2019], with  
860 Maritime Continent residence times increasing by 5-6 days and Indian Ocean residence times  
861 decreasing by 3-4 days. Analyses of global satellite-gauge precipitation trends [Adler *et al.*,  
862 2017], have noted marked increases WVG-like SSTs, Warm Pool total precipitable water and  
863 precipitation (c.f. their Fig. 8), consistent with a strong equatorial Pacific SST gradient [Seager  
864 *et al.*, 2022; Seager *et al.*, 2019].

865 In closing, when one considers the ‘cause’ of the EA rainfall decline, we would suggest that it is  
866 useful to consider two aspects: the increased impacts following recent La Niña events, and the  
867 high frequency of recent La Niña events themselves. In place of the ‘East African Climate  
868 Paradox’ we have suggested the ‘East Africa Enigma’: why have La Niña-related SST conditions  
869 become such a consistent driver of droughts during MAM? Our analysis of atmospheric heating  
870 and changes in moisture transports help explain how the combination of anthropogenic Western  
871 V warming and La Niña events leads to increases in Warm Pool heating, which in turn  
872 modulates important circulation features over the Indian Ocean, increasing subsidence and  
873 decreasing EA moisture levels (Table 3). Hence, the interaction of climate change and frequent  
874 La Niña events have led to frequent MAM droughts, and many of those dry seasons have  
875 followed poor OND outcomes [*Funk et al.*, 2018]. This is consistent with recent multi-agency  
876 alerts attributing the recent droughts to the combined influence of La Niña and climate change.  
877 Without climate change, there would not be a strong link to La Niñas (Figure 7A,B). It is worth  
878 noting that strong ‘gradient La Niñas’ have been identified in observations [*Johnson*, 2013], and  
879 are expected by climate change models [*Cai et al.*, 2022; *Cai et al.*, 2015a; *Cai et al.*, 2015b].

880 For EA, our study has emphasized the strong relationship between MAM atmospheric heating,  
881 WVG SST and EA SPI, given the set of all post-1997 OND La Niña events. Such conditions  
882 pose risks, even if a La Niña event fades. When these events commence, enhanced trade winds  
883 transport more oceanic heat energy from the east Pacific and into the Western V region, via the  
884 sub-tropical gyre, and there is a great deal of certainty that these transports will persist for many  
885 months. As oceanic heat content increases due to climate change, it is not surprising to see that  
886 these natural La Niña transport patterns result in large increases in Western V SSTs, and more  
887 negative WVG values (Fig. 2C), which are very predictable (Figure 2D). Western V SSTs, even  
888 in the absence of very cool NINO3.4 SSTs, still increase flows of heat and moisture into the  
889 Warm Pool atmosphere, which increase the risk of dry EA rainy seasons. Even if the frequency  
890 of La Niñas were to decrease in the future, La Niñas will develop in an environment that is very  
891 warm- and likely even warmer than present-day- and the conditions in the Warm Pool and  
892 Western V will likely amplify the impacts of these La Niñas, setting the stage for sequential dry  
893 East Africa outcomes in OND and MAM. It is also possible, however, that observed streak of La  
894 Niñas will continue, due to a stronger zonal Pacific gradient. CMIP6-based projections of Warm  
895 Pool atmospheric heating, based on Western V warming, suggest a further  $\sim 80 \text{ Wm}^{-2}$  increase by  
896 2050 (Fig. 9A). Understanding the emergent links between La Niñas, WVG and the Walker  
897 Circulation will help anticipate and manage risks.

## 898 **Acknowledgments**

899 This research was supported by the United States Agency for International Development  
900 (USAID) (Cooperative Agreement #72DFFP19CA00001), National Aeronautics and Space  
901 Administration (NASA) GPM mission Grant 80NSSC19K0686, and the Bill and Melinda Gates  
902 Foundation contract INV-017546.

903

## 904 **Availability Statement**

905 Please also note that we have produced a Dryad Data Repository with the time-series analyzed in  
906 this study. We have chosen a spreadsheet format to maximize accessibility. Even non-  
907 programmers can verify the basic results from our study. It is available at the link below.

908 <https://datadryad.org/stash/share/I2kn11CShPW0YDIUAA-La9IjaMHDmKLHoJzZYWCMmc8>

909

910 **Tables**

911

912 **Table 1.** The CMIP6 SSP245 models and simulations used in this study.

Model Names	Number of Simulations
ACCESS-CM2	3
ACCESS-ESM1-5	11
CanESM5-CanOE	3
CanESM5	25
CMCC-ESM2	1
CNRM-CM6-1-HR	1
CNRM-CM6-1	6
CNRM-ESM2-1	9
EC-Earth3-CC	1
EC-Earth3-Veg-LR	3
EC-Earth3-Veg	5
FGOALS-g3	4
FIO-ESM-2-0	3
GFDL-ESM4	3
GISS-E2-1-G	10
HadGEM3-GC31-LL	1
INM-CM4-8	1
INM-CM5-0	1
IPSL-CM6A-LR	11
MIROC6	3
MIROC-ES2L	30
MPI-ESM1-2-HR	2
MPI-ESM1-2-LR	9
MRI-ESM2-0	1
UKESM1-0-LL	5
<b>Total Number of Sims</b>	<b>152</b>

913

914

915

916

917 **Table 2.** Dry-Versus-West EA seasons and strong WVG season anomalies for selected forcing  
 918 regions. \*, \*\*, \*\*\* denote significance at  $p=0.1$ ,  $0.05$ , and  $0.01$ , based on two-tailed T-tests.  
 919 Moisture convergence is shown as the seasonal total moisture convergence.

	Warm Pool	Eq Central Pacific	Northern Indian	Central Indian
<b>Dry Seasons</b>				
Heat Convergence [ $\text{Wm}^{-2}$ ]				
ERA5	+78***	-85*	+51**	-32**
MERRA2	+95***	-130**	+42**	-14
Diabatic Heating [ $\text{Wm}^{-2}$ ]				
ERA5	+44***	-32	+29**	-13**
MERRA2	+77***	-55**	+45**	+3
Geopotential Divergence [ $\text{Wm}^{-2}$ ]				
ERA5	+108***	-112**	+67**	-51**
MERRA2	+128***	-178**	+63**	-16
Moisture Convergence [mm]				
MERRA2	+85***	-80	-45**	-49***
ERA5	+102***	-128**	-51**	-27*
<b>Strong WVG Seasons</b>				
Heat Convergence [ $\text{Wm}^{-2}$ ]				
ERA5	+123***	-178***	+81***	-49***
MERRA2	+133***	-206***	+74**	-36**
Diabatic Heating [ $\text{Wm}^{-2}$ ]				
ERA5	+66***	-81***	+48***	-19**
MERRA2	+95***	-114***	+86***	-40
Geopotential Divergence [ $\text{Wm}^{-2}$ ]				
ERA5	+169***	-250***	+110***	-76***
MERRA2	+172***	-287***	+160***	-91**
Moisture Convergence [mm]				
ERA5	+121***	-206***	+77***	-75***
MERRA2	+126***	-243***	+81***	-59

920

921

922

923

924 **Table 3.** Strong WVG season anomalies for Eastern East African MERRA2 and ERA5 Total  
 925 Precipitable Water and 600 hPa vertical velocities. \*, \*\*, \*\*\* denote significance at  $p=0.1$ , 0.05, and  
 926 0.01, based on two-tailed T-tests. Moisture convergence is shown as the seasonal total moisture  
 927 convergence. Anomalies also expressed as standardized anomalies. Eastern East Africa region  
 928 corresponds to 38-52°E, 5°S-8°N.

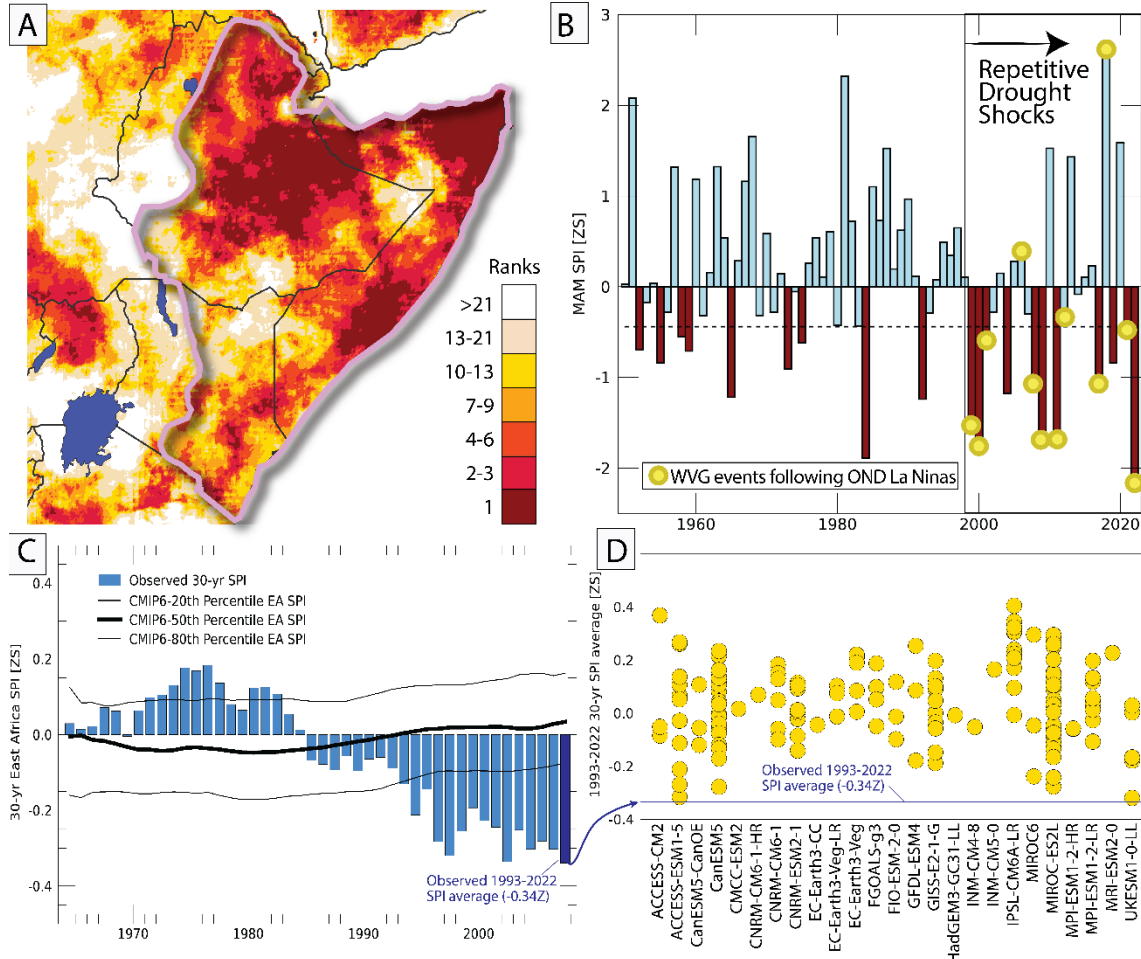
	Total Precipitable Water [ $\text{kgm}^2\text{s}^{-1}$ ]	Total Precipitable Water [Z-score]	600 hPa vertical velocity [ $\text{Pas}^{-1}$ ]	600 hPa vertical velocity [Z Score]
ERA5	-2.4***	-1.1Z***	+0.004**	+0.7Z
MERRA2	-2.2***	-1.0Z***	+0.003*	+0.5Z

929

930

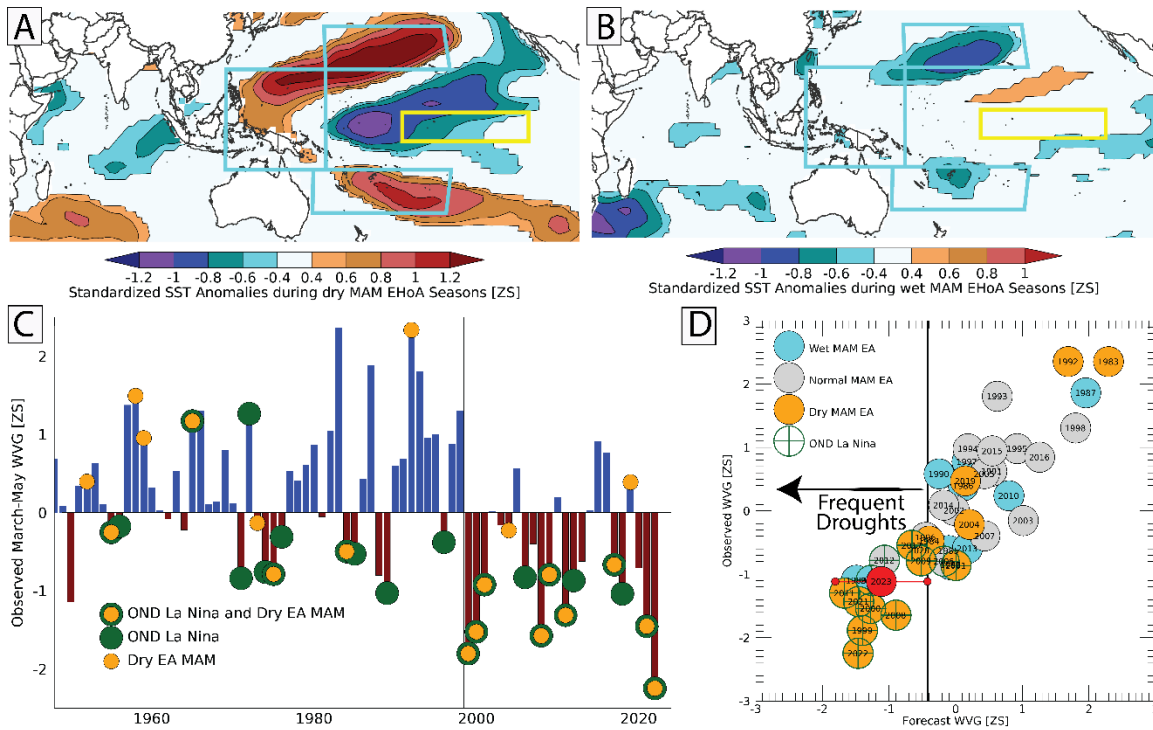
931

932 **Figures**  
 933

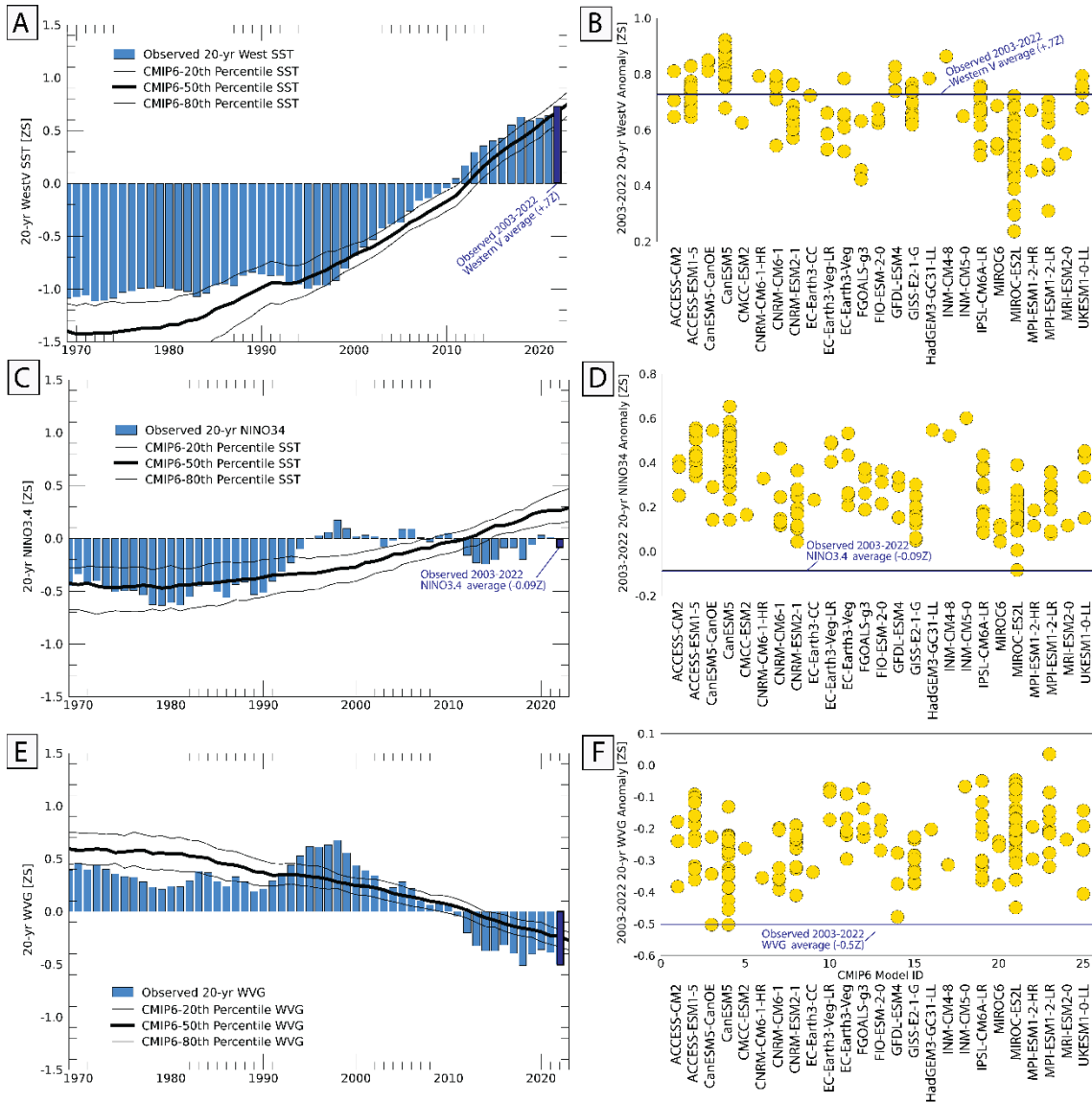


934 **Figure 1.** Describing the East African Climate Paradox. **A.** MAM 2022 rainfall ranks indicate  
 935 most of the Horn of Africa received extremely low rainfall amounts, based on 42 years of  
 936 CHIRPS rainfall. The purple polygon in Panel A denotes the area of exceptional dryness in  
 937 MAM 2022. **B.** Time-series of dry region MAM CHIRPS/Centennial Trends rainfall, expressed  
 938 as Standardized Precipitation Index (SPI) values). Also noted with yellow circles are strong  
 939 negative WVG seasons. **C.** Observed (blue bars) and projected CMIP6 SSP245 30-yr average  
 940 East Africa SPI. Centered on a 1981-2021 baseline. Based on 152 CMIP6 simulations. The thick  
 941 and thin black lines show the median and 20<sup>th</sup>/80<sup>th</sup> quantiles of the CMIP6 simulation  
 942 distribution. **D.** The 152 simulated CMIP6 2003-2022 20-yr average East Africa SPI, centered on  
 943 a 1981-2021 baseline. The horizontal line in Fig. 1D denotes the observed 1993-2022 average  
 944 East Africa SPI value (-0.34Z).  
 945

946  
 947  
 948

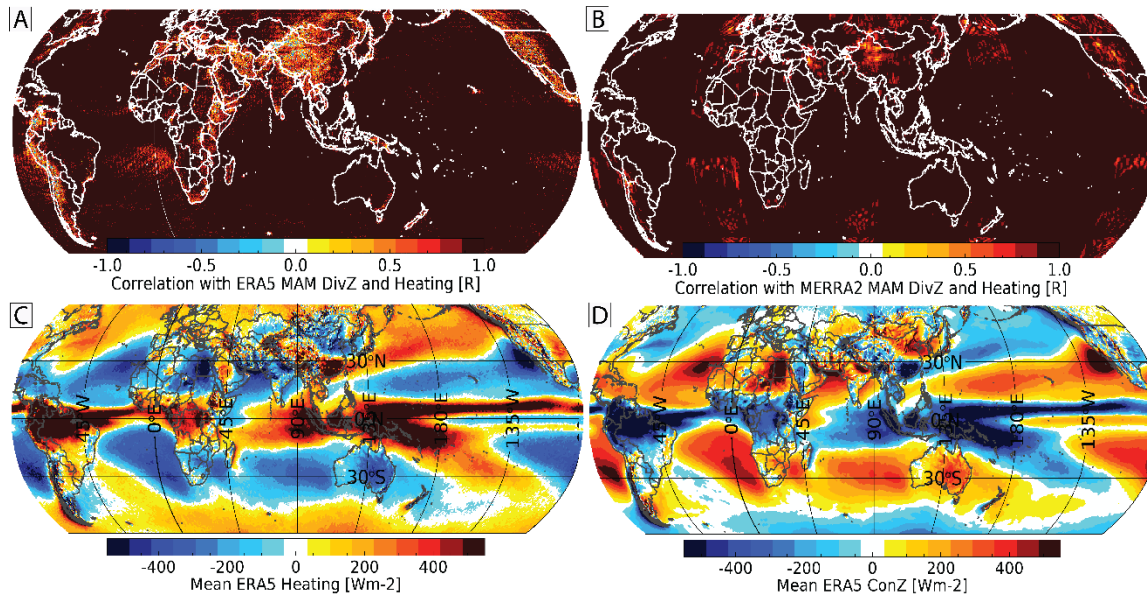


949 **Figure 2.** Relating dry seasons to the Western V gradient. **A-B.** Composites of standardized  
 950 SSTs during 1981-2022 dry seasons (**A**) and wet seasons (**B**) reveal a substantial non-linearity.  
 951 Dry seasons exhibit a coherent dipole pattern in the Pacific, while wet seasons SST anomalies  
 952 exhibit few areas with significant relationships. Wet and dry seasons based on 1981-2022 EA  
 953 SPI values of greater or less than +0.44 and -0.44. These breaks correspond with the top and  
 954 bottom tercile boundaries. Screened for significance at  $p=0.1$  using a two-tailed T-test. The cyan  
 955 boxes in A and B denote the equatorial [120-160°E, 15°S-20°N], northern [160°E -150°W, 20-  
 956 35°N], and southern [155°E -150°W, 30-15°S] regions of the ‘Western V’ area. The yellow box  
 957 denotes the NINO3.4 region in the eastern equatorial Pacific [170-120°W, 5°S-5°N]. The WVG  
 958 is the standardized difference between the NINO3.4 and Western V areas. **C.** A bar plot of  
 959 observed standardized MAM WVG values, centered on a 1981-2021 baseline. Orange circles  
 960 denote dry EA MAM seasons. Green circles denote preceding OND La Niña years. Orange  
 961 within green circles identify OND La Niña seasons followed by dry EA MAM events. The thin  
 962 vertical line at between 1998 and 1999 identifies the shift towards stronger WVG values and  
 963 more frequent dry EA MAM rainy seasons. **D.** Scatterplot showing forecasts of MAM WVG  
 964 index values, based on August NMME SST predictions. Observed MAM EA rainy season  
 965 outcomes shown with blue/gray/orange shading. All time-series and SST centered on a 1981-  
 966 2021 baseline. Also shown are preceding OND La Niña seasons, and the 2023 WVG forecasts.  
 967 The y-axis value has been set to the forecast value. 80% confidence intervals for the forecast are  
 968 also shown with small red circles and a horizontal red line.



970  
 971 **Figure 3.** Observed and CMIP6 SST time-series. **A.** Observed (blue bars) and CMIP6 SSP245  
 972 projections of 20-yr averages of standardized Western V SST anomalies. Centered on a 1981-  
 973 2021 baseline. CMIP6 results based on 152 CMIP6 simulations. The thick and thin red lines  
 974 show the median and 20<sup>th</sup>/80<sup>th</sup> quantiles of the CMIP6 simulation distribution. **B.** Individual  
 975 CMIP6 simulated 2003-2022 20-yr average Western V SST anomalies, centered on a 1981-2021  
 976 baseline. The horizontal line in Fig. 4B denotes the observed average 2003-2022 standardized  
 977 Western V SST anomaly (+0.7Z). **C-D.** Same but for standardized NINO3.4 SST anomalies. **E-**  
 978 **F.** Same but for standardized WVG index values.

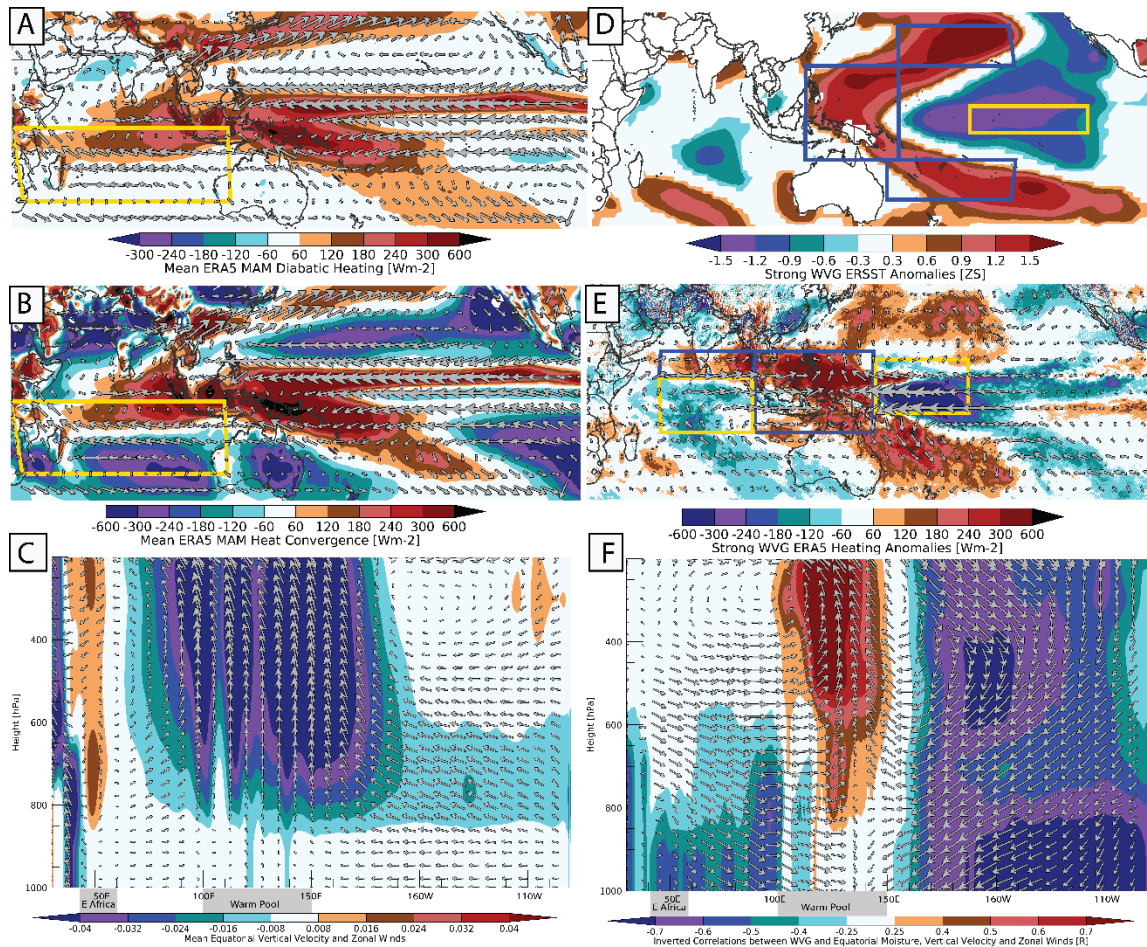
979



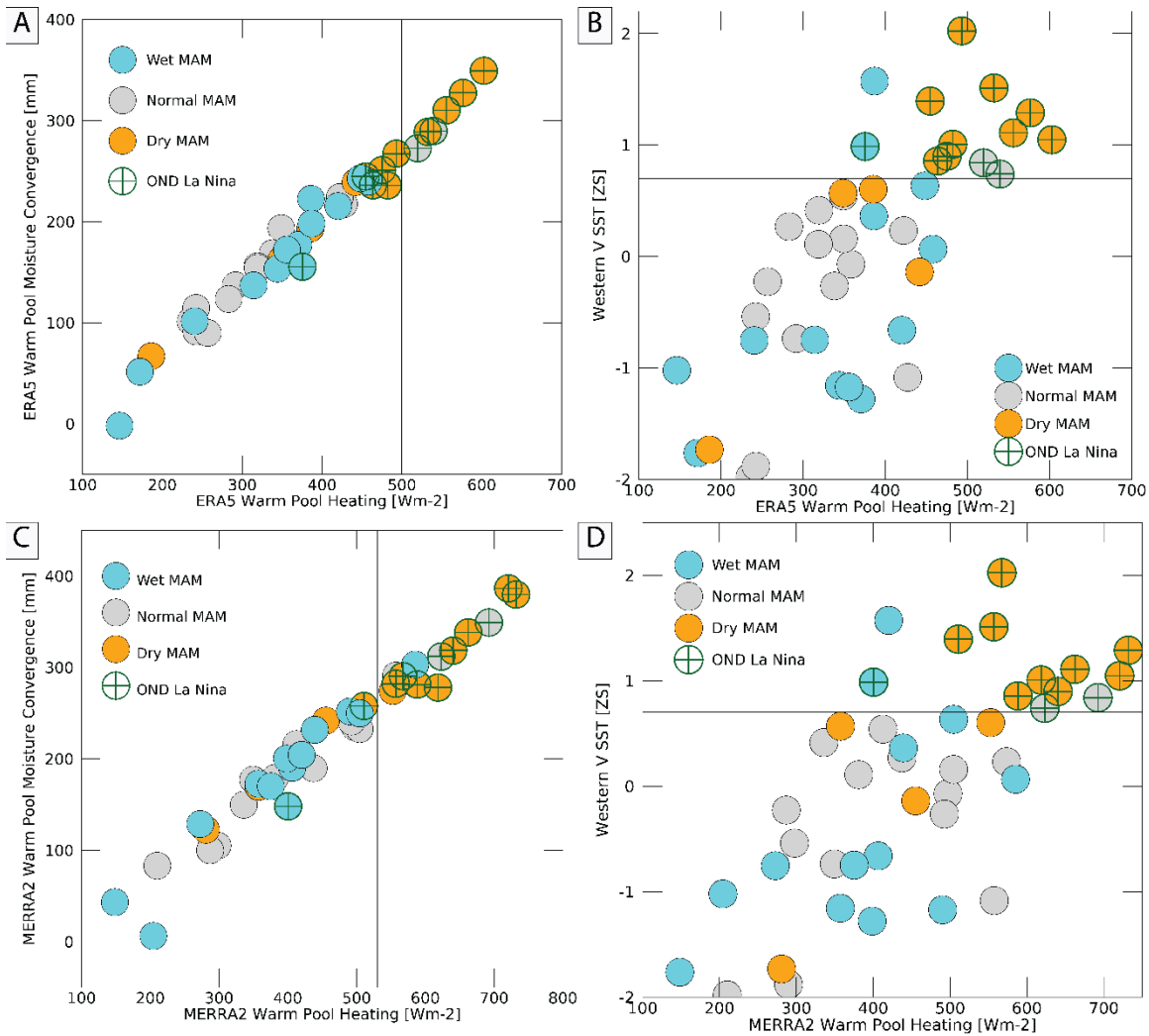
980  
981  
982  
983  
984  
985  
986  
987  
988

**Figure 4.** Geopotential height energy divergence offsets heating energy changes. **A-B.** 1981-2021 correlations between ERA5 (**A**) and MERRA2 (**B**) MAM atmospheric heating (diabatic heating + heat convergence) and geopotential height energy divergence. **C.** Long term (1981-2021) mean ERA5 atmospheric heating **B.** Same for geopotential height convergence.

989

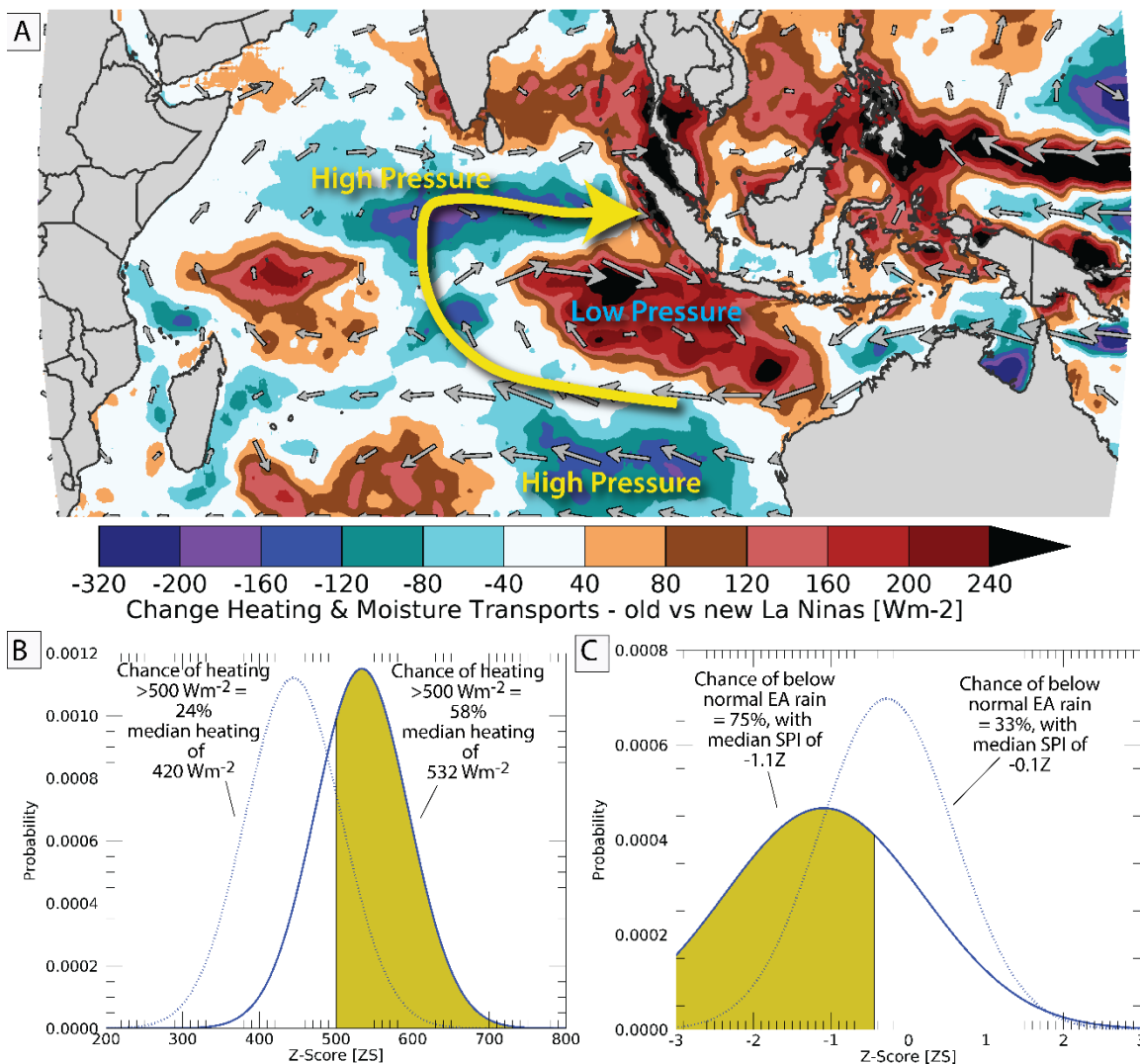


990  
 991 **Figure 5.** Relating WVG events to Walker Circulation intensification. **A.** Mean 1981-2021  
 992 ERA5 diabatic heating in  $\text{Wm}^{-2}$ . Vectors show ERA5 mean vertically-integrated moisture  
 993 transports, with a maximum westerly flux rate of  $-357 \text{ kgm}^{-1}\text{s}^{-1}$ . **B.** Same but for mean vertically  
 994 integrated atmospheric heat convergence. **C.** Long term mean ERA5 equatorial [ $5^{\circ}\text{S}-5^{\circ}\text{N}$ ]  
 995 longitude-by-height vertical and zonal velocities ( $\text{Pas}^{-1}$  and  $\text{ms}^{-1}$ ). Vertical velocities scaled by  
 996 200. **D.** Composites of standardized MAM SSTs during 1981-2022 strong WVG events (circles  
 997 in Fig. 1B). Screened for significance at  $p=0.1$  using a two-tailed T-test. **E.** Similar composites  
 998 but for ERA5 atmospheric heating (diabatic heating + atmospheric heat convergence) in  $\text{Wm}^{-2}$ .  
 999 Screened for significance at  $p=0.1$ . Also shown are ERA moisture transport anomalies, with a  
 1000 maximum westerly flux rate of  $-174 \text{ kgm}^{-1}\text{s}^{-1}$ . Also shown are areas of interest: Indo-Pacific  
 1001 [ $100-150^{\circ}\text{E}$ ,  $15^{\circ}\text{S}-15^{\circ}\text{N}$ ], Central Pacific [ $150-170^{\circ}\text{E}$ ,  $8^{\circ}\text{S}-12^{\circ}\text{N}$ ], northern Indian Ocean [ $60-$   
 1002  $100^{\circ}\text{E}$ ,  $5^{\circ}\text{N}-15^{\circ}\text{N}$ ], and central Indian Ocean [ $60-100^{\circ}\text{E}$ ,  $15^{\circ}\text{S}-5^{\circ}\text{N}$ ]. **F.** 1981-2022 correlations  
 1003 between equatorial ERA5 vertical and zonal velocity and moisture (specific humidity) and  
 1004 inverted observed WVG values (the time-series shown in Supplemental Fig. 1A). Since negative  
 1005 vertical velocities (in  $\text{Pas}^{-1}$ ) indicate upward motions (panel C), the vertical velocity correlations  
 1006 have been inverted, to indicate that stronger WVG values are associated with increased ascent  
 1007 over the Warm Pool.

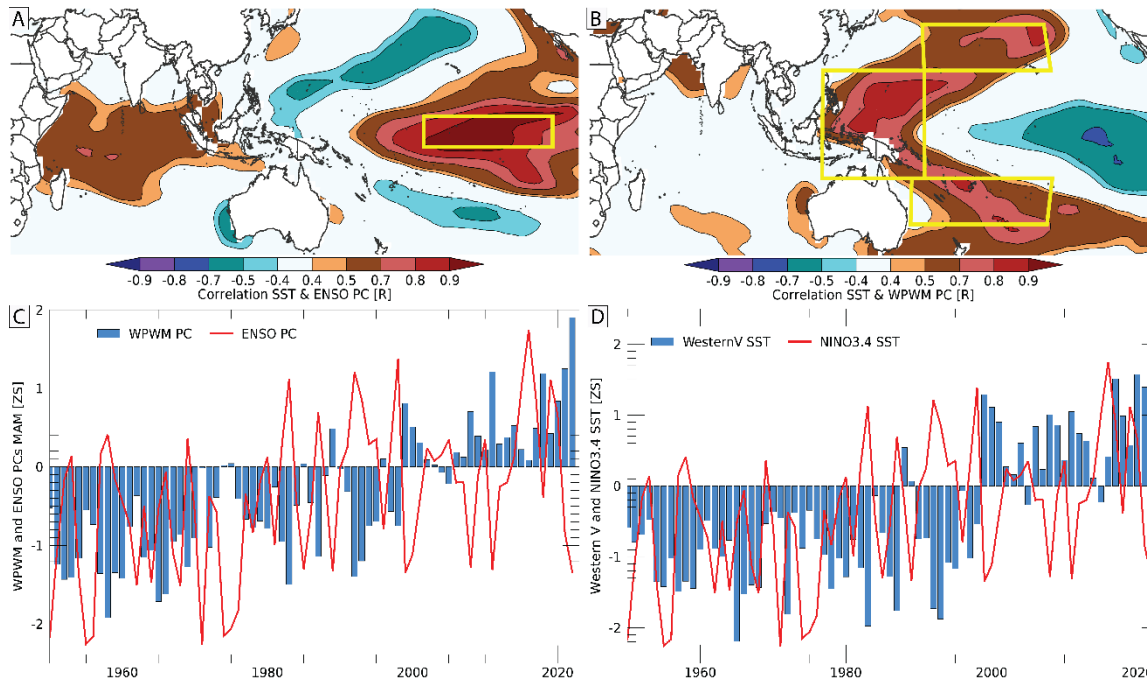


1008  
 1009  
 1010  
 1011  
 1012  
 1013  
 1014  
 1015  
 1016  
 1017

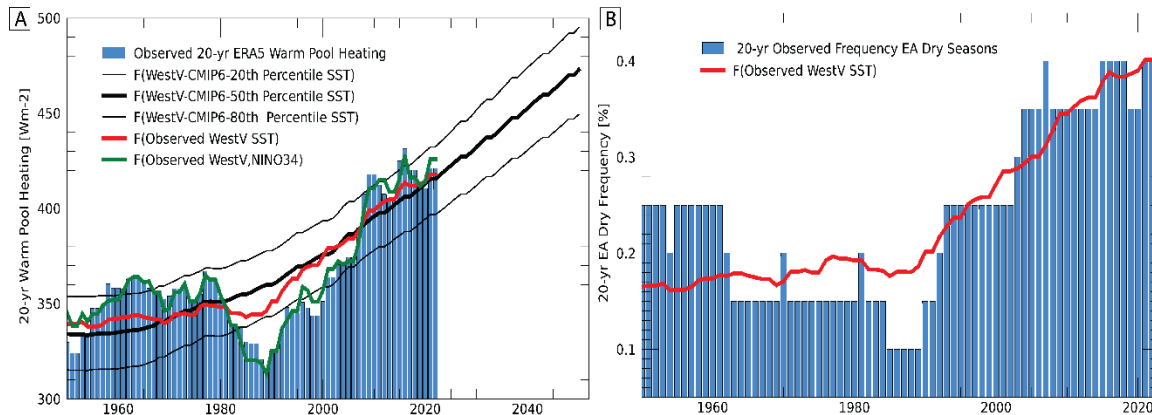
**Figure 6.** Increased Warm Pool atmospheric heating can help explain the East Africa Climate Enigma. Circle color denotes East African MAM rainfall terciles. Green crosses identify preceding OND La Niña seasons. **A.** A scatterplot of ERA5 MAM Warm Pool heating (x-axis) and Warm Pool moisture convergence (y-axis) **B.** A scatterplot of ERA5 Warm Pool heating (x-axis) and standardized MAM Western V SSTs (y-axis). Circle colors in **A** and **B** identify EA wet and dry MAM rainy seasons. **C-D.** Same but for MERRA2 reanalysis.



1018  
 1019 **Figure 7.** Change in atmospheric heating following recent La Niñas can help explain the East  
 1020 Africa Climate Enigma. Circle color denotes East African MAM rainfall terciles. Green crosses  
 1021 identify preceding OND La Niña seasons. **A.** The difference between 1999-2022 and 1950-1997  
 1022 ERA5 atmospheric heating and moisture transports in MAM seasons following OND La Niña  
 1023 events. **B.** PDFs of MAM West Pacific heating following pre- and post-1998 OND La Niña  
 1024 events. **C.** Same for observed EA MAM SPI (i.e. the data plotted in Figure 1B).  
 1025  
 1026



1027  
 1028 **Figure 8.** Relating MAM NINO3.4 and Western V SST to ENSO and West Pacific Warming  
 1029 Mode Empirical Orthogonal Functions (EOF). **A.** 1981-2022 correlation between the 1<sup>st</sup>  
 1030 Principal Component (PC) of tropical Pacific MAM SSTs and observed MAM SSTs. Yellow  
 1031 box denotes the NINO3.4 region. **B.** Same but for the WPWM and Western V region. **C.** Time-  
 1032 series of MAM WPWM and ENSO MAM PCs, expressed as standardized anomalies centered on  
 1033 a 1981-2021 baseline. **D.** Same for regional SST averaged over the Western V and NINO3.4.  
 1034



1035 **Figure 9.** Relating Warm Pool heating and more frequent droughts to anthropogenic warming in  
 1036 the Western V. **A.** Observed and estimated 20-yr ERA5 West Pacific Heating V SST anomalies.  
 1037 The green line show regression estimates based on observed standardized 20-yr Western V and  
 1038 NINO3.4 SST. The red line shows estimates based only observed Western V. The thick black  
 1039 line shows 20-yr Warm Pool heating based on the median CMIP6 Western V SST estimates. The  
 1040 thin black lines show the spread of CMIP6 Warm Pool Heating estimates. **B.** The 20-yr observed  
 1041 frequency of EA dry seasons (i.e. circles in Figure 2C), along with Western V and NINO3.4-  
 1042 based regression estimates.  
 1043  
 1044

1045

## 1046 References

- 1047  
 1048 Adler, R. F., G. Gu, M. Sapiano, J.-J. Wang, and G. J. Huffman (2017), Global precipitation:  
 1049 Means, variations and trends during the satellite era (1979–2014), *Surveys in Geophysics*,  
 1050 38(4), 679-699.  
 1051 Bjerknes, J. (1969), Atmospheric teleconnections from the equatorial Pacific, *Monthly Weather*  
 1052 *Review*, 97(3), 163-172, doi: 10.1175/1520-0493(1969)097<0163:atftpe>2.3.co;2.  
 1053 Button, H. (2022), Famine Early Warning Systems Network forecasts alert USAID to impending  
 1054 food emergencies, edited, US Agency for International Development, Washington, DC.  
 1055 Cai, W., B. Ng, G. Wang, A. Santoso, L. Wu, and K. Yang (2022), Increased ENSO sea surface  
 1056 temperature variability under four IPCC emission scenarios, *Nature Climate Change*, 12(3),  
 1057 228-231, doi: 10.1038/s41558-022-01282-z.  
 1058 Cai, W., A. Santoso, G. Wang, S.-W. Yeh, S.-I. An, K. M. Cobb, M. Collins, E. Guilyardi, F.-F.  
 1059 Jin, and J.-S. Kug (2015a), ENSO and greenhouse warming, *Nature Climate Change*.  
 1060 Cai, W., G. Wang, A. Santoso, M. J. McPhaden, L. Wu, F.-F. Jin, A. Timmermann, M. Collins,  
 1061 G. Vecchi, and M. Lengaigne (2015b), Increased frequency of extreme La Niña events under  
 1062 greenhouse warming, *Nature Climate Change*, 5(2), 132-137.  
 1063 Checchi, F., and W. C. Robinson (2013), Mortality among populations of southern and central  
 1064 Somalia affected by severe food insecurity and famine during 2010-2012*Rep.*, 87 pp,  
 1065 [http://www.fsnao.org/downloads/Somalia\\_Mortality\\_Estimates\\_Final\\_Report\\_8May2013\\_up](http://www.fsnao.org/downloads/Somalia_Mortality_Estimates_Final_Report_8May2013_upload.pdf)  
 1066 [load.pdf](http://www.fsnao.org/downloads/Somalia_Mortality_Estimates_Final_Report_8May2013_upload.pdf), Rome, Washington.

- 1067 Dinku, T., C. Funk, P. Peterson, R. Maidment, T. Tadesse, H. Gadain, and P. Ceccato (2018),  
1068 Validation of the CHIRPS satellite rainfall estimates over eastern of Africa, *Quarterly*  
1069 *Journal of the Royal Meteorological Society*.
- 1070 Endris, H. S., C. Lennard, B. Hewitson, A. Dosio, G. Nikulin, and H.-J. Panitz (2016),  
1071 Teleconnection responses in multi-GCM driven CORDEX RCMs over Eastern Africa,  
1072 *Climate Dynamics*, 46(9), 2821-2846.
- 1073 Endris, H. S., C. Lennard, B. Hewitson, A. Dosio, G. Nikulin, and G. A. Artan (2019), Future  
1074 changes in rainfall associated with ENSO, IOD and changes in the mean state over Eastern  
1075 Africa, *Climate dynamics*, 52(3), 2029-2053.
- 1076 Endris, H. S., P. Omondi, S. Jain, C. Lennard, B. Hewitson, L. Chang'a, J. Awange, A. Dosio, P.  
1077 Ketiem, and G. Nikulin (2013), Assessment of the performance of CORDEX regional  
1078 climate models in simulating East African rainfall, *Journal of Climate*, 26(21), 8453-8475.
- 1079 Eyring, V., S. Bony, G. A. Meehl, C. A. Senior, B. Stevens, R. J. Stouffer, and K. E. Taylor  
1080 (2016), Overview of the Coupled Model Intercomparison Project Phase 6 (CMIP6)  
1081 experimental design and organization, *Geoscientific Model Development*, 9(5), 1937-1958.
- 1082 Finney, D. L., J. H. Marsham, D. P. Walker, C. E. Birch, B. J. Woodhams, L. S. Jackson, and S.  
1083 Hardy (2020), The effect of westerlies on East African rainfall and the associated role of  
1084 tropical cyclones and the Madden–Julian Oscillation, *Quarterly Journal of the Royal*  
1085 *Meteorological Society*, 146(727), 647-664, doi: <https://doi.org/10.1002/qj.3698>.
- 1086 Funk, C., and A. Hoell (2015), The leading mode of observed and CMIP5 ENSO-residual sea  
1087 surface temperatures and associated changes in Indo-Pacific climate, *Journal of Climate*,  
1088 28(11), 4309-4329.
- 1089 Funk, C., and A. Hoell (2017), Recent Climate Extremes Associated with the West Pacific  
1090 Warming Mode, in *Climate Extremes: Patterns and Mechanisms*, edited by S. Y. Wang, Jin-  
1091 Ho; Funk, Chris; Gillies, Robert, Wiley Press, American Geophysical Union.
- 1092 Funk, C., and e. al. (2019), Recognizing the Famine Early Warning Systems Network (FEWS  
1093 NET): Over 30 Years of Drought Early Warning Science Advances and Partnerships  
1094 Promoting Global Food Security, *Bull. Amer. Meteor. Soc.* 100(6), 1010-1027.
- 1095 Funk, C., S. E. Nicholson, M. Landsfeld, D. Klotter, P. Peterson, and L. Harrison (2015a), The  
1096 Centennial Trends Greater Horn of Africa precipitation dataset, *Scientific Data*, 2(150050),  
1097 doi: 10.1038/sdata.2015.50.
- 1098 Funk, C., M. D. Dettinger, J. C. Michaelsen, J. P. Verdin, M. E. Brown, M. Barlow, and A. Hoell  
1099 (2008), Warming of the Indian Ocean threatens eastern and southern African food security  
1100 but could be mitigated by agricultural development, *Proc Nat Acad Sci USA*, 105(31),  
1101 11081-11086.
- 1102 Funk, C., A. Hoell, S. Shukla, I. Bladé, B. Liebmann, J. B. Roberts, and G. Husak (2014),  
1103 Predicting East African spring droughts using Pacific and Indian Ocean sea surface  
1104 temperature indices, *Hydrology and Earth System Sciences Discussions*, 11(3), 3111-3136.
- 1105 Funk, C., G. Senay, A. Asfaw, J. Verdin, J. Rowland, J. Michaelson, G. Eilerts, D. Korecha, and  
1106 R. Choularton (2005), Recent drought tendencies in Ethiopia and equatorial-subtropical  
1107 eastern Africa, *Vulnerability to Food Insecurity: Factor Identification and Characterization*  
1108 *Report, 1*, 12.
- 1109 Funk, C., P. Peterson, M. Landsfeld, D. Pedreros, J. Verdin, S. Shukla, G. Husak, J. Rowland, L.  
1110 Harrison, and A. Hoell (2015b), The climate hazards infrared precipitation with stations—a  
1111 new environmental record for monitoring extremes, *Scientific data*, 2.

- 1112 Funk, C., et al. (2018), Examining the role of unusually warm Indo-Pacific sea surface  
1113 temperatures in recent African droughts *Quart J Roy Meteor Soc*, 144, 360-383, doi:  
1114 10.1002/qj.3266.
- 1115 Funk, C., et al. (2019), Examining the potential contributions of extreme 'Western V' sea surface  
1116 temperatures to the 2017 March-June East African Drought, *Bull. Amer. Meteor. Soc.*,  
1117 100(1), S55-S60.
- 1118 Gelaro, R., et al. (2017), The Modern-Era Retrospective Analysis for Research and Applications,  
1119 Version 2 (MERRA-2), *Journal of Climate*, 30(14), 5419-5454, doi: 10.1175/JCLI-D-16-  
1120 0758.1.
- 1121 Gill, A. E. (1980), Some simple solutions for heat-induced tropical circulation, *Q J Roy Meteor*  
1122 *Soc*, 106, 447-462.
- 1123 Gill, A. E. (1982), *Atmosphere-ocean dynamics*, 662 pp., Academic Press, San Diego.
- 1124 Gudoshava, M., H. O. Misiani, Z. T. Segele, S. Jain, J. O. Ouma, G. Otieno, R. Anyah, V. S.  
1125 Indasi, H. S. Endris, and S. Osima (2020), Projected effects of 1.5 C and 2 C global warming  
1126 levels on the intra-seasonal rainfall characteristics over the Greater Horn of Africa, *Environ*  
1127 *Res Lett*, 15(3), 034037.
- 1128 Hersbach, H., B. Bell, P. Berrisford, S. Hirahara, A. Horányi, J. Muñoz-Sabater, J. Nicolas, C.  
1129 Peubey, R. Radu, and D. Schepers (2020), The ERA5 global reanalysis, *Quarterly Journal of*  
1130 *the Royal Meteorological Society*, 146(730), 1999-2049.
- 1131 Hoell, A., and C. Funk (2013a), Indo-Pacific sea surface temperature influences on failed  
1132 consecutive rainy seasons over eastern Africa, *Climate Dynamics*, 43(5-6), 1645-1660.
- 1133 Hoell, A., and C. Funk (2013b), The ENSO-Related West Pacific Sea Surface Temperature  
1134 Gradient, *Journal of Climate*, 26(23), 9545-9562.
- 1135 Huang, B., P. W. Thorne, V. F. Banzon, T. Boyer, G. Chepurin, J. H. Lawrimore, M. J. Menne,  
1136 T. M. Smith, R. S. Vose, and H.-M. Zhang (2017), Extended Reconstructed Sea Surface  
1137 Temperature, Version 5 (ERSSTv5): Upgrades, Validations, and Intercomparisons, *Journal*  
1138 *of Climate*, 30(20), 8179-8205, doi: 10.1175/JCLI-D-16-0836.1.
- 1139 Husak, G. J., J. Michaelsen, and C. Funk (2007), Use of the gamma distribution to represent  
1140 monthly rainfall in Africa for drought monitoring applications, *International Journal of*  
1141 *Climatology*, 27(7), 935-944.
- 1142 ICPAC, FEWS-NET, WMO, FAO, WFP, and JRC (2022a), Unprecedented drought brings threat  
1143 of starvation to millions in Ethiopia, Kenya, and Somalia, *Multi-Agency Drought Alert*.
- 1144 ICPAC, et al. (2022b), Immediate global action required to prevent Famine in the Horn of  
1145 Africa, *Multi-agency Drought Alert*.
- 1146 Johnson, N. C. (2013), How many ENSO flavors can we distinguish?, *Journal of Climate*,  
1147 26(13), 4816-4827.
- 1148 Kilavi, M., D. MacLeod, M. Ambani, J. Robbins, R. Dankers, R. Graham, H. Titley, A. A. Salih,  
1149 and M. C. Todd (2018), Extreme rainfall and flooding over central Kenya including Nairobi  
1150 city during the long-rains season 2018: causes, predictability, and potential for early warning  
1151 and actions, *Atmosphere*, 9(12), 472.
- 1152 Kirtman, B. P., D. Min, J. M. Infanti, J. L. Kinter III, D. A. Paolino, Q. Zhang, H. van den Dool,  
1153 S. Saha, M. P. Mendez, and E. Becker (2014), The North American Multimodel Ensemble:  
1154 Phase-1 seasonal-to-interannual prediction; phase-2 toward developing intraseasonal  
1155 prediction, *B Am Meteorol Soc*, 95(4), 585-601.

- 1156 L'Heureux, M. L., S. Lee, and B. Lyon (2013), Recent multidecadal strengthening of the Walker  
1157 circulation across the tropical Pacific, *Nature Climate Change*, 3(6), 571-576, doi:  
1158 doi:10.1038/nclimate1840.
- 1159 Liebmann, B., I. Bladé, G. N. Kiladis, L. M. Carvalho, G. B. Senay, D. Allured, S. Leroux, and  
1160 C. Funk (2012), Seasonality of African precipitation from 1996 to 2009, *Journal of Climate*,  
1161 25(12), 4304-4322.
- 1162 Liebmann, B., M. P. Hoerling, C. Funk, I. Bladé, R. M. Dole, D. Allured, X. Quan, P. Pegion,  
1163 and J. K. Eischeid (2014), Understanding Recent Eastern Horn of Africa Rainfall Variability  
1164 and Change, *J. Climate*, 27(23), 8630-8645.
- 1165 Lyon, B. (2014), Seasonal Drought in the Greater Horn of Africa and its Recent Increase During  
1166 the March-May Long Rains, *Journal of Climate*, 27(2014), 7953-7975.
- 1167 Lyon, B. (2020), Biases in CMIP5 Sea Surface Temperature and the Annual Cycle of East  
1168 African Rainfall, *Journal of Climate*, 33(19), 8209-8223.
- 1169 Lyon, B. (2021), Biases in sea surface temperature and the annual cycle of Greater Horn of  
1170 Africa rainfall in CMIP6, *International Journal of Climatology*.
- 1171 Lyon, B., and D. G. DeWitt (2012), A recent and abrupt decline in the East African long rains,  
1172 *GEOPHYSICAL RESEARCH LETTERS*, 39(L02702).
- 1173 Lyon, B., and N. Vigaud (2017), Unraveling East Africa's climate paradox, *Climate extremes:*  
1174 *Patterns and mechanisms*, 265, 281.
- 1175 Lyon, B., A. G. Barnston, and D. G. DeWitt (2013), Tropical pacific forcing of a 1998–1999  
1176 climate shift: observational analysis and climate model results for the boreal spring season,  
1177 *Climate Dynamics*, 43 (3-4), 893-909.
- 1178 MacLeod, D. (2018), Seasonal predictability of onset and cessation of the east African rains,  
1179 *Weather and climate extremes*, 21, 27-35.
- 1180 Mantua, N., and S. Hare (2002), The Pacific Decadal Oscillation, *Journal of Oceanography*,  
1181 58(1), 35-44, doi: 10.1023/a:1015820616384.
- 1182 Meinshausen, M., Z. R. Nicholls, J. Lewis, M. J. Gidden, E. Vogel, M. Freund, U. Beyerle, C.  
1183 Gessner, A. Nauels, and N. Bauer (2020), The shared socio-economic pathway (SSP)  
1184 greenhouse gas concentrations and their extensions to 2500, *Geoscientific Model*  
1185 *Development*, 13(8), 3571-3605.
- 1186 Nicholson, S. E. (2015), Long-term variability of the East African 'short rains' and its links to  
1187 large-scale factors, *International Journal of Climatology*, n/a-n/a, doi: 10.1002/joc.4259.
- 1188 Nicholson, S. E. (2017), Climate and Climatic Variability of Rainfall over Eastern Africa,  
1189 *Reviews of Geophysics*, n/a-n/a, doi: 10.1002/2016RG000544.
- 1190 NOAA (2022), *Cold & Warm Episodes by Season*, edited by C. P. Center.
- 1191 Ogega, O. M., J. Koske, J. B. Kung'u, E. Scoccimarro, H. S. Endris, and M. N. Mistry (2020),  
1192 Heavy precipitation events over East Africa in a changing climate: results from CORDEX  
1193 RCMs, *Climate Dynamics*, 55(3), 993-1009.
- 1194 Park, S., D. Kang, C. Yoo, J. Im, and M.-I. Lee (2020), Recent ENSO influence on East African  
1195 drought during rainy seasons through the synergistic use of satellite and reanalysis data,  
1196 *ISPRS Journal of Photogrammetry and Remote Sensing*, 162, 17-26.
- 1197 Peixoto, J. P., and A. H. Oort (1992), *Physics of Climate*, Am. Inst. Physics, New York.
- 1198 Rowell, D. P., B. B. Booth, S. E. Nicholson, and P. Good (2015), Reconciling Past and Future  
1199 Rainfall Trends over East Africa, *Journal of Climate*, 28(24), 9768-9788, doi: 10.1175/JCLI-  
1200 D-15-0140.1.

- 1201 Roxy, M. K., P. Dasgupta, M. J. McPhaden, T. Suematsu, C. Zhang, and D. Kim (2019),  
1202 Twofold expansion of the Indo-Pacific warm pool warps the MJO life cycle, *Nature*,  
1203 575(7784), 647-651, doi: 10.1038/s41586-019-1764-4.
- 1204 Rubiano, M. P. (2022), How Scientists Predict Famine Before It Hits, *BBC Future Planet*.
- 1205 Schwarzwald, K., L. Goddard, R. Seager, M. Ting, and K. Marvel (2022), Understanding CMIP6  
1206 Biases in the Representation of the Greater Horn of Africa Long and Short Rains.
- 1207 Seager, R., N. Henderson, and M. Cane (2022), Persistent discrepancies between observed and  
1208 modeled trends in the tropical Pacific Ocean, *Journal of Climate*, 1-41, doi: 10.1175/jcli-d-  
1209 21-0648.1.
- 1210 Seager, R., M. Cane, N. Henderson, D.-E. Lee, R. Abernathey, and H. Zhang (2019),  
1211 Strengthening tropical Pacific zonal sea surface temperature gradient consistent with rising  
1212 greenhouse gases, *Nature Climate Change*, 9(7), 517-522, doi: 10.1038/s41558-019-0505-x.
- 1213 Shukla, S., J. Roberts, A. Hoell, C. C. Funk, F. Robertson, and B. Kirtman (2016), Assessing  
1214 North American multimodel ensemble (NMME) seasonal forecast skill to assist in the early  
1215 warning of anomalous hydrometeorological events over East Africa, *Climate Dynamics*, 1-  
1216 17, doi: 10.1007/s00382-016-3296-z.
- 1217 Shukla, S., G. Husak, W. Turner, F. Davenport, C. Funk, L. Harrison, and N. Krell (2021), A  
1218 slow rainy season onset is a reliable harbinger of drought in most food insecure regions in  
1219 Sub-Saharan Africa, *Plos one*, 16(1), e0242883.
- 1220 Tierney, J., J. Smerdon, K. Anchukaitis, and R. Seager (2013), Multidecadal variability in East  
1221 African hydroclimate controlled by the Indian Ocean, *Nature*, 493(7342), 389-392.
- 1222 Tierney, J. E., C. C. Ummenhofer, and P. B. deMenocal (2015), Past and future rainfall in the  
1223 Horn of Africa, *Science Advances*, 1(9), 1-8, doi: 10.1126/sciadv.1500682.
- 1224 Trenberth, K. E., and D. P. Stepaniak (2003a), Covariability of components of poleward  
1225 atmospheric energy transports on seasonal and interannual timescales, *Journal of Climate*,  
1226 16(22), 3691-3705.
- 1227 Trenberth, K. E., and D. P. Stepaniak (2003b), Seamless poleward atmospheric energy transports  
1228 and implications for the Hadley circulation, *Journal of Climate*, 16(22), 3706-3722.
- 1229 Verdin, J., C. Funk, G. Senay, and R. Choullarton (2005), Climate science and famine early  
1230 warning, *Philos T Roy Soc B*, 360(1463), 2155-2168.
- 1231 Voosen, P. (2020), The hunger forecast, *Science*, 368(6488), 226-229, doi: DOI:  
1232 10.1126/science.368.6488.226.
- 1233 Wainwright, C. M., J. H. Marsham, R. J. Keane, D. P. Rowell, D. L. Finney, E. Black, and R. P.  
1234 Allan (2019), 'Eastern African Paradox' rainfall decline due to shorter not less intense Long  
1235 Rains, *npj Climate and Atmospheric Science*, 2(1), 1-9.
- 1236 Walker, D. P., J. H. Marsham, C. E. Birch, A. A. Scaife, and D. L. Finney (2020), Common  
1237 Mechanism for Interannual and Decadal Variability in the East African Long Rains,  
1238 *Geophysical Research Letters*, 47(22), e2020GL089182, doi:  
1239 <https://doi.org/10.1029/2020GL089182>.
- 1240 Williams, P., and C. Funk (2011), A westward extension of the warm pool leads to a westward  
1241 extension of the Walker circulation, drying eastern Africa, *Climate Dynamics*, 37(11-12),  
1242 2417-2435.
- 1243 Wills, R. C. J., Y. Dong, C. Proistosescu, K. C. Armour, and D. S. Battisti (2022), Systematic  
1244 Climate Model Biases in the Large-Scale Patterns of Recent Sea-Surface Temperature and  
1245 Sea-Level Pressure Change, *Geophysical Research Letters*, 49(17), e2022GL100011, doi:  
1246 <https://doi.org/10.1029/2022GL100011>.

1247 Yang, W., R. Seager, M. A. Cane, and B. Lyon (2014), The East African Long Rains in  
1248 Observations and Models, *Journal of Climate*, 27(19), 7185-7202, doi: 10.1175/JCLI-D-13-  
1249 00447.1.  
1250